Methodology Development and Investigation of Turbofan Engine Response to Simultaneous Inlet Total Pressure and Swirl Distortion

Dustin J. Frohnapfel

Dissertation submitted to the Faculty of the
Virginia Polytechnic Institute and State University
in partial fulfillment of the requirements for the degree of

Doctor of Philosophy
in
Mechanical Engineering

Walter F. O'Brien, Co-Chair
K. Todd Lowe, Co-Chair
William W. Copenhaver
William T. Cousins
Clinton L. Dancey
Alfred L. Wicks

February 22, 2019
Blacksburg, Virginia

Keywords: Turbofan Engine, Inlet Distortion, Total Pressure, Swirl, Secondary Flow, Computational Fluid Dynamics, Experimental Ground Test

Copyright 2019, Dustin J. Frohnapfel

Methodology Development and Investigation of Turbofan Engine Response to Simultaneous Inlet Total Pressure and Swirl Distortion

Dustin J. Frohnapfel

ABSTRACT

As a contribution to advancing turbofan engine ground test technology in support of propulsion system integration in modern conceptual aircraft, a novel inlet distortion generator (ScreenVane™) was invented. The device simultaneously reproduces combined inlet total pressure and swirl distortion elements in a tailored profile intended to match a defined turbofan engine inlet distortion profile. The device design methodology was intended to be sufficiently generic to be utilized in support of any arbitrary inlet distortion profile yet adequately specific to generate high-fidelity inlet distortion profile simulation.

For the current investigation, a specific inlet distortion profile was defined using computational analysis of a conceptual boundary layer ingesting S-duct turbofan engine inlet. The resulting inlet distortion profile, consisting of both total pressure and swirl distortion elements, was used as the objective profile to be matched by the ScreenVane in a turbofan engine ground test facility.

A ScreenVane combined inlet total pressure and swirl distortion generator was designed, computationally analyzed, and experimentally validated. The design process involved specifying a total pressure loss screen pattern and organizing a unique arrangement of swirl inducing turning vanes. Computational results indicated that the ScreenVane manufactured distortion profile matched the predicted S-duct turbofan engine inlet manufactured distortion profile with excellent agreement in pattern shape, extent, and intensity. Computational full-field total pressure recovery and swirl angle profiles matched within approximately 1% and 2.5° (RMSD), respectively. Experimental turbofan engine ground test results indicated that the ScreenVane manufactured distortion profile matched the predicted S-duct turbofan engine inlet manufactured distortion profile with excellent agreement in pattern shape, extent, and intensity. Experimental full-field total pressure recovery and swirl angle profiles matched within approximately 1.25% and 3.0° (RMSD), respectively.

Following the successful reproduction of the S-duct turbofan engine inlet manufactured distortion profile, a turbofan engine response evaluation was conducted using the validated ScreenVane inlet distortion generator. Flow measurements collected at discrete planes immediately upstream and downstream of the fan rotor isolated the component for performance analysis. Based on the results of this particular engine and distortion investigation, the adiabatic fan efficiency was negligibly altered while operating with distorted inflow conditions when compared to nominal inflow conditions. Fuel flow measurements indicated that turbofan engine inlet air mass flow specific fuel consumption increased by approximately 5% in the presence of distortion.

While a single, specific turbofan engine inlet distortion profile was studied in this investigation, the ScreenVane methodology, design practices, analysis approaches, manufacturing techniques, and experimental procedures are applicable to any arbitrary, realistic combined inlet total pressure and swirl distortion.

Methodology Development and Investigation of Turbofan Engine Response to Simultaneous Inlet Total Pressure and Swirl Distortion

Dustin J. Frohnapfel

GENERAL AUDIENCE ABSTRACT

As a contribution to advancing turbofan engine ground test technology in support of propulsion system integration in modern conceptual aircraft, a novel inlet distortion generator (ScreenVane^{TM}) was invented. The device simultaneously reproduces combined inlet total pressure and swirl distortion elements in a tailored profile intended to match a defined turbofan engine inlet distortion profile. The device design methodology was intended to be sufficiently generic to be utilized in support of any arbitrary inlet distortion profile yet adequately specific to generate high-fidelity inlet distortion profile simulation.

For the current investigation, a specific inlet distortion profile was defined using computational analysis of a conceptual boundary layer ingesting S-duct turbofan engine inlet. The resulting inlet distortion profile, consisting of both total pressure and swirl distortion elements, was used as the objective profile to be matched by the ScreenVane in a turbofan engine ground test facility.

A ScreenVane combined inlet total pressure and swirl distortion generator was designed, computationally analyzed, and experimentally validated. The design process involved specifying a total pressure loss screen pattern and organizing a unique arrangement of swirl inducing turning vanes. Computational and experimental results indicated that the ScreenVane manufactured distortion profile matched the predicted S-duct turbofan engine inlet manufactured distortion profile with excellent agreement in pattern shape, extent, and intensity.

Following the successful reproduction of the S-duct turbofan engine inlet manufactured distortion profile, a turbofan engine response evaluation was conducted using the validated ScreenVane inlet distortion generator. Flow measurements collected at discrete planes immediately upstream and downstream of the fan rotor isolated the component for performance analysis. Based on the results of this particular engine and distortion investigation, the adiabatic fan efficiency was negligibly altered while operating with distorted inflow conditions when compared to nominal inflow conditions. Fuel flow measurements indicated that turbofan engine inlet air mass flow specific fuel consumption increased in the presence of distortion.

While a single, specific turbofan engine inlet distortion profile was studied in this investigation, the ScreenVane methodology, design practices, analysis approaches, manufacturing techniques, and experimental procedures are applicable to any arbitrary, realistic combined inlet total pressure and swirl distortion.

Acknowledgements

First and foremost, I would like to acknowledge and graciously thank my graduate research advisors and dissertation committee co-chairs Dr. Walter O'Brien and Dr. Todd Lowe for supporting this research from start to finish. Your technical advice, attention to the project, and confidence in my abilities fostered an unparalleled research, design, development, and engineering environment that led directly to my achievements and successes. I will be forever grateful to have studied turbomachinery with you and will carry my experience at the Virginia Tech Turbomachinery and Propulsion Research Laboratory as motivation throughout my career and life.

I would like to thank my dissertation committee: Dr. William Copenhaver, Dr. William Cousins, Dr. Clinton Dancey, and Dr. Alfred Wicks. Your comments, suggestions, and assistance have helped shape this investigation into an innovative piece of research. Dr. Dancey and Dr. Wicks assisted with academic views and theories, while Dr. Copenhaver and Dr. Cousins added industrial knowledge to serve the greater turbomachinery industry.

To all of my colleagues at the Virginia Tech TurboLab: THANK YOU! It takes an exceptionally hard-working, talented, and intelligent team to conduct turbofan engine ground test research. To my early colleagues, Justin Bailey, Anthony Ferrar, Chaitanya Halbe, and William Schneck, thank you for laying the foundation for world-class turbofan engine research at this facility. To my more recent colleagues, Dylan Dawson, John Gillespie, Tamara Guimarães, Elizabeth Mack, and Katherine Smith, thank you for the opportunity to work with you and learn from you. To the laboratory and department staff, Dr. William Copenhaver, Dr. Todd Lowe, Dr. Walter O'Brien, Dr. Alexandrina Untaroiu, Diana Israel, and Gregg Perley, thank you for your tremendous support in every aspect of research spanning design reviews, analysis, procurement, fabrication, assembly, installation, and test. You all made my work and my time at Virginia Tech memorable and fun.

To my parents, Tim and Penny Frohnapfel, and my sister, Tiffany Frohnapfel, thank you for providing endless encouragement and for believing in my wildest dreams. The solid foundation of our family is a constant source of energy and the work ethic that you have instilled in me drives me to accomplish any goal.

Finally, to my fiancé, Robyn Higginbotham, thank you for the seemingly infinite love, support, and, most importantly, patience that you have given throughout this endeavor. Research requires a tremendous amount of work and time, but it pales in comparison to the sacrifices that you have made for us. I dedicate this work and my life to you, for all the evers.

Sincerely,
Dustin J. Frohnapfel

Contents

List of Figures

List of Tables

Nomenclature

	English	
A_e	Exit Area	in^2
A_i	Entrance Area	in^2
a	Speed of Sound	ft/s
b	Transducer Calibration Intercept	psia
C_2	Three-Dimensional Loss Coefficient	1/in
C_d	Discharge Coefficient	
Cp_P	Static Pressure Pressure Coefficient	
Cp_{P0}	Total Pressure Pressure Coefficient	
$Cp_{\alpha r}$	Radial Flow Angle Pressure Coefficient	
$Cp_{\alpha\theta}$	Tangential Flow Angle Pressure Coefficient	
C_r	Radial Velocity	ft/s
$C_{r\theta z}$	Three-Dimensional Velocity Magnitude	ft/s
C_z	Axial Velocity	ft/s
$C_{z\infty}$	Free-Stream Velocity	ft/s
C_θ	Tangential Velocity	ft/s
D	Diameter	in
D	Drag	lb_f
D_e	Exit Diameter	in
g	Gravitational Acceleration	ft/s^2
FTPR	Fan Total Pressure Ratio	
FTTR	Fan Total Temperature Ratio	
H_i	Entrance Height	in
K	Two-Dimensional Loss Coefficient	
L	Length	in
L	Lift	lb_f
M	Mach Number	
m	Transducer Calibration Slope	psia/V
m_1	Initial Mass	lb_m
m_2	Final Mass	lb_m
$\dot{m}_a$	Air Mass Flow Rate	lb_m/s
$\dot{m}_f$	Fuel Mass Flow Rate	gal/hr
$\dot{m}SFC$	Inlet Air Mass Flow Rate Specific Fuel Consumption	$(gal/hr)/(lb_m/s)$
N	Number of Samples	
N	Spool Speed	%
N_1	Fan Spool Speed	%
N_2	Core Spool Speed	%
$n_{screens}$	Number of Wire Mesh Screen Layers	

P	Pressure Measurement	psia
P	Static Pressure	psia
P_0	Total Pressure	psia
$P_{1,2,3,4,5}$	Five Hole Probe Measured Pressures	psia
P_{atm}	Atmospheric Pressure	psia
P_{std}	Standard Atmospheric Pressure Reference	psia
PAV	Average Total Pressure	psia
PAVLOW	Average Total Pressure (Low Pressure Region)	psia
PFAV	Face Average Total Pressure	psia
$\overline{P}$	Four Port Average Five Hole Pressure	psia
R	Gas Constant (Air)	ft lb_f/lb_m °R
R_0	Total Pressure Recovery	
Re	Reynold's Number	
r	Radius	in
r_w	Wall Radius	in
SI	Swirl Intensity	deg
s	Range	ft
T	Static Temperature	°R
T	Temperature Measurement	°R
T_0	Total Temperature	°R
T_{atm}	Atmospheric Temperature	°R
T_{std}	Standard Atmospheric Temperature Reference	°R
TSFC	Thrust Specific Fuel Consumption	(gal/hr)/lb_f
$t_{screens}$	Thickness of Wire Mesh Screen	in
u_∞	Flight Velocity	ft/s
V	Velocity Magnitude	ft/s
V	Voltage Measurement	V
W_i	Entrance Width	in
Y	Vertical Component	in

<u>Greek</u>

α	Porosity	%
α_r	Radial Flow Angle	deg
α_θ	Tangential Flow Angle, Swirl Angle	deg
γ	Specific Heat Ratio (Air)	
Δ	Comparison Data	
ΔH	Centerline Shift	in
ΔP	Static Pressure Loss	psia
ΔP_0	Total Pressure Loss	psia
$\Delta PC/P$	Circumferential Total Pressure Distortion Intensity	
$\Delta PR/P$	Radial Total Pressure Distortion Intensity	
δ	Boundary Layer Height	in
δ	Standard Pressure Correction Factor	
η_f	Adiabatic Fan Efficiency	
θ	Standard Temperature Correction Factor	
θ	Fan Rotation Angle	deg
μ	Dynamic Viscosity	psia s
ρ	Density	lb_m/ft^3

Subscript	
corrected	Indicates Term Corrected to Standard Atmospheric Conditions
ideal	Indicates Ideal Term
measured	Indicates Measured Term

Abbreviation	
AIP	Aerodynamic Interface Plane
ASME	American Society of Mechanical Engineers
BLI	Boundary Layer Ingestion
CAD	Computer-Aided Design
CFD	Computational Fluid Dynamics
EXP	Experimental
FREP	Fan Rotor Exit Plane
NASA	National Aeronautics and Space Administration
P&WC	Pratt and Whitney Canada
PTFE	Polytetrafluoroethylene
RMS	Root Mean Square
RMSD	Root Mean Square Difference
SAE	Society of Automotive Engineers
SDP	ScreenVane Design Plane

Chapter 1 – Introduction

1.1 Dissertation Overview

Modern conceptual aircraft designs are increasingly shifting turbofan engine installations away from pylon mounts in conventional tube-and-wing airframes toward highly integrated, often embedded, engine/airframe arrangements associated with boundary layer ingesting blended wing body architectures. These unified engine/airframe systems offer superior propulsive efficiency and performance in terms of lift-to-drag ratio, fuel consumption, range, and noise abatement and are currently viewed as the most promising solution to rising fuel costs and ever tightening airfield restrictions.

While the potential advantages of highly coupled engine/airframe architectures are numerous, the integrated turbofan engines are frequently exposed to non-uniform inlet conditions, typically referred to as inlet flow distortions, emanating from interactions between the engine, airframe, and any associated inlets or nearby control surfaces. Left unmitigated, the inlet flow distortions pose a significant risk to turbofan engine operation. In order to achieve an optimized vehicle, these interactions must be understood and accounted for through safety, operability, and performance margins. This requirement leads to the necessity of improved design methodology, updated simulation models, enhanced analysis techniques, and rigorous test procedures.

The research presented in the following dissertation is the culmination of a comprehensive investigation into turbofan engine response to simultaneous inlet total pressure and swirl distortion. The specific inlet distortion profile was defined from computational analysis of a turbofan engine inlet associated with an embedded installation in a blended wing body aircraft subjected to significant amounts of boundary layer ingestion. A novel distortion device, designated ScreenVane, was invented and designed with the goal of producing a tailored combined total pressure and swirl distortion matching the conditions exiting the turbofan engine inlet duct. Computational verification of the ScreenVane design methodology was completed as well as experimental ground test validation of computational models. Additionally, turbofan engine response experimental ground tests were conducted to quantify the implications of subjecting a turbofan engine to continuous inlet flow distortion. All computational analyses and experimental ground tests were conducted at the Virginia Tech Turbomachinery and Propulsion Research Laboratory in Blacksburg, VA.

This chapter (Chapter 1) outlines the future applications of conventional turbofan engines installed in unconventional arrangements, reviews the current state-of-the-art for turbofan inlet distortion ground test procedures and apparatus, and places the current investigation into the context of ongoing research throughout the turbomachinery and aviation industry. Chapter 2 presents a computational case study involving an embedded turbofan engine installation attached to an S-duct inlet subjected to varying amounts of boundary layer flow ingestion. Chapter 3 explains the methodology involved in design and manufacture of the ScreenVane combined total pressure and swirl distortion generator. Chapter 4 documents the computational verification while Chapter 5 documents the experimental ground test validation of the ScreenVane combined total pressure and swirl distortion generator. Chapter 6 then demonstrates the application of the ScreenVane as a combined total pressure and swirl distortion generator for utilization in turbofan engine ground tests. Chapter 7 summarizes the significant outcomes and Chapter 8 reports all conclusions based on the results obtained throughout the investigation.

While a singular distortion profile is presented in the following document, it is merely intended to serve as an example. The ScreenVane methodology should not be considered limited to only this example profile, but should be considered a valid means to simulate nearly any realistic combined total pressure and swirl distortion.

1.2 Literature Review and Background

1.2.1 The Future of Turbofan Engine Installation Configurations

Future aircraft designs appear to be trending toward a paradigm shift, opting for highly integrated configurations that combine propulsion and control subsystems into blended wing body airframes rather than conventional discrete fuselage, wings, and engines common in present designs. This is the case for a wide range of aircraft in both commercial and military applications. Each class has specific requirements sacrificing performance for efficiency or vice versa, but nearly all modern concepts feature some level of propulsion integration to achieve goals that are currently unobtainable using conventional designs [1-11].

Focusing on commercial subsonic transport aircraft, the prospect of incorporating propulsion systems into airframe structures is leading to exciting breakthroughs in efficiency, fuel consumption, range, and noise abatement. Highly integrated aircraft typically have smaller frontal area, greater lift-to-drag ratio, and enhanced fuselage noise shielding. Additionally, these integrated aircraft concepts readily allow for boundary layer ingestion due to the close coupling of turbofan engines with the aircraft lifting surfaces. Boundary layer ingestion is a process in which the turbofan engine inlet is located within the boundary layer flow. The engine therefore ingests the relatively low energy boundary layer flow, reenergizes the flow, and exhausts a jet stream that more closely matches the free-stream. The benefits of boundary layer ingestion include reduced aircraft drag, reduced aircraft wake, and reduced required thrust culminating in estimated fuel savings of greater than 10% when compared to conventional aircraft completing identical missions [1,4,12-22].

Figure 1.1 illustrates increasing advantages with increasing levels of turbofan engine integration. The initial concept (top) features a blended wing body airframe with pod mounted engines located sufficiently above the lifting surface to avoid ingesting boundary layer flow. This is likely the nearest term concept to reach maturation. Because the propulsion system in this arrangement is simply moved from below the wing to above the wing, conventional turbofan engines can be installed with little modification. This arrangement provides the least system benefit as both ram drag and boundary layer parasitic drag remain comparable to conventional tube-and-wing aircraft. Increasing complexity (middle), the turbofan engines are installed near the aircraft lifting surface either within or just above the boundary layer flow. The significant benefit of this arrangement is a reduction in frontal area resulting in decreased ram drag. In applications without boundary layer ingestion, turbofan engines may occasionally be exposed to leading edge vortices or flow distortion arising from aggressive flight maneuvers. In applications with boundary layer ingestion, boundary layer parasitic drag and aircraft wake are reduced; however, the turbofan engine is subjected to more severe and continuous distortions. Advancing the technology further (bottom), turbofan engines are embedded within the aircraft lifting surface with flow entering via ducted inlets. This arrangement offers the greatest system benefit in terms of drag reduction and required thrust reduction as the aircraft frontal area is minimized and aircraft wake is nearly eliminated through engine ingestion and re-energization. Turbofan engines will be subjected to continuous boundary layer ingestion likely leading to continuous inlet flow distortions. While the system benefits increase with increasing complexity and amounts of boundary layer ingestion, the turbofan engines must operate with high efficiency and survive high cycle load fluctuations to achieve the greatest return.

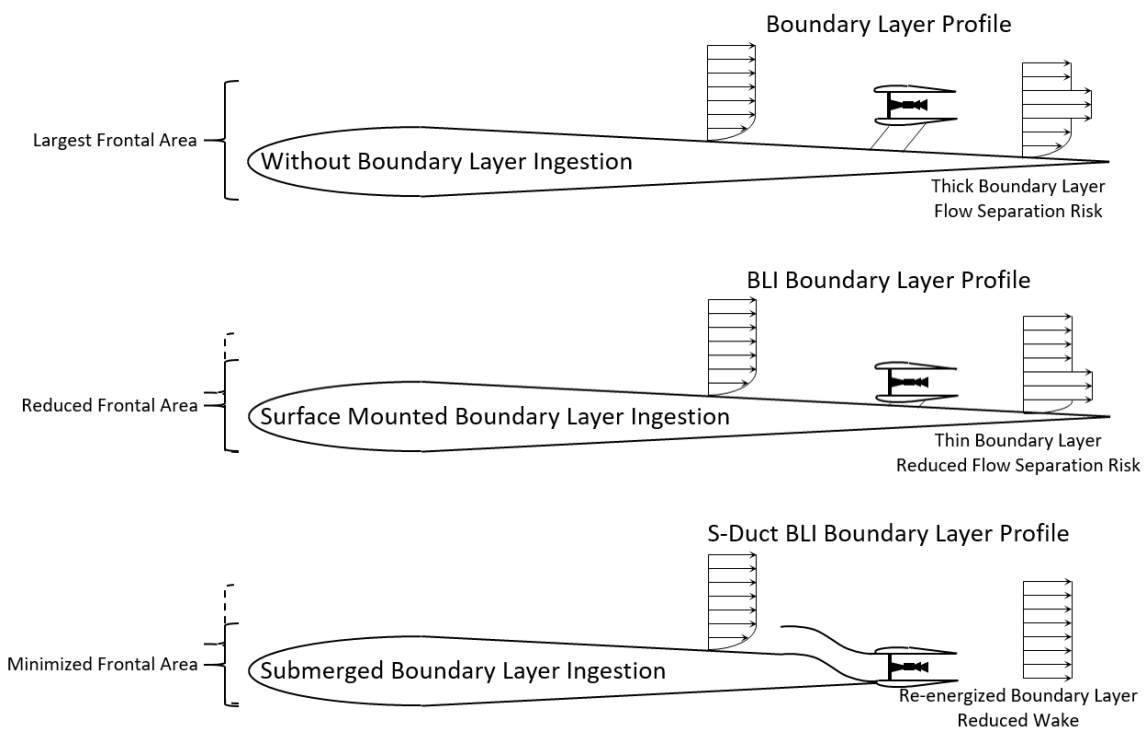

Figure 1.1: Boundary Layer Ingesting Blended Wing Body Aircraft – Schematic

1.2.2 The Challenges Surrounding Turbofan Engine Inlet Flow Distortion

From high level inspection of the Breguet range equation (Equation 1.1), an increase in lift-to-drag ratio or, more simply, a reduction in aircraft drag results in increased range for equivalent propulsion system efficiency, flight conditions, and aircraft weight. It is therefore imperative that turbofan engines installed in highly integrated engine/airframe configurations operate with performance and efficiency levels matching or exceeding conventionally mounted counterparts to exploit aircraft drag advantages.

$$s = \frac{L}{D}\frac{1}{TSFC}\frac{u_\infty}{g}\ln\left(\frac{m_1}{m_2}\right) \tag{1.1}$$

This is currently not the case.

Propulsion system installations in highly integrated, boundary layer ingestion aircraft rarely operate in nominal inlet flow conditions. Because the flow properties vary within the boundary layer, turbofan engines installed in boundary layer ingestion configurations are exposed to continuous inlet distortion conditions. These distortions typically consist of non-uniform total pressure and large amounts of secondary flow entering the engine and lead to operability challenges, performance and efficiency degradations, and aeromechanical stress intensification [13,14,23-43].

Before studying the effects of complex inlet flow distortions, it is important to understand the mechanisms that generate the distortions. Inlet total pressure distortions typically arise from low energy boundary layer flow ingestion and flow separation within non-axisymmetric inlet duct geometry. Inlet swirl distortions typically arise from upstream wake shedding, secondary flow mixing, and aggressive flight maneuvers [25,26].

Studies of inlet flow distortion have concluded that turbofan engines operating in continuous distorted inlet conditions suffer significant propulsive efficiency losses, operability margin reduction, and high cycle fatigue intensification. Propulsive efficiency degradation produces thrust specific fuel consumption penalties of up to 15% increase compared to nominal inlet conditions [23,27,35-38]. Rapidly changing fan rotor incidence angle and severe circumferential pressure gradients result in operability margin reduction as the compressor operates closer to stall conditions at lower spool speeds [28-30,39,40]. Due to repeated circumferential distortion patterns, the fan cycles through areas of varying distortion levels, inducing dynamic blade loading, and exacerbating high cycle fatigue [24,31,34,41-43].

These challenges to the propulsion system in highly integrated aircraft deserve attention but it should be noted that system level benefits of engine/airframe integration reduce the propulsive demands and offset degradations in turbofan engine performance and efficiency. Revisiting the Breguet range equation, it can be seen that increasing lift to drag ratio offsets increasing thrust specific fuel consumption for equivalent flight conditions and aircraft weight. Therefore, conventional turbofan engine technology may already be capable of achieving a more efficient flight vehicle in highly integrated aircraft (even with a short term increase in thrust specific fuel

consumption). As engine technology advances to better cope with inlet flow distortion, the thrust specific fuel consumption penalty diminishes and the benefit margin expands.

1.2.3 The State-of-the-Art Turbofan Engine Inlet Flow Distortion Testing

Clearly, a substantial amount of work is still required to understand turbofan engine interactions with inlet flow distortion and to develop mitigation techniques for advancing integrated turbofan engines to performance and efficiency levels equivalent to conventionally pylon mounted counterparts. This work involves reduced order analytical models, simplified and comprehensive computational models, sub-scale and full-scale ground testing, and eventually flight testing leading to airworthiness certification.

The earliest discovered documentation of inlet flow distortion generation for turbomachinery propulsion applications dates back to initial integration of jet engines into military aircraft over half a century ago [44]. The research utilized low porosity screens to produce a 90° sector of reduced total pressure upstream of the initial axial compressor stage. Since then, devices and techniques have been continually upgraded with the primary goal of simulating flight conditions either computationally or experimentally.

Computational analysis has recently become an indispensable tool enabling high-fidelity design verification and rapid iteration at a relatively inexpensive cost compared to most experimental tests. Computational analysis is largely utilized on isolated inlets devoid of turbofan engines to observe baseline distortion profiles or on coupled inlet/turbofan arrangements to observe the impact of inlet manufactured distortions on turbomachinery. The results of these studies are then used to modify inlet design, specify limits of the turbomachinery, or define fluid conditions for experimental ground test replication [45-52].

Turbofan engine inlet flow distortion experimental ground tests are conducted at both sub-scale and full-scale. In both cases, flow conditions can be manufactured by simplified distortion generators or replica inlets operating at realistic flight conditions. At the most complex end of these experimental ground tests, full-scale, powered inlets are tested at operational flight conditions providing the best match of flight conditions. Decreasing the test complexity through the use of sub-scale models provides an excellent representation of flight conditions at reduced operational costs. Isolated or powered inlets are commonly tested in wind-tunnels with scaled conditions closely matching full-scale flight conditions. While the results may not be in exact agreement with full-scale flight tests, design flexibility is gained. [53-58].

Further reduction of experimental complexity results in devices that simulate the flow distortion at the turbofan inlet without the use of complicated, rigid, and often expensive inlet geometry models. While the resulting distortions from such devices may be limited in capabilities of truly representing inlet duct manufactured distortions, rapid design iteration as well as analytical or generic distortions are possible. These devices typically create decoupled distortion elements of separate total pressure and swirl distortion.

Total pressure distortions have been classically generated using loss inducing wire mesh screens as early as the 1950's [44]. Modern total pressure distortion generators use advanced methods for generating tailored total pressure distortion. Varying the porosity or number of wire mesh layers results in custom total pressure distortion generators that produce a specific profile [59-63]. Additive manufacturing has improved the capabilities of total pressure distortion generators with the ability to include continuously variable porosity patterns for high-fidelity profile simulation [64,65]. Recently, actively variable total pressure distortion generators have been deployed to recreate dynamic total pressure distortions through the use of actuated blockage devices [66-68].

Investigations of swirl distortion have been relatively limited when compared to inlet total pressure distortion; however, recently this imbalance has started to close. Swirl distortion generators for inlet flow distortion can be traced back the late 1980's. These devices produced generic swirl distortion profiles relating to ground vortex ingestion and relatively uncomplicated engine inlet geometries [69]. Variable localized vortex generators appeared later which allowed greater flexibility in distortion generation but remained limited to generic distortion profiles due to rigid arrangement of the variable vortex generators [70]. Inlet duct adapters are also currently used to introduce secondary flow distortions perpendicular to the streamwise axis [71-74]. Again, these devices produce relatively generic distortion profiles according to classic swirl distortion patterns. Most recently, StreamVanes have been utilized in turbofan engine ground tests to generate high-fidelity, tailored swirl distortion profiles. These devices consist of a unique arrangement of turning vanes that reproduce secondary flow conditions closely matching desired distortion profiles [75-91].

While total pressure distortion generators and swirl distortion generators simulate decoupled pressure and swirl distortions, the devices fail to accurately replicate the coupled total pressure and swirl distortions generated by inlets operating at realistic flight conditions. Therefore, the current investigation attempts to provide an advanced distortion generator capable of accurate reproduction of combined total pressure and swirl distortions for full-scale experimental turbofan engine ground tests. It is anticipated that the enhanced distortion producing features of this novel device will support integrated engine/airframe conceptual aircraft development and allow greater design flexibility and verification.

1.3 Research Motivation, Objectives, and Hypotheses

Boundary layer ingestion is a potentially revolutionary technology advancement for the aviation industry. Capitalizing on the benefits of boundary layer ingestion requires focused research and development of propulsion system components into integrated engine/airframe configurations. Significant challenges encountered by turbofan engines installed in conceptual next generation aircraft designs center on inlet flow distortion interaction with the initial stages of the turbomachinery. Solving these challenges requires innovative ground test equipment that enhance experimental investigations allowing for design optimization. This ground test hardware must be cost-effective, rapidly produced, easily iterated, and accurate.

Short of full-scale coupled turbofan engine/inlet wind tunnel tests, there currently exists no extensively validated technology capable of accurately simulating complex, non-uniform inlet

flow conditions, composed of both total pressure and swirl distortions, for turbofan engine ground tests. Previously, inlet total pressure distortion elements and inlet swirl distortion elements have been decoupled for ground test purposes. As a contribution to the ongoing turbofan engine integration research efforts throughout the aviation industry, a novel technology, the ScreenVane combined total pressure and swirl distortion device, was invented and motivated the current investigation.

The current state-of-the-art total pressure distortion generators claim profile reproduction accuracy within ±1.0% total pressure recovery while swirl distortion generators claim profile reproduction accuracy within ±1.5° swirl angle. Therefore, as an aggressive goal, the new combined device was intended to match both inlet total pressure and swirl distortion profiles within similar margins. Once validated, the remaining objective of the current research was to quantify effects of inlet distortion on turbofan engine performance and efficiency through component and system analysis.

At the onset of this investigation, the following hypotheses were formulated:

- Inlet duct generated flow distortions can be replicated by a ScreenVane combined total pressure and swirl distortion generator.

- Inlet duct generated flow distortions and ScreenVane generated flow distortions interact similarly with turbofan components.

- Inlet flow distortions alter turbofan engine efficiency and/or performance at both the component and system level.

A series of computational analyses and experimental ground tests were conducted to test each hypothesis. The conclusion of these analyses and tests verify and validate the ScreenVane technology for use in future turbofan engine inlet distortion investigations. By proving this novel device, a new tool will be available for use throughout the turbomachinery and aviation industry.

Chapter 2 – Defining the Distortion

2.1 Overview

The first step toward understanding turbofan engine response to complex inlet flow distortions is to define the distortion profile. This can be accomplished in several ways: analytically, using mathematic equations defining the significant distortion parameters; computationally, using computational fluid dynamics (CFD) models of aircraft/engine/inlet architectures; or experimentally, using data gained via ground or flight testing. Analytical models are the most flexible when specifying a distortion profile as nearly all variables (both flow and geometry related) can be controlled and altered. Computational models are slightly less flexible, requiring geometry specification and adherence to physical laws of fluid dynamics; however, the geometry and fluid properties can be altered with relative ease in the computational domain. Experimental data is the most rigid method of specifying a distortion profile as it requires strict adherence to physical laws of fluid dynamics with relative difficulty of altering geometry or test conditions. While there are no incorrect methods of defining a distortion profile, it should be understood that analytical and computational models can exceed physical laws of fluid dynamics and lead to potentially non-physical flow conditions.

For the current investigation, the distortion profile was defined using computational analysis of a conceptual boundary layer ingesting S-duct turbofan engine inlet. The geometry was modeled at an appropriate scale, and computational analysis was conducted at flow conditions matching the size and capabilities of the turbofan engine ground test platform at the Virginia Tech Turbomachinery and Propulsion Research Laboratory. Defining the initial distortion using a predetermined engine/inlet configuration produced results that were readily applicable to distortion device design. While this analysis approach is not necessarily required, it does remove any scaling of the distortion profile geometrically, aerodynamically, or otherwise.

The following chapter documents a computational case study involving an embedded turbofan engine installation attached to an S-duct inlet subjected to varying amounts of boundary layer flow ingestion. Specifications of the geometry, flow conditions, and analysis settings are explained. Resulting flow profiles extracted at the aerodynamic interface plane (AIP) are then presented to demonstrate the effects of boundary layer ingestion on the flow properties entering the attached turbofan engine.

2.2 The Turbofan Inlet Duct Computational Analysis

2.2.1 Turbofan Inlet Duct Geometry

The turbofan inlet duct selected for the current investigation was based on an embedded turbofan engine installation attached to an S-duct inlet subjected to large amounts of boundary layer flow ingestion. The specific inlet design, designated Inlet-A, was originally developed by NASA as part of a wind tunnel case study examining boundary layer ingestion aircraft and passive flow control for distortion attenuation [92-103]. This inlet was chosen due to the substantial amount of available published literature and the significance of embedded engines in conceptual, next generation aircraft. While this exact inlet may never be installed in an aircraft, it was speculated that many of the associated features and accompanying distortions will be apparent in future integrated airframe/engine architectures.

The single bend turbofan engine inlet duct, shown schematically in Figure 2.1, featured a semi-circular entrance which transitioned into a circular exit with an area expansion (A_e/A_i) of approximately 107%. The duct featured a length-to-diameter ratio (L/D_e) of approximately three exit diameters and an entrance-to-exit centerline shift ratio ($\Delta H/D_e$) of approximately one exit diameter. Table 2.1 summarizes the significant geometric parameters of the NASA provided Inlet-A sub-scale model.

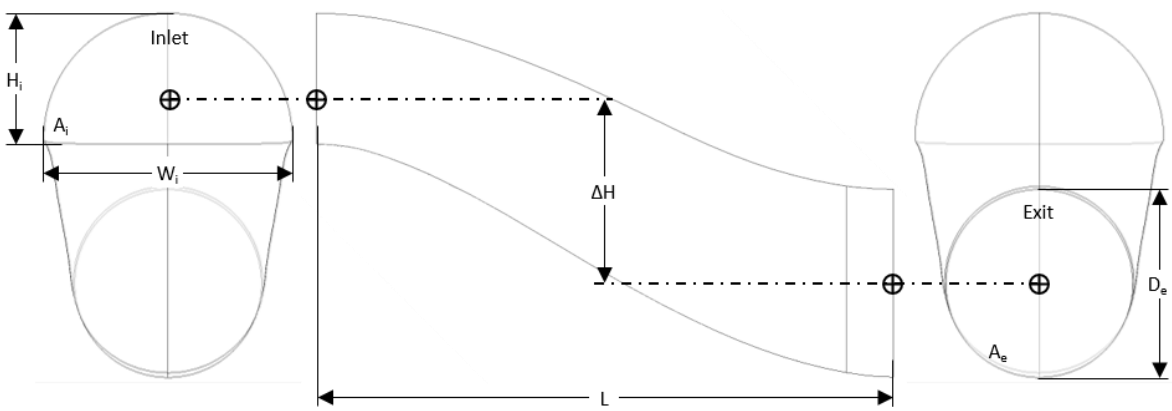

Figure 2.1: S-Duct Turbofan Engine Inlet – Schematic

Table 2.1: S-Duct Turbofan Engine Inlet – NASA Inlet-A S-Duct Geometric Parameters

Length	L	7.539 in
Entrance Height	H_i	1.706 in
Entrance Width	W_i	3.255 in
Entrance Area	A_i	4.402 in^2
Exit Diameter	D_e	2.448 in
Exit Area	A_e	4.705 in^2
Centerline Shift	ΔH	2.543 in
Length-to-Diameter Ratio	L/D_e	3.080
Centerline Shift Ratio	$\Delta H/D_e$	1.039
Area Ratio	A_e/A_i	1.069

The sub-scale model was uniformly scaled to match an exit diameter equivalent to the turbofan engine ground test platform at the Virginia Tech Turbomachinery and Propulsion Research Laboratory. The scaled geometry was designated Inlet-F. Table 2.2 summarizes the significant geometric parameters of the Inlet-F model used in the computational study.

Table 2.2: S-Duct Turbofan Engine Inlet – VT Inlet-F S-Duct Geometric Parameters

Length	L	64.676 in
Entrance Height	H_i	14.632 in
Entrance Width	W_i	27.921 in
Entrance Area	A_i	323.947 in^2
Exit Diameter	D_e	21.000 in
Exit Area	A_e	346.361 in^2
Centerline Shift	ΔH	21.819 in
Length-to-Diameter Ratio	L/D_e	3.080
Centerline Shift Ratio	$\Delta H/D_e$	1.039
Area Ratio	A_e/A_i	1.069

Specification of the aerodynamic interface plane (AIP) was required before computational geometry could be finalized and analysis could commence. This arbitrarily defined plane is often used by airframe/engine designers to identify the transition from the exit of the inlet duct to the entrance of the turbofan engine. For the purpose of this investigation, the AIP was desired to be located sufficiently far downstream of the S-duct circular transition to allow flow reattachment and distortion stabilization yet maintain significant levels of distortion for testing purposes. Based on coarse initial analysis, the streamwise distance between the S-duct circular exit plane and the AIP was selected as one-half the exit diameter. Furthermore, based on the prior existence of experimental ground test hardware, the streamwise distance between the AIP and the fan case inlet flange was fixed at approximately one-tenth the exit diameter. These axial separation distances were accomplished through the use of constant area cylindrical ducts connecting the S-duct circular exit plane to the AIP and connecting the AIP to the fan case inlet flange.

2.2.2 Isolated Computational Domain

In order to obtain a baseline computational flow distortion profile definition, devoid of turbofan engine interactions, two empty cylindrical exit ducts were attached to the Inlet-F S-duct inlet geometry at the circular exit plane. A one-half fan diameter axial length cylindrical duct represented the distance from the S-duct circular exit plane to the AIP. This standoff allowed flow separation from the lower wall of the S-duct to reattach upstream of the AIP. A second empty cylindrical exit duct was attached at the AIP. This five fan diameter axial length cylindrical duct supplied sufficient distance between the AIP and the exit boundary to eliminate boundary condition interactions from propagating upstream to the analysis plane [104]. Figure 2.2 illustrates the isolated computational domain.

The computational domain was discretized using native meshing algorithms [ANSYS CFX]. Unstructured, tetrahedral elements were used throughout the fluid domain to simplify the meshing procedure. Near the outer wall boundaries, a structured inflation mesh was applied to enhance the

resolution within the boundary layer at the fluid-solid interfaces. Table 2.3 summarizes the statistics for the final mesh of the baseline computational domain geometry.

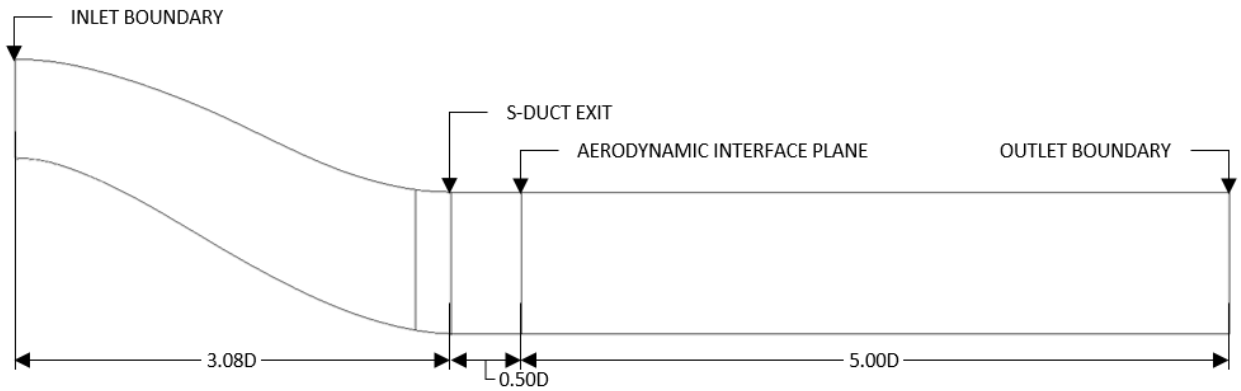

Figure 2.2: S-Duct CFD Case Study – Isolated Computational Domain

Table 2.3: S-Duct CFD Case Study – Isolated Computational Mesh Parameters

Method	Unstructured Tetrahedrons
Element Sizing	0.250 in
Growth Rate	1.10
Inflation, y+	Approx. 25
Inflation, First Layer Thickness	0.004 in
Inflation, Number of Layers	20
Inflation, Growth Rate	1.20
Nodes	Approx. 9.3M
Elements	Approx. 38.0M

2.2.3 Coupled Computational Domain

In order to analyze interactions between the S-duct manufactured distortion and the turbofan engine, a simplified model of the turbomachinery was attached to the Inlet-F S-duct inlet geometry. A one-half fan diameter axial length cylindrical duct represented the distance from the S-duct circular exit plane to the AIP. Next, to represent ground test hardware, a one-tenth fan diameter axial length cylindrical duct was attached at the AIP. The fan case was then attached to the short ground test hardware duct. In this setup, the nose cone of the turbofan engine penetrated the AIP producing an annular, rather than circular, data plane. The radially outward curving wall of the nose cone along with the radially inward tapered fan case produced a significant area reduction from the empty duct case. A five fan diameter axial length annular exit duct was attached to the exit of the fan case. This constant area, annular duct supplied sufficient distance between the AIP and the exit boundary to eliminate boundary condition interactions from propagating upstream to the analysis plane [104]. Figure 2.3 illustrates the coupled computational domain.

The computational domain was discretized using native meshing algorithms [ANSYS CFX]. Unstructured, tetrahedral elements were used throughout the fluid domain to simplify the meshing procedure. Near the outer wall and centerbody surface boundaries, a structured inflation mesh was applied to enhance the resolution within the boundary layer at the fluid-solid interfaces. Table 2.4

summarizes the statistics for the final mesh of the simplified turbofan computational domain geometry.

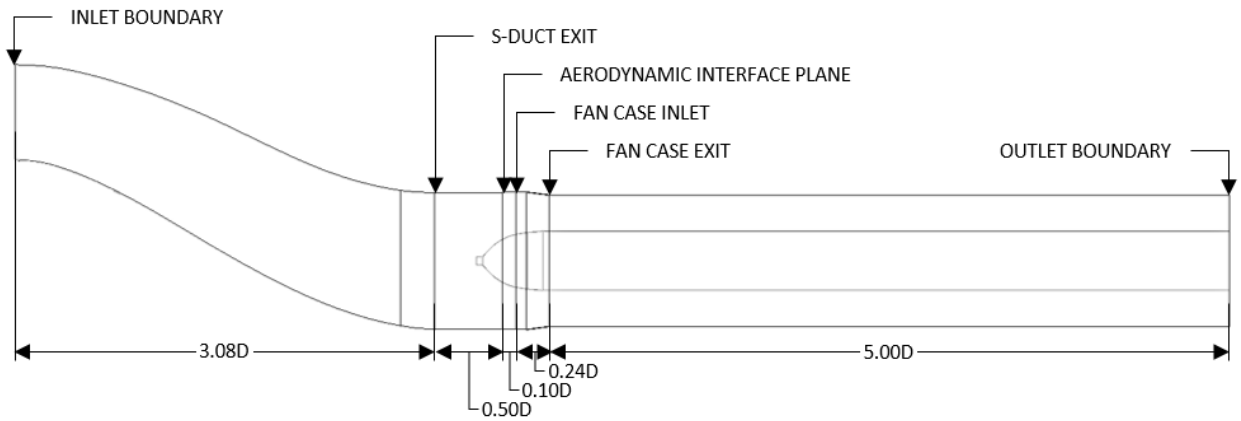

Figure 2.3: S-Duct CFD Case Study – Coupled Computational Domain

Table 2.4: S-Duct CFD Case Study – Coupled Computational Mesh Parameters

Method	Unstructured Tetrahedrons
Element Sizing	0.250 in
Growth Rate	1.10
Inflation, y+	Approx. 25
Inflation, First Layer Thickness	0.004 in
Inflation, Number of Layers	20
Inflation, Growth Rate	1.20
Nodes	Approx. 9.6M
Elements	Approx. 34.8M

2.2.4 Fluid Properties

For both case studies, with and without the centerbody modeled, several parameters were held consistent. In all analyses, a steady state solution was desired for simplicity. The working fluid was set to air with ideal gas assumptions to ensure a compressible solution. The energy equation was coupled with the mass and momentum solution. While no heat or work was added to the working fluid, the energy equation ensured the most complete solution and accounts for any compressibility effects. The k-ω Shear Stress Transport turbulence model was used due to the separated flow conditions associated with the S-duct lower wall. This turbulence model was specifically designed to best predict reattachment length of separated flows and was considered superior to all other steady state turbulence approximations [ANSYS CFX].

2.2.5 Inlet Boundary Conditions

In a realistic integrated airframe/engine architecture, a reduced energy boundary layer forms on the aircraft skin leading into the engine inlet duct. To simplify this boundary layer development, the flow profile entering the S-duct was simulated as a turbulent flat plate velocity boundary layer.

Equation 2.1 defines a turbulent flat plate velocity boundary layer profile as a piecewise function with components inside and outside of the boundary layer. This analytical approach to specifying the inlet conditions agreed well with previously published computational and experimental work [98,99,102].

$$C_z = \begin{cases} C_{z\infty}\left(\frac{Y}{\delta}\right)^{\frac{1}{7}} & , \quad Y < \delta \\ C_{z\infty} & , \quad Y \geq \delta \end{cases} \tag{2.1}$$

The case study examined a varying boundary layer height as a percentage of S-duct inlet height from zero percent to fifty percent in intervals of five percent. Figure 2.4 illustrates the normalized boundary layer profile computed for each boundary layer height percentage.

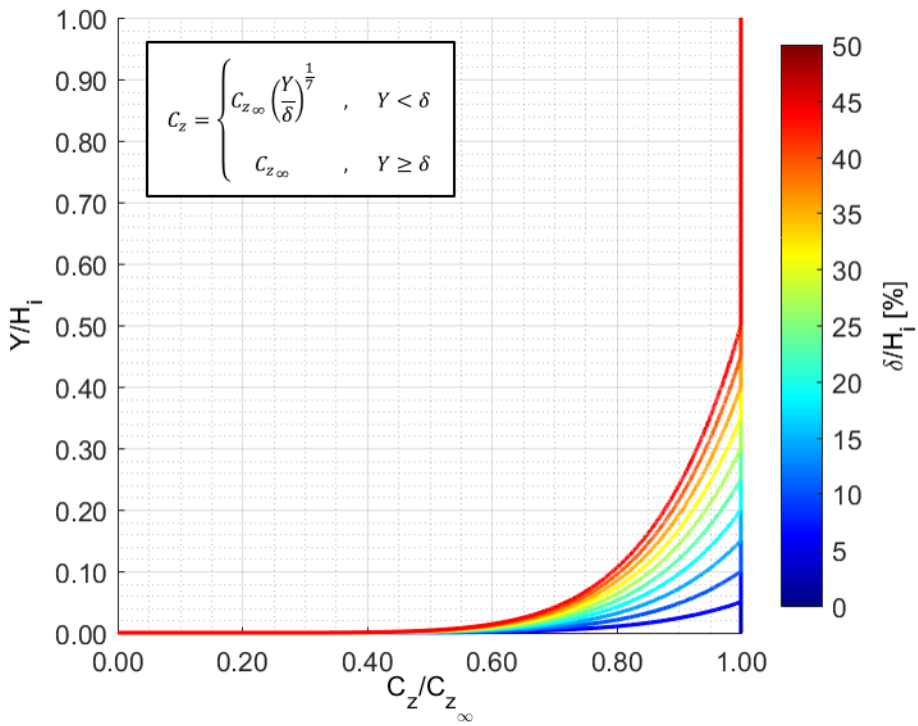

Figure 2.4: S-Duct CFD Case Study – Turbulent Flat Plate Boundary Layer Profiles

The one dimensional normalized turbulent flat plate boundary layer profiles were then mapped to a two dimensional surface equal in size and shape to the Inlet-F entrance. The normalized profile was scaled to an average velocity equal to the velocity generated by a defined mass flow. In the case of Inlet-F, the corrected mass flow rate generated by the turbofan engine ground test platform at test conditions was approximately 50 lb_m/s at sea level standard atmospheric conditions. This mass flow rate equated to an average inlet velocity of approximately 290 ft/s at sea level standard atmospheric conditions. The resulting normalized inlet velocity profiles are shown in Figure 2.5.

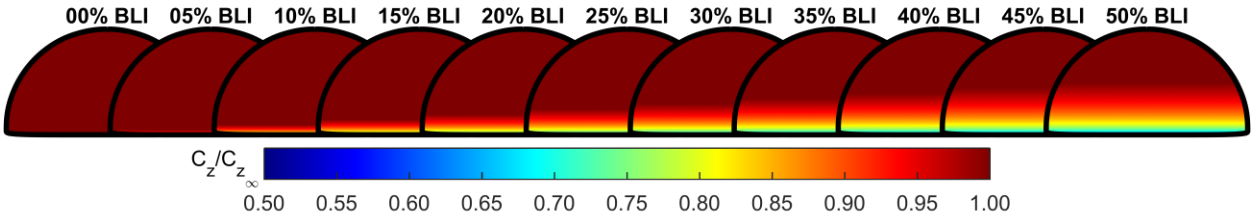

Figure 2.5: S-Duct CFD Case Study – Inlet Velocity Profiles

2.2.6 Outlet Boundary Conditions

The most robust outlet boundary condition for a specified inlet velocity profile is a specified static pressure [ANSYS CFX]. This boundary condition set ensures an explicit calculation of pressure throughout the fluid domain. With the boundary layer inlet velocity profiles set, an iterative approach was utilized to find the average outlet static pressure (with an allowed one percent profile blend). By altering the outlet static pressure, the total pressure was monitored until the maximum total pressure in the duct matched atmospheric pressure within one percent. In the isolated case of Inlet-F, the average outlet static pressure required to drive a mass flow rate of 50 lb_m/s was found to equal 13.696 psia, or exactly 1.000 psi vacuum from atmospheric total pressure. In the coupled case of Inlet-F, the average outlet static pressure required to drive a mass flow rate of 50 lb_m/s was found to equal 13.000 psia, or exactly 1.696 psi vacuum from atmospheric total pressure.

2.2.7 Other Boundary Conditions

In the isolated case of Inlet-F, only the exterior duct wall surface required boundary condition specification. For this analysis, the wall was defined as a no-slip, smooth, stationary wall. In the coupled case of Inlet-F, the exterior duct wall and centerbody surfaces required boundary condition specification. For this analysis, the exterior wall was defined as a no-slip, smooth, stationary wall while the centerbody surface was defined as a no-slip, smooth wall with a rotational velocity equivalent to the experimental test condition (12800 rpm).

2.2.8 Convergence Criteria

In the isolated case of Inlet-F, the convergence criteria for mass and momentum equations was set to an RMS residual of $1x10^{-5}$. The energy equation convergence criteria was relaxed to $5x10^{-5}$ to aid solution convergence and increase solution efficiency. It was assumed appropriate to relax the convergence criteria for the energy equation due to the lack of heat transfer and assumed zero work input to the fluid.

Because the true engine geometry was not modeled in the coupled case of Inlet-F, it was assumed that the computational data would not identically match the experimental data; therefore, to assist in solution efficiency, the convergence criteria for mass, momentum, and energy equations was set to an RMS residual of $5x10^{-5}$. The slightly relaxed convergence criteria produced valuable engineering data without the expense of high precision design data.

2.3 The Turbofan Inlet Duct Computational Results

2.3.1 Total Pressure Distortion Profile

Total pressure distortion results are typically represented as total pressure recovery factors normalized by either the atmospheric total pressure or the maximum in-plane total pressure. Normalizing by the atmospheric total pressure demonstrates the cumulative total pressure changes between the entrance of the inlet duct and the AIP. Normalizing by the maximum in-plane total pressure more appropriately demonstrates only the total pressure changes that the engine will encounter, essentially operating in a reduced total pressure environment. Because the maximum in-plane total pressure measured was within one percent of standard atmospheric pressure, the normalizing factor has no significant difference in the computational study; however, for convenience when comparing to experimental data, the total pressure normalizing factor was selected to be the maximum in-plane total pressure, Equation 2.2.

$$R_0 = \frac{P_0}{\max(P_0)} \tag{2.2}$$

The AIP total pressure distortion profiles exiting the isolated S-duct (top) and coupled S-duct (bottom) are shown in Figure 2.6. The results are presented left-to-right in increasing amounts of boundary layer ingestion percentage. All results are presented forward-looking-aft.

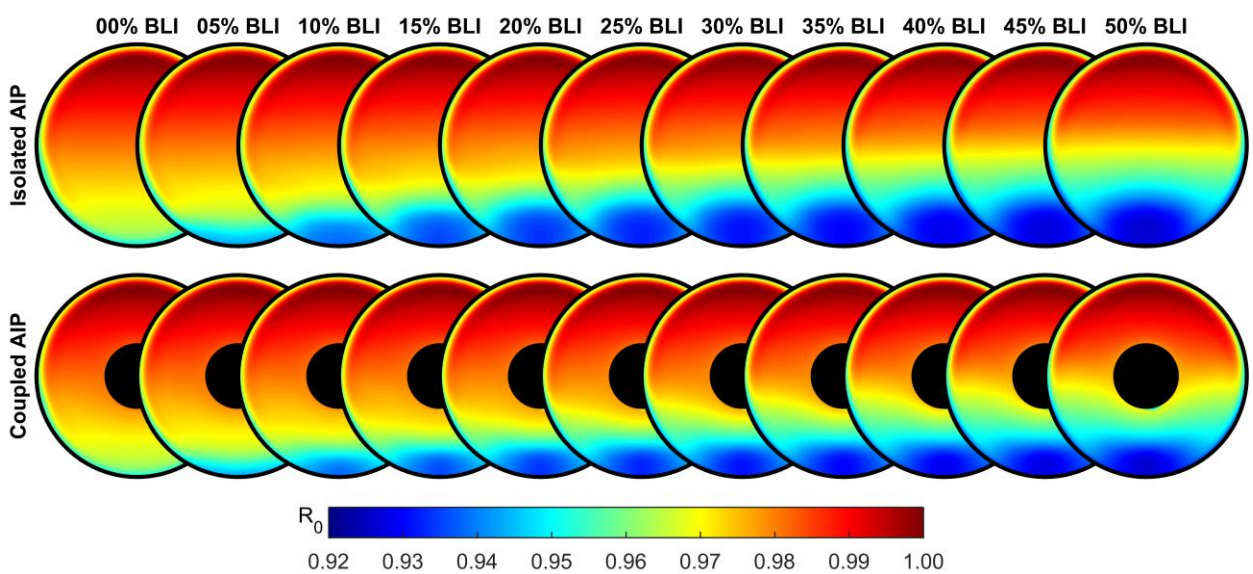

Figure 2.6: S-Duct CFD Case Study – AIP Total Pressure Recovery Profiles

The AIP total pressure recovery profiles illustrated a once-per-revolution low pressure recovery region in the lower semi-circular sector with nearly fully recovered total pressure in the upper semi-circular sector. This profile shape was attributed to exacerbated flow separation along the lower duct wall due to decreased fluid energy entering the inlet from the boundary layer ingestion profiles (Figure 2.5). Further analysis of the geometric symmetry plane (vertical centerline plane), Figure 2.7, better illustrates the onset of flow separation along the lower duct wall.

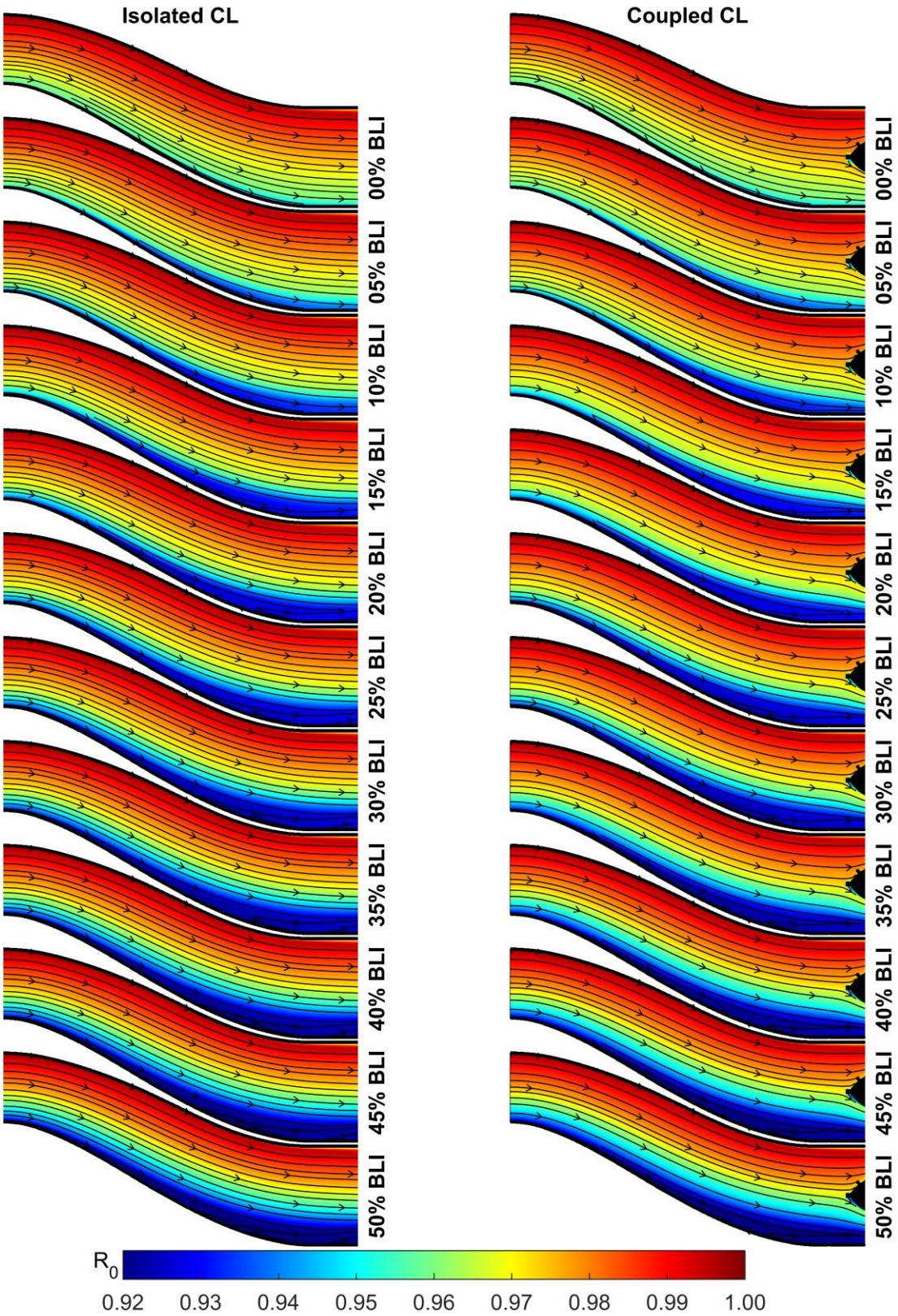

Figure 2.7: S-Duct CFD Case Study – Centerline Total Pressure Recovery Profiles

In both case studies, the severity of the total pressure loss increased with increasing amounts of boundary layer ingestion. The trend had a stronger effect at lower BLI percentages with the extent of the low total pressure recovery region growing significantly. At approximately 25% BLI, the change in extent and intensity of the low total pressure recovery region stabilized, and a nearly constant total pressure distortion profile existed for the remainder of the study results.

The addition of the turbofan nose cone altered the total pressure recovery profile from the isolated case study. With the nose cone modeled, flow acceleration in the axial direction (due to changing area) and flow redistribution (due to solid body avoidance) decreased the extent and intensity of the lowest total pressure recovery region, while increasing the radial total pressure gradients along the vertical centerline.

2.3.2 Swirl Distortion Profile

Swirl distortion arises from the existence of secondary flow, or non-axial fluid motion, within the inlet duct and entering the turbomachinery. This distortion is typically driven by fluid/solid interactions (wake ingestion and/or duct geometry) and flow redistribution (boundary layer ingestion). Swirl distortion is measured as the swirl angle, Equation 2.3, and is a form of circumferential flow normalized by axial flow.

$$\alpha_\theta = \tan^{-1}\left(\frac{C_\theta}{C_z}\right) \tag{2.3}$$

The AIP swirl distortion profiles exiting the isolated S-duct (top) and coupled S-duct (bottom) are shown in Figure 2.8. The results are presented left-to-right in increasing amounts of boundary layer ingestion percentage. All results are presented forward-looking-aft.

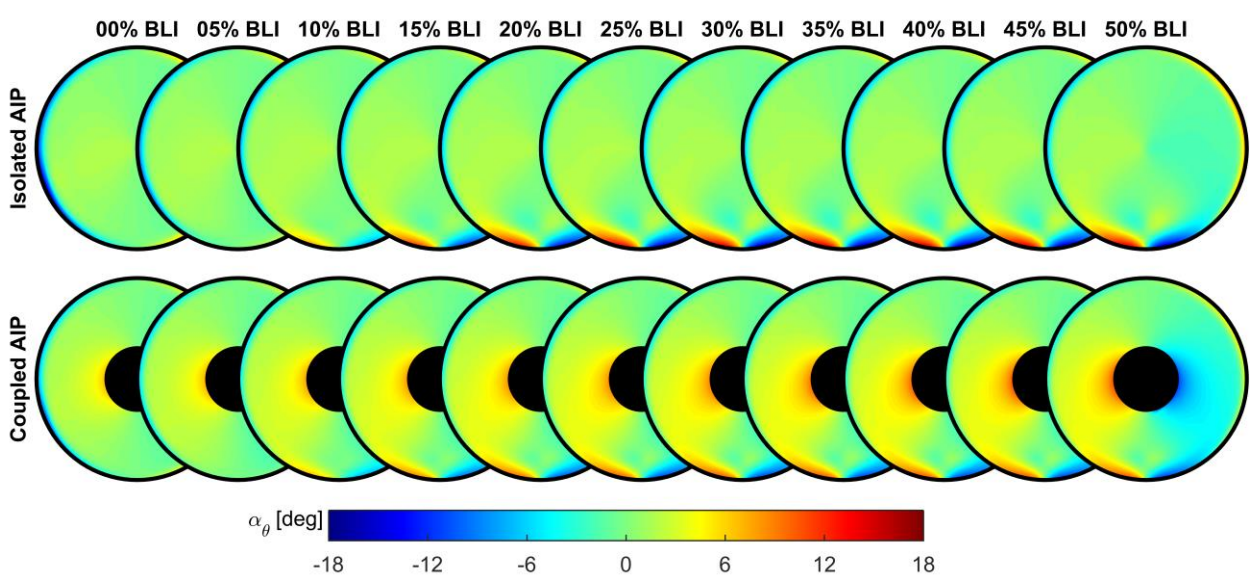

Figure 2.8: S-Duct CFD Case Study – AIP Swirl Angle Profiles

The AIP swirl angle profiles demonstrated the onset of paired-swirl located near bottom-dead-center in the lower semi-circular sector. The ingestion of increasing boundary layer amounts produced low energy flow along the lower duct wall, while the single bend S-duct forces relatively high energy flow downward. The resulting redistribution created a tumbling flow phenomenon exiting the S-duct portion of the inlet. This motion manifested itself in streamwise vorticity as the predominant flow direction returns to axial in the straight duct section.

In both case studies, the amplitude of swirl angle increased with increasing amounts of boundary layer ingestion from BLI percentages of 0% to 20%. At very low BLI percentages (0% and 5%) almost negligible swirl distortion was measured at the AIP. This discovery led to the conclusion that the swirl distortion at these conditions (BLI less than 20%) was primarily attributable to the velocity gradient entering the inlet and flow redistribution as opposed to the fluid/solid interactions with the S-duct geometry. Similar to the total pressure recovery profile, at approximately 20% BLI, the change in extent and intensity of the significant swirl distortion region stabilizes, and a nearly constant swirl angle profile exists for the remainder of the study results. This discovery led to the reversal of the early conclusion; the swirl distortion at these conditions (BLI greater than 20%) was primarily attributable to the fluid/solid interactions with the S-duct geometry as opposed to the velocity gradient entering the inlet and flow redistribution within the inlet.

The addition of the turbofan nose cone altered the swirl angle profile from the isolated case study. With the nose cone modeled, flow acceleration in the axial direction (due to changing area) attenuated the swirl angle intensity in the area of strongest distortion (along the lower wall). Examination of Equation 2.3 explains this phenomenon; without a mechanism to increase the tangential fluid velocity, the swirl angle decreases with accelerating axial fluid velocity. Conversely, the swirl angle near the centerline was increased in the presence of the nose cone. This amplification resulted from flow redistribution (due to solid body avoidance) and increased total pressure gradients forcing fluid direction from areas of relatively high total pressure (upper semi-circular region) to areas of relatively low total pressure (lower semi-circular region).

2.3.3 S-16 Distortion Descriptors

As another method to quantify inlet flow distortions in turbofan engines, the SAE S-16 Turbine Engine Inlet Flow Distortion Committee has developed and issued an Aerospace Recommended Practice (ARP1420) for inlet total pressure distortions and an Aerospace Information Report (AIR5686) for inlet swirl distortions [105,106]. The guidelines outline data collection, processing, and reporting procedures for significant distortion parameters. While many of the parameters require additional information about the turbomachinery (compressor maps, stability margins, and operating limits), distortion intensity values may be obtained using only distorted flow profiles.

In the case of total pressure distortions, the S-16 Committee defines distortion elements in terms or circumferential distortion intensity (Equation 2.4) and radial distortion intensity (Equation 2.5). For swirl distortions, the S-16 Committee defines only the circumferential distortion intensity (Equation 2.6). The intensity values are calculated along concentric radial rings corresponding to centers of equal area annuli. The resulting values are then reported as radial trends at each ith radial ring (Figure 2.9).

$$\left(\frac{\Delta PC}{P}\right)_i = \left(\frac{PAV - PAVLOW}{PAV}\right)_i \tag{2.4}$$

$$\left(\frac{\Delta PR}{P}\right)_i = \frac{PFAV - PAV_i}{PFAV} \tag{2.5}$$

$$SI_i = \frac{SS_i^+ \times \theta_i^+ + |SS_i^-| \times \theta_i^-}{360} = \mathrm{ave}(|\alpha_\theta|)_i \tag{2.6}$$

Where,

$$PAV_i = \frac{1}{360}\int_0^{360} \left(P_0(\theta)\right)_i d\theta = ave(P_0)_i$$

$$PAVLOW_i = \frac{1}{\theta_i^-}\int_{\theta_{1_i}}^{\theta_{2_i}} \left(P_0(\theta)\right)_i d\theta = ave(P_0 < PAV)_i$$

$$PFAV = \frac{1}{N}\sum_{i=1}^{N} PAV_i = areaAve(P_0)$$

$$SS_i^+ = \frac{1}{\theta_i^+}\int_{\theta_i^+} \left(\alpha_\theta(\theta)\right)_i d\theta$$

$$SS_i^- = \frac{1}{\theta_i^-}\int_{\theta_i^-} \left(\alpha_\theta(\theta)\right)_i d\theta$$

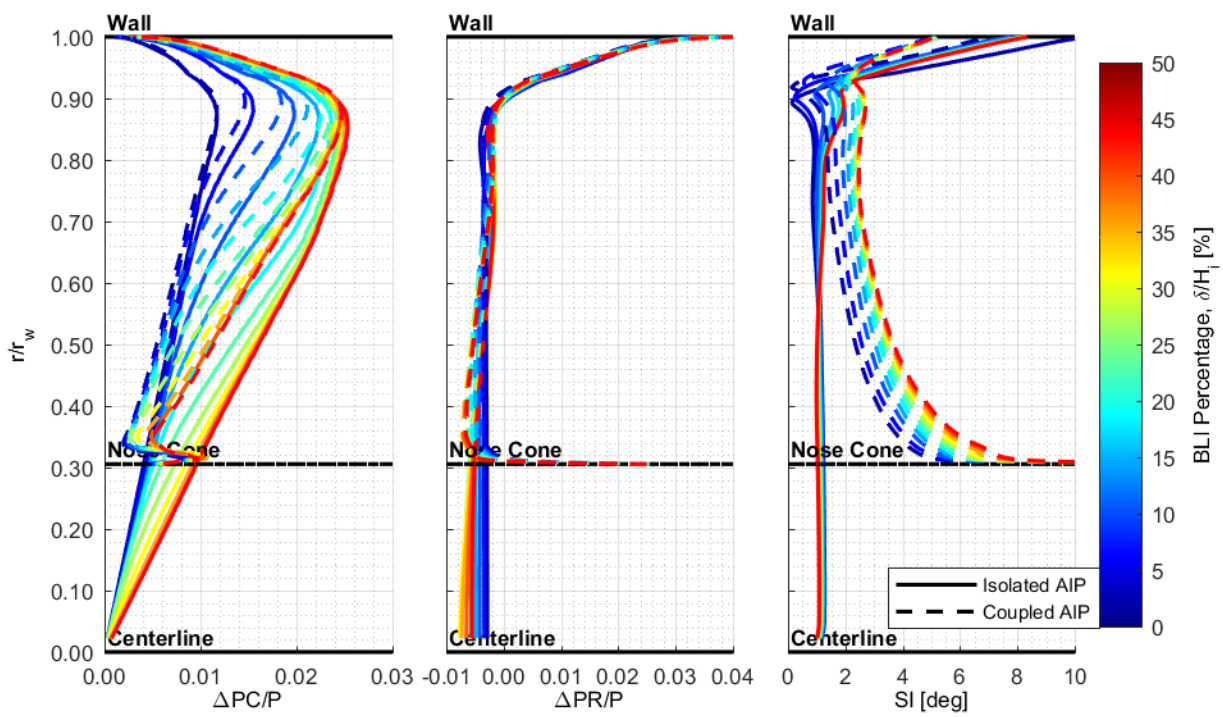

Figure 2.9: S-Duct CFD Case Study – AIP S-16 Distortion Intensity Trends

From the figures, the inlet distortions in this investigation were concentrated near the outer wall. The total pressure circumferential distortion intensity increased from centerline, reached a maximum value at approximately 90% radius, then attenuated along the wall. The total pressure radial distortion intensity and the swirl intensity trends were nearly identical, beginning with negligible distortion at centerline, then rapidly increasing at approximately 90% radius before reaching maximum values at the wall.

The addition of the nose cone geometry had no significant effect on either total pressure distortion intensity parameter, with the only reportable change relating to an increased radial gradient in the circumferential distortion intensity. The swirl intensity was more significantly impacted by the addition of the nose cone geometry. As previously discussed, the flow redistribution associated with the amplified total pressure gradients resulted in increased fluid motion from areas of relatively high total pressure to areas of relatively low total pressure. Aside from one anomaly (swirl intensity at 0% BLI), the maximum values of each parameter increased with increasing amounts of BLI; however, maximum values were observed to remain nearly constant with BLI increasing beyond 20%.

2.4 Summary

A computational case study was conducted to develop a portfolio of turbofan engine inlet flow distortion profiles. A single bend S-duct boundary layer ingesting turbofan engine inlet served as a candidate inlet geometry grounded in reality and relevance. Varying amounts of boundary layer ingestion spanned a predicted range for aircraft inlets of this design. Baseline flow analysis performed with the inlet duct isolated from turbofan hardware was compared to turbofan flow analysis performed with the inlet duct coupled to simplified turbofan hardware.

By systematically varying the amount of boundary layer ingestion, the case study produced corresponding AIP flow profile results with varying extents and intensities of total pressure and swirl distortion. From analysis and observations, the underlying features (including a once-per-revolution total pressure distortion and paired-swirl swirl distortion) of the distortion profiles were largely independent of the amount of boundary layer ingested. This was especially true at the upper end of the tested boundary layer heights, greater than approximately 20% entrance height. Further evaluation of the AIP results indicated that the generated distortions generally increase in intensity with increasing amounts of boundary layer ingestion. This was especially true at the lower end of the tested boundary layer heights, less than approximately 20% entrance height, where distortion intensities rapidly increased in magnitude.

Chapter 3 – Designing the Distortion Generator

3.1 Overview

Due to the complexities associated with ground testing boundary layer ingesting S-duct turbofan inlets at flight conditions, a novel method of replicating specific flow properties matching the S-duct distortion was invented at Virginia Tech: The ScreenVane. This new device combined a total pressure distortion Screen with a swirl distortion StreamVane to simultaneously generate a tailored inlet total pressure distortion and a tailored inlet swirl distortion. The necessity of such a device for turbofan engine ground testing was governed by extreme technical difficulties and expense of the current test methods. Fabricating a full scale inlet duct, generating boundary layer ingestion inlet conditions (either through the use of a wind tunnel or boundary layer fences), maneuvering an asymmetric inlet duct, relocating or duplicating measurement devices to obtain complete data coverage, and rapidly modifying the geometry or flight conditions are just some of the complications solved with a ScreenVane device.

In the current investigation, a single AIP distortion profile from the S-duct turbofan inlet computational case study results was selected as a candidate profile for ScreenVane design, validation, and ground testing. The candidate profile was desired to produce significant levels of combined total pressure and swirl distortion to demonstrate the current state-of-the-art ScreenVane methodology while maintaining realistic flow conditions simulating embedded turbofan engine installations.

The following chapter explains the methodology involved in design and manufacture of the ScreenVane combined total pressure and swirl distortion generator. Down-selection of a single distortion profile candidate is explained. Necessary flow propagation from the desired aerodynamic interface plane to the device design plane is presented. Individual ScreenVane component design and manufacture is then discussed, culminating in the completed design of testable hardware.

3.2 The Desired Distortion Profile

3.2.1 Selection of Aerodynamic Interface Plane Distortion Profile

Computational case studies, such as the one presented in Chapter 2, provide a large amount of information spanning many boundary conditions and allow for relatively inexpensive analysis of

geometry, installation, and condition combinations. At this point, engine/aircraft integration optimization can be performed, geometries can be altered and re-analyzed, and down selection of testable hardware can be finalized. Depending on the application, any or all inlet conditions may be desirable for experimental investigations. Moving from the computational domain to the experimental domain can become relatively expensive and test hardware design is much more rigid; therefore, the number of potential cases, setups, and analyses must be optimized.

For this investigation, down-selection of one candidate distortion profile based on the S-duct case study was performed. This profile was used to generate distortion devices that simulate the inlet flow distortion conditions in the inlet of a full-scale turbofan engine ground test platform. The computational case study of the Inlet-F S-duct resulted in several key findings that assisted in the selection of a single candidate test profile.

- Realistic: The candidate test profile must arise from realistic conditions while advancing the state-of-the-art. Published literature proposes that conceptual boundary layer ingestion aircraft will feature a boundary layer thickness of approximately 25-35% of duct entrance height.

- Significant: The candidate test profile must contain significant distortion elements that are testable. Conventional measurement uncertainties of approximately 1% total pressure recovery and 1.5° swirl angle suggest maximum pressure losses of at least 5% and maximum swirl angles of at least 7.5° to maintain a substantial factor above uncertainty. Results of these magnitudes were discovered for BLI percentages exceeding 15%.

- Multi-use: The candidate test profile should attempt to encompass as many similar distortion elements as possible. Because the S-duct geometry remained constant while the inlet boundary condition was varied, a nearly constant distortion profile was discovered for BLI percentages exceeding 20%.

For the above reasons, the single case for test hardware development was selected to be 25% BLI. This case was determined to align with predicted conceptual aircraft, yield distortion levels that were measurable, and encompass attributes of resulting distortion profiles from over half of the case study.

Figure 3.1 summarizes the AIP total pressure recovery profile for the selected case. The circular cross sections (left) are simply enlarged views of the selected data from the set previously discussed in Chapter 2, Section 2.3.1. The circumferential trends (right) unwrap the distortion profile beginning at top-dead-center (0°), moving counterclockwise through bottom-dead-center (180°), and returning counterclockwise to top-dead-center (360°). The colors displayed here correspond to normalized radius. The total pressure distortion was concentrated near the outer wall, where recovery values experienced the largest fluctuations. In the upper semi-circular region, the total pressure was nearly fully recovered with values greater than 98% for all radii. In the lower semi-circular region, recovery values descended to a minimum of approximately 93% at the outermost radii. All results are presented forward-looking-aft.

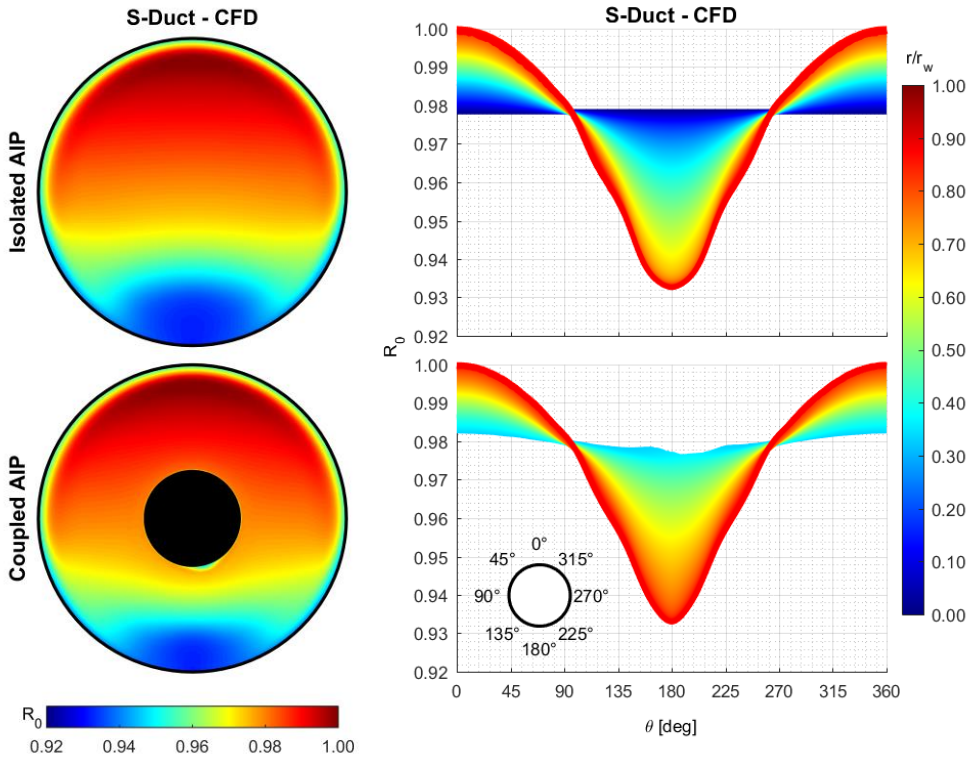

Figure 3.1: S-Duct CFD Analysis – AIP Total Pressure Recovery Profiles and Trends

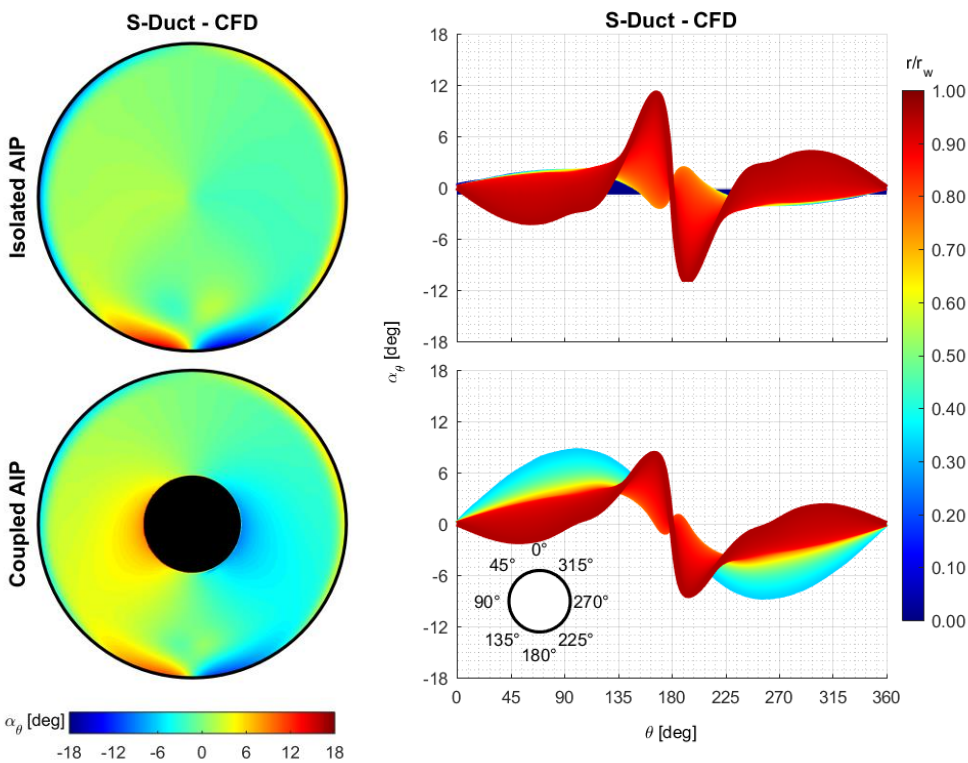

Figure 3.2: S-Duct CFD Analysis – AIP Swirl Angle Profiles and Trends

Figure 3.2 summarizes the AIP swirl angle profile for the selected case. The circular cross sections (left) are simply enlarged views of the selected data from the set previously discussed in Chapter 2, Section 2.3.2. The circumferential trends (right) unwrap the distortion profile beginning at top-dead-center (0°), moving counterclockwise through bottom-dead-center (180°), and returning counterclockwise to top-dead-center (360°). The colors displayed here correspond to normalized radius. Similar to the total pressure distortion, the swirl distortion was concentrated near the outer wall where swirl angles reach maximum values of approximately ±10°. All results are presented forward-looking-aft.

3.2.2 Inverse Flow Propagation to Distortion Generator Design Plane

Installation of the distortion generator upstream of the AIP was required for compatibility with the experimental turbofan ground test facility. Essentially, the physical distortion generator device must be placed upstream of the desired measurement plane to allow for clearance of instrumentation. The ground test facility consists of an assembly of modular cylindrical duct sections attached to the inlet of a turbofan engine. Based on available duct sections, a standoff distance of one diameter between the exit plane of the distortion generator and the AIP was chosen. This distance was considered sufficient for removing unintentional wake effects generated by the submerged solid body of the distortion generator and allowed clearance for experimental instrumentation. It is important to note that the standoff distance is arbitrary and does not necessarily align with distances in the S-duct hardware.

With the desired AIP distortion profile known, a new upstream distortion profile was necessary that, once generated, would develop naturally into the desired distortion profile at the downstream AIP. To accomplish this reverse propagation of the target profile, a reverse vorticity transport method with an ex post facto total pressure and axial velocity correction was employed. This method was related to previously published research [107,108]. The process of reverse propagation of the target profile and prediction of the distortion profile at the upstream device plane advances as follows.

[Note: Specifics regarding the reverse propagation methodology are considered proprietary intellectual property of the Virginia Tech Turbomachinery and Propulsion Research Laboratory. Unfortunately, only a limited overview of the methodology is available at this time. Specific profiles or elements of profiles are designated with numbers while transport processes are designated with letters.]

1) The desired swirl distortion was extracted from the “Isolated S-Duct AIP Profile” computational results for use in Step 2. Because the current state-of-the-art flow propagation solver (StreamFlow^{TM}) was built on vorticity transport theory, a two-dimensional, planar vorticity profile and a temporal term were required. The streamwise vorticity served as the former term while the average axial velocity and desired propagation distance produced the latter. Meanwhile, the total pressure distortion and axial velocity profile were extracted from the “Isolated S-Duct AIP Profile” computational results for use in Step 5.

2) Using the Discretized Poisson's Equation to solve the local stream function, the equivalent "Two-Dimensional Intermediate AIP Profile" was calculated from the streamwise vorticity, effectively reversing Step 1 with the exception of assuming a uniform axial velocity in the calculation.

3) The swirl distortion profile was calculated from the equivalent two-dimensional in-plane velocity profile. The application of a uniform axial velocity profile typically results in an attenuated swirl distortion profile; therefore, a uniform scaling factor is applied to the vorticity profile to minimize the RMSD between the S-duct swirl distortion profile and the equivalent two-dimensional in-plane swirl distortion profile. This new profile is considered the "Two-Dimensional Best Match AIP Profile".

   A) Employing the incompressible, inviscid vorticity transport theory, the scaled streamwise vorticity from Step 3 was reverse propagated using the vorticity transport equation with a negated temporal term equivalent to the ratio of propagation distance to average axial velocity.

4) Using the Discretized Poisson's Equation to solve the local stream function, the upstream "Two-Dimensional ScreenVane Design Profile" was calculated from the propagated streamwise vorticity.

5) The desired total pressure and axial velocity profiles were extracted from the "Isolated S-Duct AIP Profile" and combined with the "Two-Dimensional Best Match AIP Profile". The resulting profile ("StreamFlow Best Match AIP Profile") was considered the best possible match of three-dimensional combined total pressure and swirl distortion achievable using the current-state-of-the-art ScreenVane technology.

   B) Using the resulting flow profiles from Step 4 and Step 5 as the temporary upstream and downstream flow conditions, respectively, streamlines connecting the planes were approximated.

   C) Using the streamlines from Method B as particle tracks, the total pressure distortion profile and the non-uniform axial velocity profile were mapped upstream as convected terms. The current state-of-the-art assumed inviscid, non-mixing flow conditions within the relatively short length of propagation for these terms.

6) The propagated two-dimensional swirl distortion profile from Step 4 was finally corrected using the non-uniform axial velocity profile convected using Method C. The updated swirl distortion profile along with the propagated total pressure distortion were then used as the "ScreenVane Design Profile" for the Screen and StreamVane distortion devices.

Figure 3.3 summarizes the StreamFlow Inverse Flow Propagation Methodology. Beginning on the far right hand side, Step 1 (outlined in blue) correspond to AIP results from the computational analysis of the isolated S-duct inlet. Steps 2, 3 and 5 (outlined in red) corresponds to desired AIP distortion profiles generated by the ScreenVane. Moving to the far left hand side, Steps 4 and 6 (outlined in green) correspond to upstream distortion profiles required for the design of Screen and StreamVane distortion generators. In the center, Methods A, B, and C (outlined in orange, violet, and magenta, respectively) link the design plane and aerodynamic interface plane and explain flow profile propagation techniques.

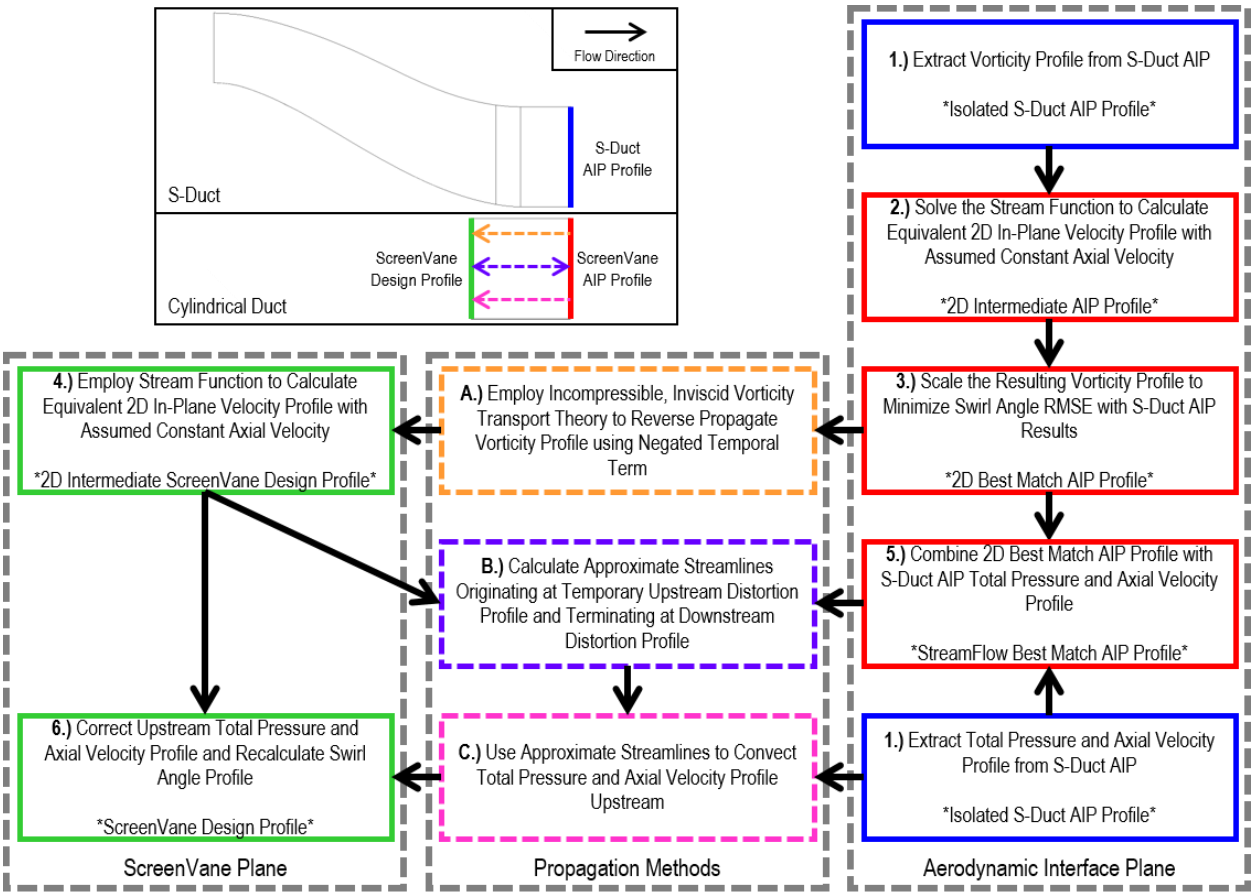

Figure 3.3: StreamFlow Inverse Flow Propagation – Process Map

3.3 The Combined Total Pressure and Swirl Distortion Generator

3.3.1 Total Pressure Distortion Screen

Following the StreamFlow Inverse Flow Propagation Method, the resulting upstream ScreenVane Design Plane (SDP) distortion profile was predicted one diameter upstream of the AIP. The total pressure profile was convected upstream using approximated streamlines connecting the SDP and AIP (Figure 3.4).

The current state-of-the-art distortion total pressure distortion Screen design fabrication process begins with a relatively high porosity, large wire diameter, wire mesh backer screen. The backer screen encompasses the entire circular cross section and ideally produces negligible total pressure losses. The purpose of the backer screen is to allow attachment points for localized, relatively low porosity, loss producing wire mesh distortion screens. In order of increasing fidelity at the expense of increased complexity, the distortion screens consist of either layers of common porosity wire mesh patches, varying porosity wire mesh patches, or a combination of both. The number of layers is directly proportional to total pressure loss whereas porosity is indirectly proportional to total pressure loss.

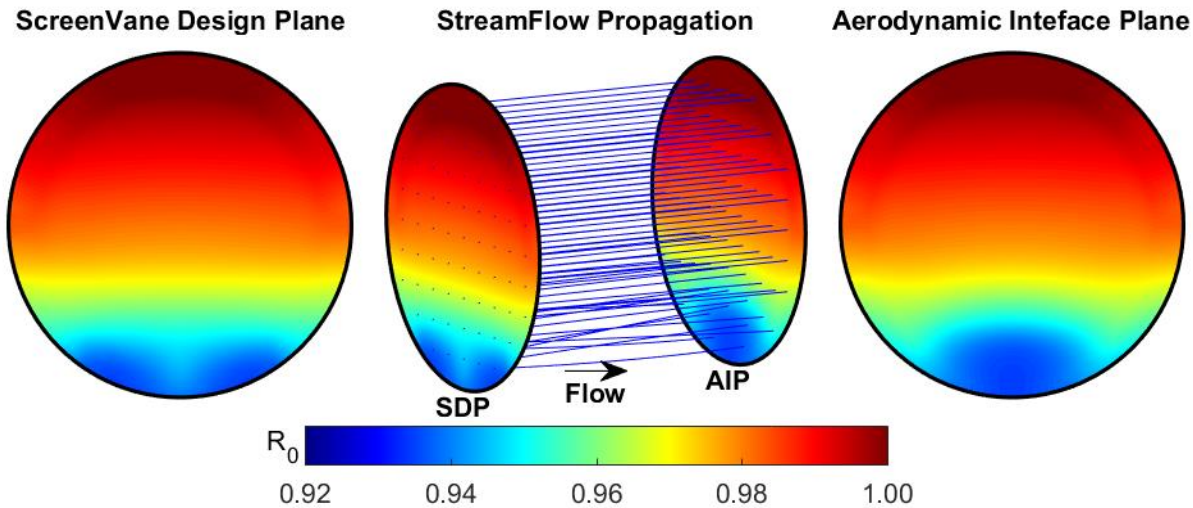

Figure 3.4: StreamFlow Inverse Flow Propagation – Total Pressure Distortion

At this point, engineering decisions regarding Screen design must be made. The selection of an appropriate backer screen was governed by commonly available, rigidly crimped, stainless steel wire mesh. This mesh style was found to be the strongest of conventionally sourced options. An opening size of 1/2" was selected to allow discretized attachment points to 1/2" grid spacing. Of the options available, a wire diameter of 1/16" supplied the greatest porosity of 79% open area.

Next, the distortion screens were specified. Because the desired total pressure distortion consisted of large areas of common recovery, a layered approach using common porosity distortion screens was selected. Again, the selection of distortion screens was governed by commonly available options. For manufacturability, it was desired that the number of layers did not exceed four. With a minimum recovery of approximately 93%, a pressure loss per screen layer of approximately 1.75% (assuming a linear relationship) was necessary. Using the modeling technique outlined in [109] and assuming incompressible flow, the suggested distortion screen porosity was determined to be approximately 70% open area. The nearest commonly available screen with sufficient strength was found to be a 73% open area, 0.057" opening size, 0.010" wire diameter wire mesh.

Layout design of the total pressure distortion Screen began with importing the ScreenVane Design Plane total pressure profile (Figure 3.5, left) and creating a loss model (Equations 3.1-3.6 and Figure 3.5, center) corresponding to the selected distortion screen parameters and assumed inlet flow properties. The continuously varying total pressure recovery profile was then discretized into regions corresponding to an integer multiple of loss per screen (Figure 3.5, right).

From literature [109],

$$\Delta P = K\frac{\rho V^2}{2} \tag{3.1}$$

Assuming incompressible flow and satisfying continuity,

$$\Delta P = \Delta P_0 \tag{3.2}$$

$$\Delta P_0 = K\frac{\rho V^2}{2} \tag{3.3}$$

Where,

$$K = \left(\frac{1}{C_d^2}\right)\left(\frac{1-\alpha^2}{\alpha^2}\right) \tag{3.4}$$

And,

$$C_d = \begin{cases} 0.1\sqrt{Re} & , \quad Re < 20 \\ \sim 1.3 & , \quad Re \geq 500 \end{cases} \tag{3.5}$$

Assuming standard sea-level conditions, an inlet Mach number of approximately 0.20, a Reynolds number greater than 500, and a porosity of 73% open area, the normalized pressure recovery per layer of mesh is,

$$\frac{\Delta P_0}{P_{atm}} = 1.45 \tag{3.6}$$

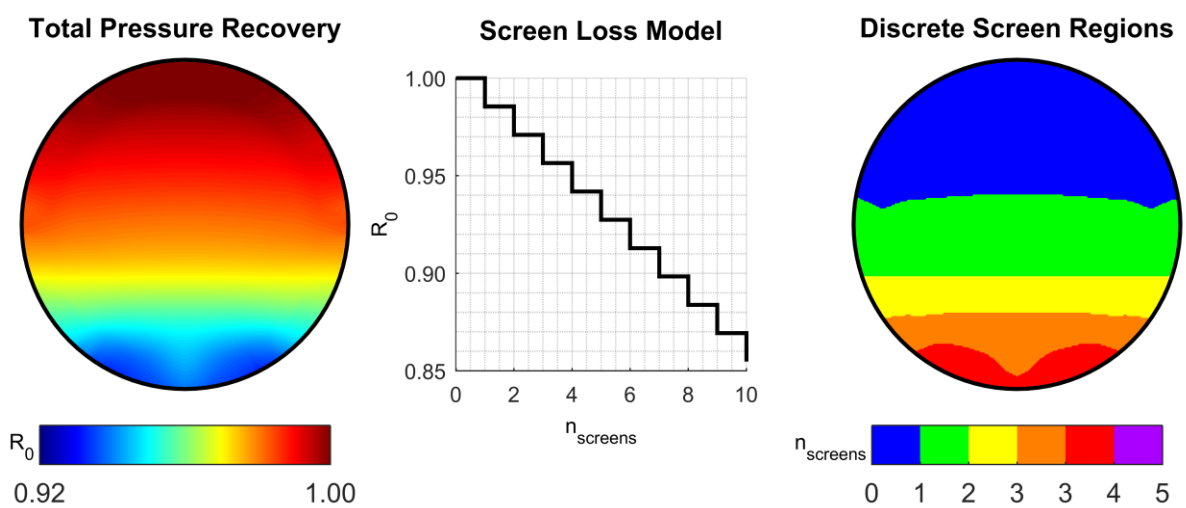

Figure 3.5: Total Pressure Distortion Screen – Layout Design

With the calculated pressure recovery values, the discrete screen zones were then exported to CAD software, automatically assigned a thickness value equivalent to an approximated experimental test device, and converted into solid body geometries for computational analysis (Figure 3.6, left). The turbofan ground test total pressure distortion Screen was fabricated by attaching layers of fine wire mesh distortion screens to a coarse mesh backer screen (Figure 3.6, right). The Screen layout was then clamped into a flanged frame for installation into the inlet duct. Material specified for the Screen was 304 Stainless Steel wire mesh.

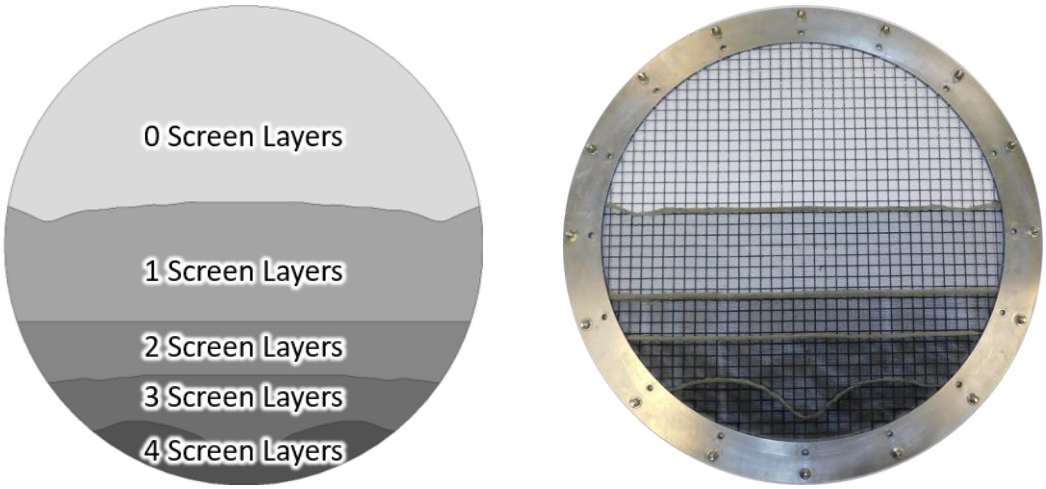

Figure 3.6: Total Pressure Distortion Screen – Device Computational Model (left) and Experimental Device (right)

3.3.2 Swirl Distortion StreamVane

Following the StreamFlow Inverse Flow Propagation Method, the resulting upstream ScreenVane Design Plane (SDP) distortion profile was predicted one diameter upstream of the AIP (Figure 3.7). The swirl angle profile was reverse propagated using a vorticity transport method solved between SDP and AIP.

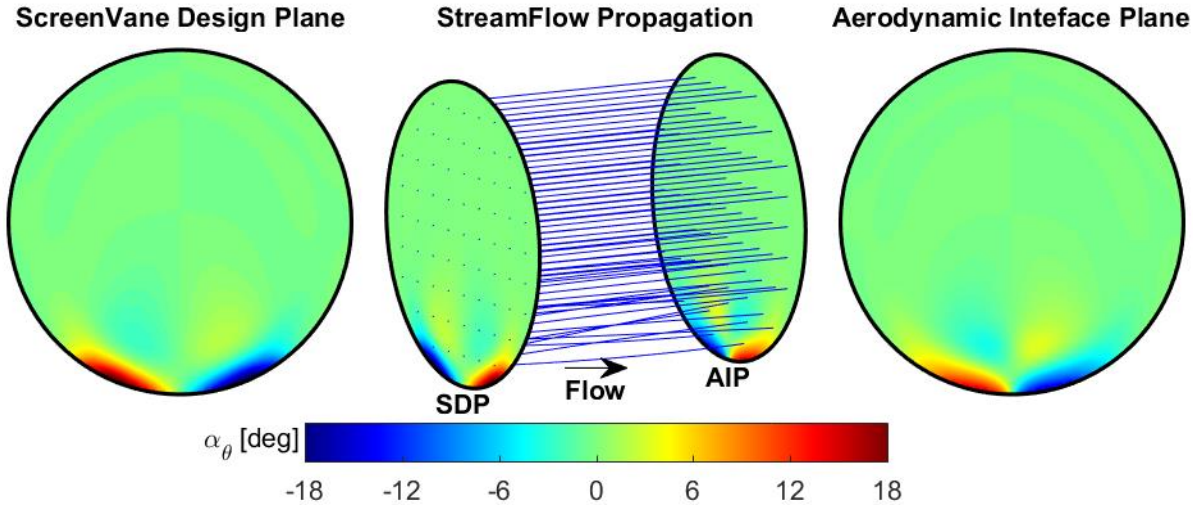

Figure 3.7: StreamFlow Inverse Flow Propagation – Swirl Distortion

Layout design of the swirl distortion StreamVane [75,76] began with importing the ScreenVane Design Plane swirl angle profile (Figure 3.8, left). Next, two-dimensional pathlines were automatically positioned in areas of significant distortion (Figure 3.8, center). Engineering judgement was required to specify a threshold of significant swirl angle, but typical values were angles greater than 1-3°. Below this threshold, swirl distortion intensities were considered negligible, resulting in nearly flat turning vanes, and were ignored. This design decision ensured

proper coverage of the distortion profile without adding unnecessary blockage to the flow path; an important concern when minimizing losses from the swirl generating device and avoiding choke conditions in the inlet. The final step in design was the application of a three-dimensional cambered flat plate thickness profile to each pathline (Figure 3.8, right). The vane thickness was set for manufacturability and strength while the chord length was set for installation into the experimental setup.

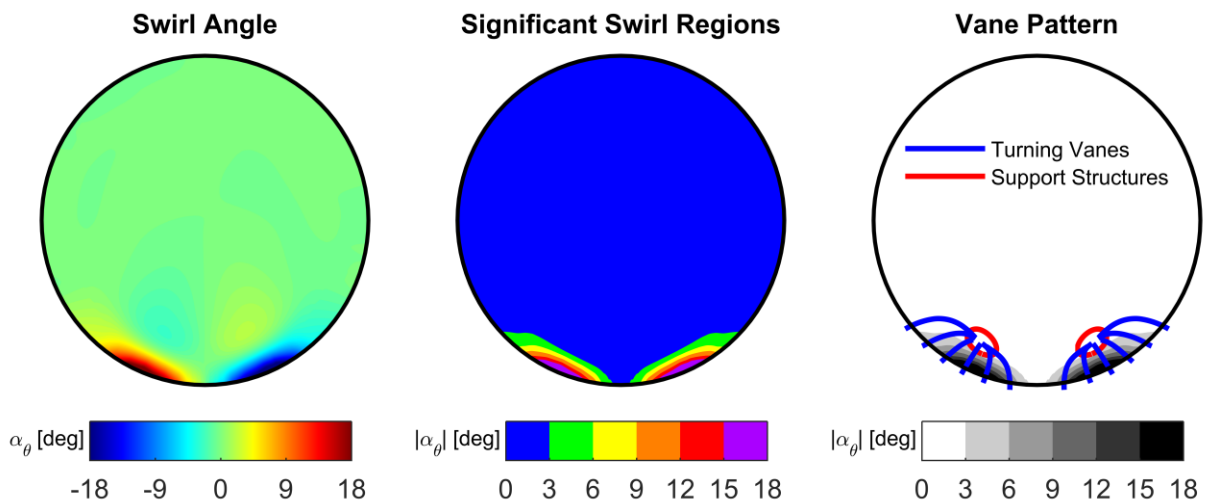

Figure 3.8: Swirl Distortion StreamVane – Layout Design

Figure 3.9: Swirl Distortion StreamVane – Device
Computational Model (left) and Experimental Device (right)

The three-dimensional turning vane coordinates were then exported to CAD software, regenerated, and converted into solid body geometries for computational analysis and manufacture (Figure 3.9, left). The turbofan engine ground test StreamVane was fabricated using large format additive manufacturing (Figure 3.9, right). Individual turning vanes were connected to cylindrical shroud at wall intersection locations and a flange was added for installation into the inlet duct. Material specified for the StreamVane was ULTEM 9085 fused deposition model material.

3.3.3 Combined Total Pressure and Swirl Distortion ScreenVane

The ScreenVane is a novel combined total pressure and swirl distortion generator. As such, very little information regarding the interactions between wire mesh screens and turning vanes existed prior to this investigation [110]. Previous research conducted at Virginia Tech resulted in excellent decoupled total pressure distortions and swirl distortions using conventional wire mesh screens and StreamVanes which led to the concept of a combined device. Unpublished fundamental research suggested that in order to design a valid ScreenVane, the interactions between the two underlying devices must be minimized or accounted for in initial design.

For this investigation, the swirl distortion effects of installing a wire mesh Screen in close proximity to a StreamVane were assumed to be negligible compared to the total pressure distortion implications of installing a solid body StreamVane in close proximity to a wire mesh. The reasoning behind this assumption is the fluid direction exiting the arrangement of turning vanes will remain constant, within a reasonable range, with a changing inlet total pressure or axial velocity profile. Small scale and large scale testing of decoupled StreamVanes suggests that the device operation is largely independent of Mach number [79,80,85,87,91]. On the other hand, solid body blockage in close proximity to the wire mesh decreases the through flow velocity resulting in decreased losses generated by the device.

In the current investigation, the areas of greatest swirl distortion are located in areas of greatest total pressure distortion. While the solid body blockage from the turning vanes reduced the through flow velocity of the nearby layered wire mesh, the solid body itself contributed to total pressure loss via surface friction drag. Thus, the effects were canceled and conventionally designed devices were simply stacked streamwise with the total pressure distortion Screen attached to the leading edge of the StreamVane.

3.4 Summary

In the current investigation, a single AIP distortion profile from the S-duct turbofan inlet computational case study results was selected as the candidate profile for ScreenVane design, validation, and ground testing. The candidate profile was desired to produce significant levels of distortion to demonstrate the current state-of-the-art ScreenVane methodology while maintaining realistic flow conditions simulating embedded turbofan engine installations; therefore, the single case for ScreenVane development was selected to be 25% BLI. This case aligned with predicted boundary layer ingestion amounts found in conceptual aircraft, yielded measurable distortion levels, and encompassed attributes of resulting distortion profiles from over half of the case study. The selection also posed a significant challenge to turbomachinery due to the concentration of distortion near the wall and the increased susceptibility of blade tip stall.

Once the candidate profile was selected, the first step in ScreenVane design involved inverse propagation of the distortion to create an axial separation between the physical device and the measurement plane. The axial separation was necessary for two reasons; to allow wake disturbances to dissipate prior to the measurement plane and to allow for installation into the experimental ground test hardware. The wake disturbances associated with total pressure

distortion screens and swirl distortion StreamVanes created unintentional distortion in the device outlet flow; therefore, it was desirable to allow sufficient streamwise development length to mix these small scale features into the bulk flow. Constraints within the experimental turbofan engine ground test facility also required axial separation between the distortion generators and measurement planes. Based on available hardware and equipment at the facility, the axial separation distance was set to one fan diameter from the ScreenVane design plane (or trailing edge of the StreamVane component) and the aerodynamic interface plane (AIP). The known AIP profile was then projected upstream to the ScreenVane design plane using a vorticity transport method with total pressure corrections. This new upstream profile served as the desired flow conditions to be manufactured by the ScreenVane combined total pressure and swirl distortion device. The flow profile then exited the ScreenVane and naturally developed into the desired AIP distortion profile at the AIP.

ScreenVane design then followed conventional total pressure distortion Screen and swirl distortion StreamVane design practices. The Screen component consisted of varying layers of fine wire mesh installed in the flow to generate tailored total pressure losses according to the desired total pressure distortion profile. The StreamVane component consisted of a unique arrangement of turning vanes installed in the flow to generate the tailored secondary flow according to the desired swirl distortion profile. Combining the two devices by installing the Screen immediately upstream of the StreamVane resulted in the ScreenVane combined total pressure and swirl distortion generator.

Chapter 4 – Analyzing the Distortion Generator

4.1 Overview

Computational analysis of the ScreenVane combined total pressure and swirl distortion generator is useful for design verification prior to manufacture of the physical device. Based on results of this relatively inexpensive analysis technique, designs can be iteratively improved, safety margins can be calculated, and generated flow profiles can be predicted. As the final review of hardware, it is important to confirm the validity of the device and survivability within the ground test facility.

For the current investigation, the ScreenVane porous and solid models produced in the design procedure were readily applicable to computational analysis. These models were inserted into computational domains similar to the S-duct computational analysis procedure previously discussed. The ScreenVane computational analysis was conducted at an appropriate scale and flow conditions matching the size and capabilities of the turbofan engine ground test platform at the Virginia Tech Turbomachinery and Propulsion Research Laboratory. This study produced ScreenVane generated flow data directly comparable to S-duct generated flow data.

The following chapter documents the computational analysis of the ScreenVane combined total pressure and swirl distortion generator. Specifications of the geometry, flow conditions, and analysis settings are explained. Resulting flow profiles extracted at the aerodynamic interface plane (AIP) are then presented and compared to equivalent S-duct distortion profiles at matching conditions.

4.2 The ScreenVane Computational Analysis

4.2.1 ScreenVane Distortion Device Geometry

The ScreenVane distortion device is a combination of a total pressure distortion Screen and a swirl distortion StreamVane and is intended to simultaneously generate a total pressure and swirl distortion profile. In application, the ScreenVane is fabricated by installing the total pressure distortion Screen immediately upstream of the swirl distortion StreamVane. The specific model used in this analysis was designed to simulate the distortion generated by an S-duct turbofan inlet operating in a boundary layer ingesting installation.

The computational model for the total pressure distortion Screen was simulated as a porous domain with defined porosity settings and loss coefficients. Individual domain boundaries were automatically defined using the previously discussed total pressure distortion Screen design methodology in Chapter 3, Section 3.3.1. The computational model for the StreamVane was simulated as a series of custom solid turning vanes. Individual turning vanes were automatically placed using the previously discussed swirl distortion StreamVane design methodology presented in Chapter 3, Section 3.3.2. The computational geometries were then assembled to create the combined total pressure and swirl distortion ScreenVane.

4.2.2 Isolated Computational Domain

As a means of evaluating the design methodology for the experimental investigation, the ScreenVane was first computationally analyzed in an isolated configuration devoid of turbomachinery components. This domain consisted of a two diameter axial length, constant area, cylindrical inlet duct; the ScreenVane computational model; a one diameter axial length, constant area, cylindrical connection duct; and a five diameter axial length, constant area, cylindrical exit duct. The two diameter inlet duct matched experimental turbofan engine ground test hardware. The one diameter connection duct provided sufficient axial separation distance between the ScreenVane exit plane and the AIP. The five diameter exit duct supplied sufficient distance between the AIP and the exit boundary to eliminate boundary condition interactions from propagating upstream to the analysis plane. Figure 4.1 illustrates the isolated computational domain.

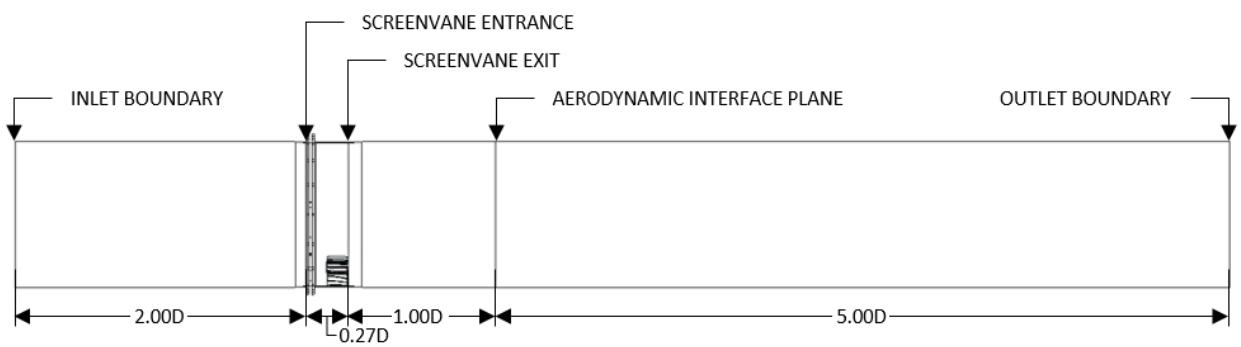

Figure 4.1: ScreenVane CFD Analysis – Isolated Computational Domain

The computational domain was discretized using native meshing algorithms [ANSYS CFX]. Unstructured, tetrahedral elements were used throughout the fluid domain to simplify the meshing procedure. Near the outer wall boundaries, a structured inflation mesh was applied to enhance the resolution within the boundary layer at the fluid-solid interfaces. Table 4.1 summarizes the statistics for the final mesh of the isolated computational domain geometry.

Table 4.1: ScreenVane CFD Analysis – Isolated Computational Mesh Parameters

Method	Unstructured Tetrahedrons
Element Sizing	0.125 in – 0.250 in
Growth Rate	1.10
Inflation, y+	Approx. 25
Inflation, First Layer Thickness	0.004 in
Inflation, Number of Layers	15 – 20
Inflation, Growth Rate	1.20
Nodes	Approx. 13.0M
Elements	Approx. 56.6M

4.2.3 Coupled Computational Domain

In order to analyze interactions between the ScreenVane manufactured distortion and the turbofan engine, a simplified model of the turbomachinery was positioned downstream of the Inlet-F ScreenVane geometry. The coupled domain consisted of a two diameter axial length, constant area, cylindrical inlet duct; the ScreenVane computational model; a one diameter axial length, constant area, cylindrical connection duct; and the simplified turbomachinery geometry. The two diameter inlet duct matched experimental turbofan engine ground test hardware. The one diameter connection duct provided sufficient axial separation distance between the ScreenVane exit plane and the AIP. The fan case was then attached at the AIP. At this location, the nose cone of the turbofan engine penetrated the AIP producing an annular, rather than circular, plane. The radially outward curving wall of the nose cone along with the radially inward tapered fan case produced a significant area reduction from the empty duct case. A five fan diameter axial length annular exit duct was attached to the exit of the fan case. This constant area, annular duct supplied sufficient distance between the AIP and the exit boundary to eliminate boundary condition interactions from propagating upstream to the analysis plane. Figure 4.2 illustrates the coupled computational domain.

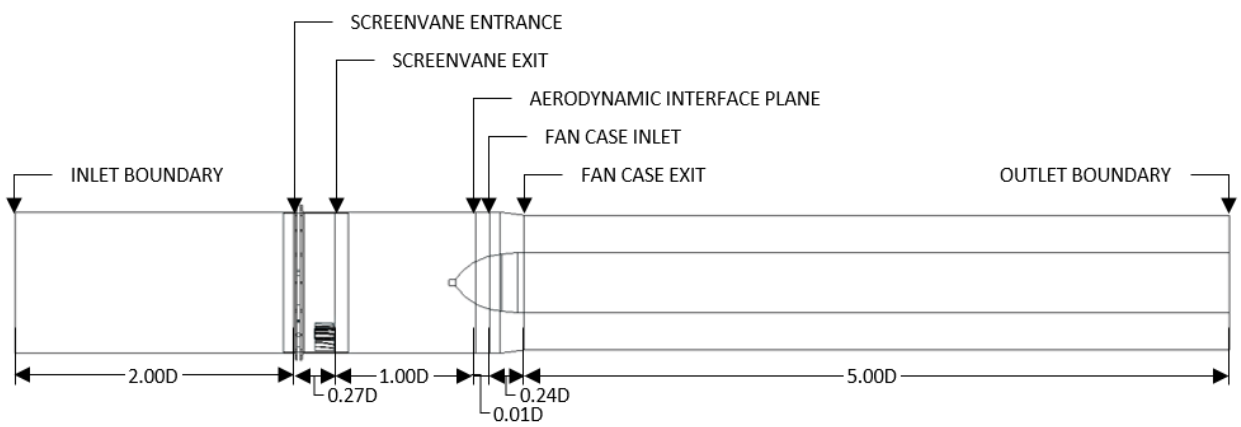

Figure 4.2: ScreenVane CFD Analysis – Coupled Computational Domain

The computational domain was discretized using native meshing algorithms [ANSYS CFX]. Unstructured, tetrahedral elements were used throughout the fluid domain to simplify the meshing procedure. Near the outer wall and centerbody surface boundaries, a structured inflation mesh was

applied to enhance the resolution within the boundary layer at the fluid-solid interfaces. Table 4.2 summarizes the statistics for the final mesh of the simplified turbofan computational domain geometry.

Table 4.2: ScreenVane CFD Analysis – Coupled Computational Mesh Parameters

Method	Unstructured Tetrahedrons
Element Sizing	0.125 in – 0.250 in
Growth Rate	1.10
Inflation, y+	Approx. 25
Inflation, First Layer Thickness	0.004 in
Inflation, Number of Layers	15 – 20
Inflation, Growth Rate	1.20
Nodes	Approx. 13.4M
Elements	Approx. 53.3M

4.2.4 Fluid Properties

For both case studies, with and without the centerbody modeled, several parameters were held consistent. In all analyses, a steady state solution was desired for simplicity. The working fluid was set to air as an ideal gas for the compressible solution. The energy equation was coupled with the mass and momentum solution. While no heat or work was added to the working fluid, the energy equation ensures the most complete solution and accounts for any compressibility effects. The k-ω Shear Stress Transport turbulence model was used due to turning vane surface interactions, small scale separated flow conditions in the wakes of the blunted trailing edges of the cambered flat plate turning vanes, and the possibility of large scale flow separation in regions of high turning. The k-ω SST model was specifically designed to best predict reattachment length of separated flows and was considered superior to all other steady state turbulence approximations [ANSYS CFX].

The distortion screen regions were specified as porous media using the built in model. In addition to setting the fluid properties, porosity settings must be defined. The volume porosity was set to the distortion screen porosity of 73% open area. For simplicity, an isentropic loss model with resistance loss coefficient was utilized. The resistance loss coefficient is a loss parameter per unit axial thickness of the Screen and is necessary since the CFD solver used requires a three dimensional domain rather than an infinitesimal step change. This three dimensional loss coefficient is conveniently calculated from the two dimensional loss coefficient (Equation 3.4) and the desired axial thickness according to Equation 4.1.

$$C_2 = K\frac{n_{screens}}{t_{screens}} \tag{4.1}$$

4.2.5 Boundary Conditions

The fluid conditions for the computational analysis were set to match known corrected fluid conditions in the inlet of the turbofan engine research platform used for experimental ground tests.

Air at standard sea level atmospheric total pressure (14.696 psia) and temperature (59°F) enters the duct at the inlet boundary. A mass flow rate equivalent to the experimental ground test (50 lb_m/s) was set as the outlet boundary condition. This boundary condition pair is considered robust because the velocity at the inlet and the static pressure at the outlet are included in the solution [ANSYS CFX].

In the isolated computational domain, the exterior duct wall surface and the submerged surfaces of the StreamVane turning vanes required boundary condition specification. For this analysis, all wetted surfaces were defined as no-slip, smooth, stationary walls. In the coupled computational domain, the exterior duct wall, the submerged surfaces of the StreamVane turning vanes, and centerbody surfaces required boundary condition specification. For this analysis, the exterior wall and StreamVane surfaces were defined as no-slip, smooth, stationary walls while the centerbody surface was defined as a no-slip, smooth wall with a rotational velocity equivalent to the experimental test condition (12800 rpm).

4.2.6 Convergence Criteria

In all cases, the convergence criteria for mass, momentum, and energy equations was set to an RMS residual of $5x10^{-5}$. This value was sufficient for producing valuable engineering data and for evaluating the ScreenVane methodology at the scales relevant to this investigation.

4.3 The ScreenVane Computational Results

4.3.1 Total Pressure Distortion Profile

Total pressure distortion profiles were extracted at the AIP and are presented in Figure 4.3. The circular cross sections (left) illustrate the full-field planer total pressure recovery as normalized by the maximum in-plane total pressure. From these profiles, the total pressure distortion remained discretized downstream of initiation. This was attributed to the discrete regions of distortion screens used to generate the total pressure distortion. In the lower semi-circular region, the two lobes of low total pressure recovery merged as desired to form a once-per-revolution total pressure distortion.

The circumferential trends (right) unwrap the distortion profile beginning at top-dead-center (0°), moving counterclockwise through bottom-dead-center (180°), and returning counterclockwise to top-dead-center (360°). The colors displayed here correspond to normalized radius. The total pressure distortion was concentrated near the outer wall, where recovery values experienced the largest fluctuations. In the upper semi-circular region, the total pressure was nearly fully recovered with values greater than 97% for all radii. In the lower semi-circular region, recovery values descended to a minimum of approximately 93% at the outermost radii. All results are presented forward-looking-aft.

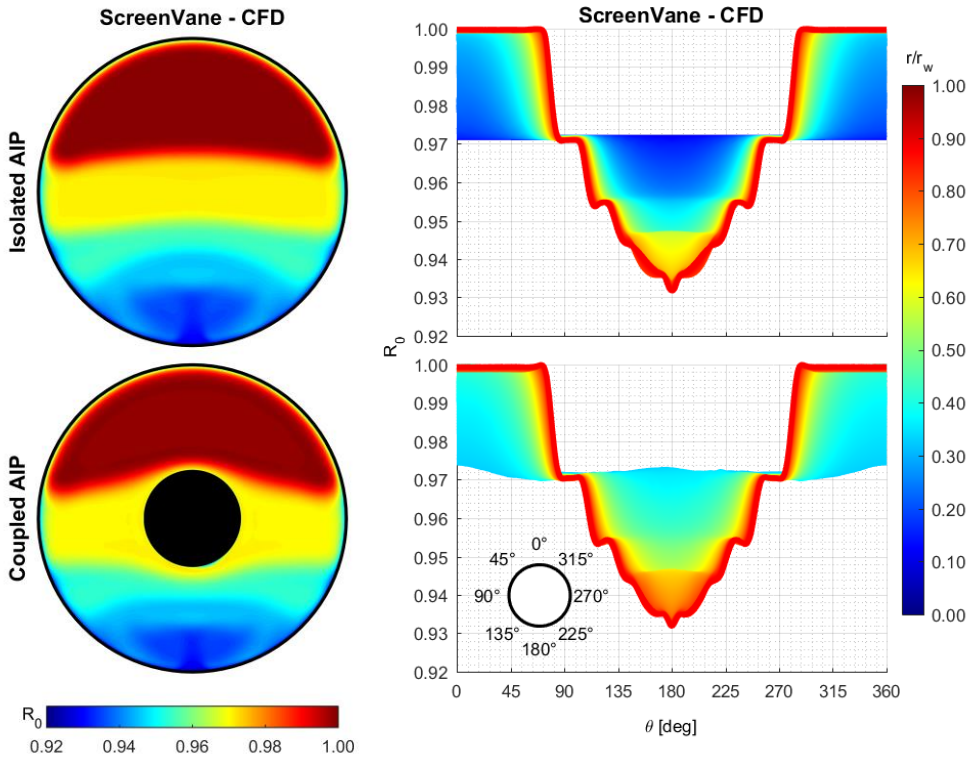

Figure 4.3: ScreenVane CFD Analysis – AIP Total Pressure Recovery Profiles and Trends

Comparing the total pressure distortion profiles from the ScreenVane computational analysis with the S-duct computational analysis provided useful insight into the capabilities of the ScreenVane distortion device. Figure 4.4 illustrates the S-duct computational results, the ScreenVane computational results, and a comparison of results according to Equation 4.2. Further, the RMSD of the entire profile was calculated according to Equation 4.3. Figure 4.5 compares the S-duct computational results and the ScreenVane computational results as circumferential trends of total pressure distortion at the AIP.

$$Comparison = |ScreenVane| - |S\text{-}Duct| \tag{4.2}$$

$$RMSD = \sqrt{\frac{\sum_{n=1}^{N}(ScreenVane - S\text{-}Duct)^2}{N}} \tag{4.3}$$

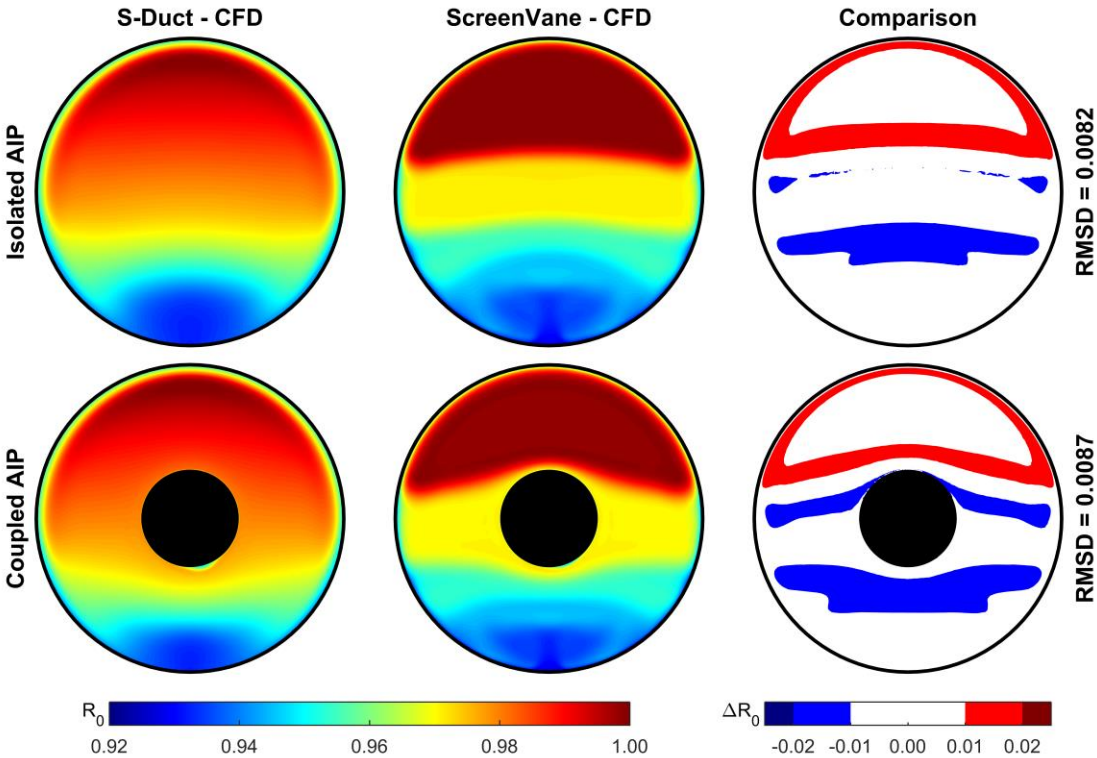

Figure 4.4: ScreenVane CFD Analysis – AIP Total Pressure Recovery Profile Comparison

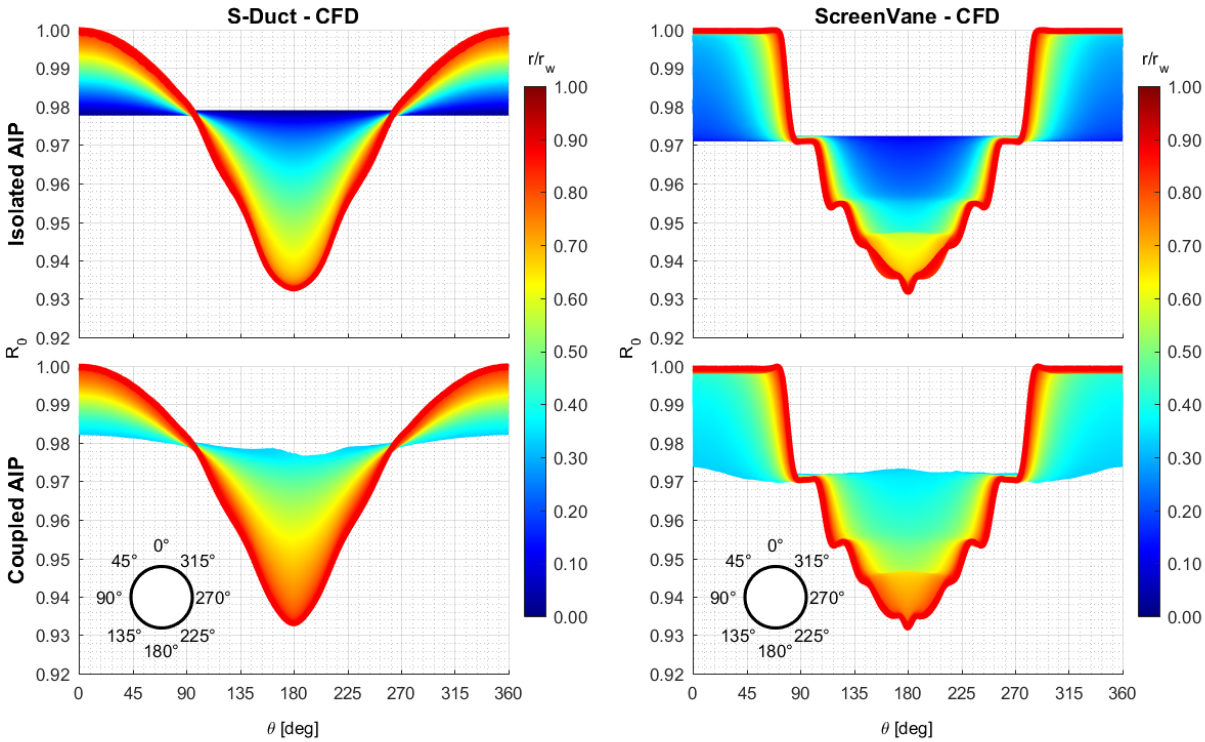

Figure 4.5: ScreenVane CFD Analysis – AIP Total Pressure Recovery Trend Comparison

Qualitatively, the predicted total pressure distortion profile produced by the ScreenVane matched the total pressure distortion profile produced by the S-duct extremely well. The overall shapes, extents, and intensities were appropriately sized and scaled. Quantitatively, the full-field total pressure recovery profile matched within one percent RMSD with largest errors occurring at the interfaces between the varying layer numbers of distortion screens. This error was attributable to discretization of the total pressure distortion profile when designing the total pressure distortion Screen. Further optimization or more complex arrangements of distortion screens could reduce this error; however, as a first attempt at a novel combined distortion generator, these errors were considered acceptable to warrant experimental testing and validation.

4.3.2 Swirl Distortion Profile

Swirl distortion profiles were extracted at the AIP and are presented in Figure 4.6. The circular cross sections (left) illustrate the full-field planer swirl angle. From these profiles, the swirl angle results showed paired swirl in the lower semi-circular region. The incorporation of turbofan engine geometry limited the extent of the vortex pair. The circumferential trends (right) unwrap the distortion profile beginning at top-dead-center (0°), moving counterclockwise through bottom-dead-center (180°), and returning counterclockwise to top-dead-center (360°). The colors displayed here correspond to normalized radius. Similar to the total pressure distortion, the swirl distortion was concentrated near the outer wall where swirl angles reach maximum values of approximately ±15°. All results are presented forward-looking-aft.

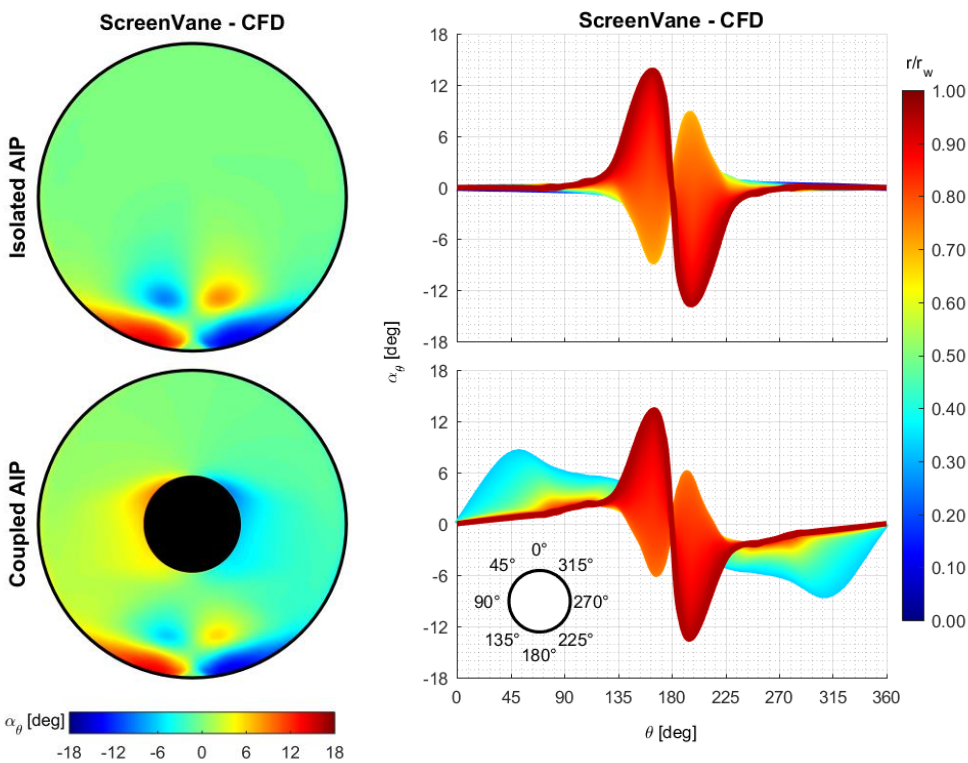

Figure 4.6: ScreenVane CFD Analysis – AIP Swirl Angle Profiles and Trends

Comparing the swirl angle profiles from the ScreenVane computational analysis with the S-duct computational analysis provided useful insight into the capabilities of the ScreenVane distortion device. Figure 4.7 illustrates the S-duct computational results, the ScreenVane computational results, and a comparison of results according to Equation 4.2. Further, the RMSD of the entire profile was calculated according to Equation 4.3. Figure 4.8 compares the S-duct computational results and the ScreenVane computational results as circumferential trends of total pressure distortion at the AIP.

Qualitatively, the swirl distortion profile produced by the ScreenVane contains similar attributes of the S-duct produced distortion. Paired swirl was generated in the lower semi-circular region and persists at the AIP. The overall shape and extent of the distortion was maintained with the ScreenVane generated distortion; however, the ScreenVane produced a slightly more concentrated distortion at bottom-dead-center. The significant difference involved the distortion intensity. The ScreenVane generated distortion was found to have elevated swirl distortion intensity with an RMSD of approximately 2.5°. This discrepancy was likely the result of the vorticity transport method used to inversely propagate the target AIP profile to the device design plane. Further optimization of the inverse propagation technique (such as implementation of a unified three-dimensional transport method) could reduce the error; however, as a first attempt at a novel combined distortion generator, these errors were considered acceptable to warrant experimental testing and validation.

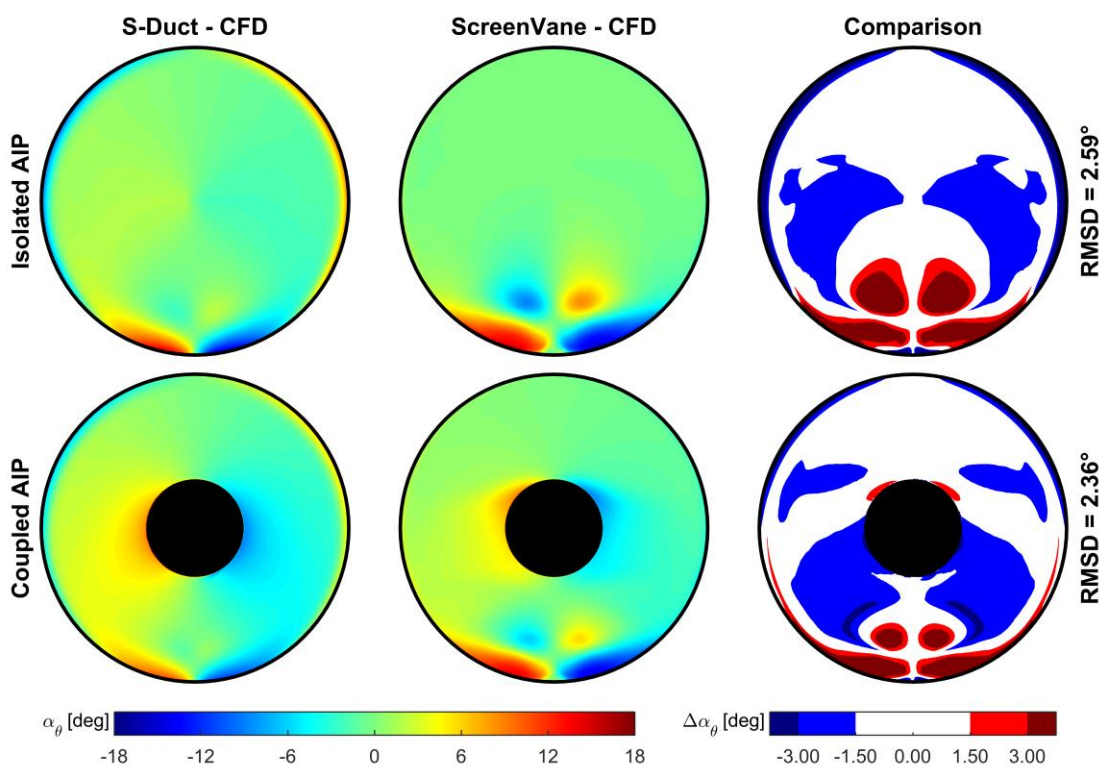

Figure 4.7: ScreenVane CFD Analysis – AIP Swirl Angle Profile Comparison

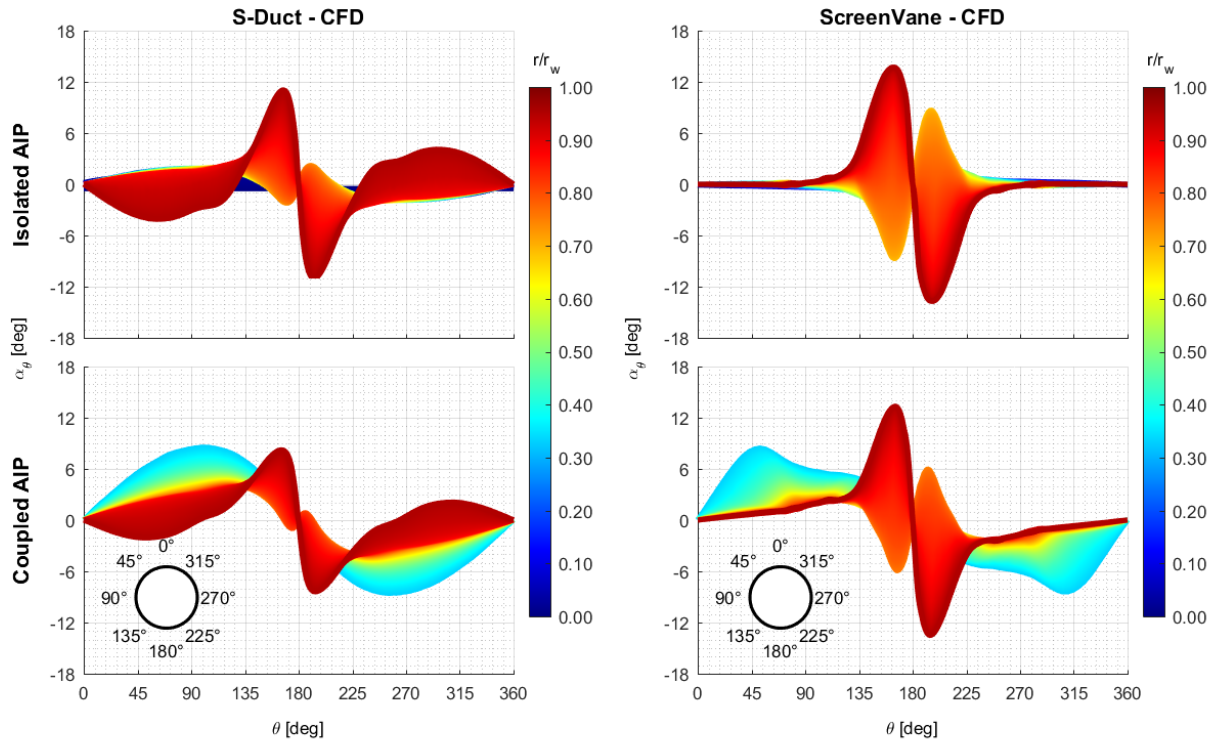

Figure 4.8: ScreenVane CFD Analysis – AIP Swirl Angle Trend Comparison

4.3.3 S-16 Distortion Descriptors

Comparison of the S-16 Distortion Intensity Parameters revealed near perfect agreement between S-duct generated distortion and ScreenVane generated distortion. In both the isolated and coupled geometry arrangements, the total pressure intensity, relative to both circumferential and radial references, was nearly identical. The swirl intensity in the coupled geometry arrangement was also nearly identical. The swirl distortion intensity in the isolated geometry arrangement showed slight disagreement between the S-duct and ScreenVane computational analyses; however, the underlying trend remained consistent.

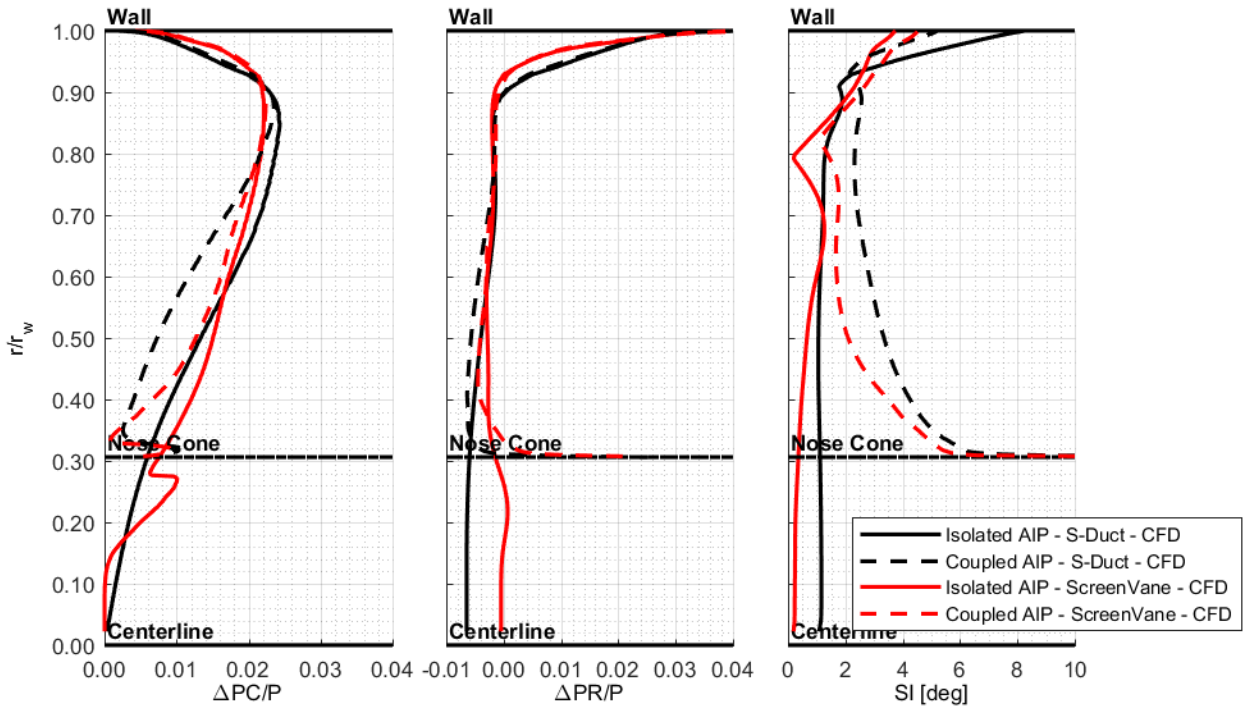

Figure 4.9: ScreenVane CFD Analysis – AIP S-16 Distortion Intensity Trend Comparison

4.4 Summary

Computational analysis of the ScreenVane combined total pressure and swirl distortion generator was conducted to verify that the device manufactured appropriate flow conditions simulating the S-duct turbofan inlet. Of interest, the ability of the ScreenVane to match total pressure recovery and swirl angle profiles at the AIP was quantified. This procedure was necessary to verify and iterate the ScreenVane design prior to fabrication of turbofan engine ground test equipment.

The ScreenVane computational domains were similar to the S-duct turbofan inlet case study. Matching AIP locations were used in isolated and coupled configurations to provide congruent data sets for comparison of S-duct generated flow distortions and ScreenVane generated flow distortions. This process involved modeling the Screen and StreamVane components and subjecting the ScreenVane to turbofan engine inlet flow rates. The Screen component was simulated using porous domain settings that match analytical loss models. The StreamVane component was simulated as a series of solid turning vanes submerged in the inlet flow. Boundary conditions were desired to match the turbofan ground test facility with air ingested at standard atmospheric conditions and propelled to a flow rate of approximately 50 lb_m/s.

ScreenVane generated distortion profiles were extracted at the AIP for analysis and comparison to S-duct generated distortions. Total pressure recovery results demonstrated excellent profile generation and agreement to the desired S-duct total pressure distortion profile. Full-field total pressure recovery error was measured to be less than one percent for both the isolated and coupled

domains. Swirl angle results indicated excellent reproduction of significant distortion features (paired-swirl located near bottom-dead-center) with moderate agreement to full-field error approximated to two and one half degrees. The error was found to be greatly influenced by small discrepancies in distortion gradients; however, as a first attempt at a novel combined distortion generator, these errors were considered acceptable to warrant experimental testing and validation.

Chapter 5 – Validating the Distortion Generator

5.1 Overview

Experimental validation of computation results is considered a best practice for proving methodology, verifying results, and strengthening conclusions. When applicable, experimental validation (either limited or comprehensive) is desirable. Based on the experimental results, computational models can be updated, design practices can be improved, and better distortion devices can be achieved.

The simulation models utilized in the computational analysis had not been rigorously validated prior to this investigation; therefore, an experimental ground test was designed and conducted to produce experimental data in support of ScreenVane design method verification and model validation. The ScreenVane combined total pressure and swirl distortion generator was manufactured, installed, and tested in the inlet duct of the turbofan engine ground test platform at the Virginia Tech Turbomachinery and Propulsion Research Laboratory. Five-hole three-dimensional flow probe measurements at discrete planes within the inlet duct produced experimental results directly comparable to both S-duct and ScreenVane computational results.

The following chapter documents the experimental validation of the ScreenVane combined total pressure and swirl distortion generator. Specifications of the turbofan ground test facility and experimental setup are discussed. Data processing techniques are explained and resulting flow profiles measured at the aerodynamic interface plane (AIP) are then presented and compared to equivalent S-duct and ScreenVane computational results at matching conditions.

5.2 The Turbofan Engine Ground Test Facility

5.2.1 Turbofan Engine Ground Test Platform

Experimental turbofan engine ground tests were conducted using a modified Pratt & Whitney Canada JT15D-1 turbofan engine ground test facility at the Virginia Tech Turbomachinery and Propulsion Research Laboratory. The facility (Figure 5.1) houses a modular inlet system attached to the intake of the turbofan engine and specializes in inlet distortion ingestion research. Along with the turbofan engine and associated control equipment, components of the facility include a mass flow rate calibrated bellmouth inlet, an inlet distortion device mount and rotator, a mobile

five-hole three-dimensional flow probe measurement spool, data acquisition hardware, and automated motion control equipment.

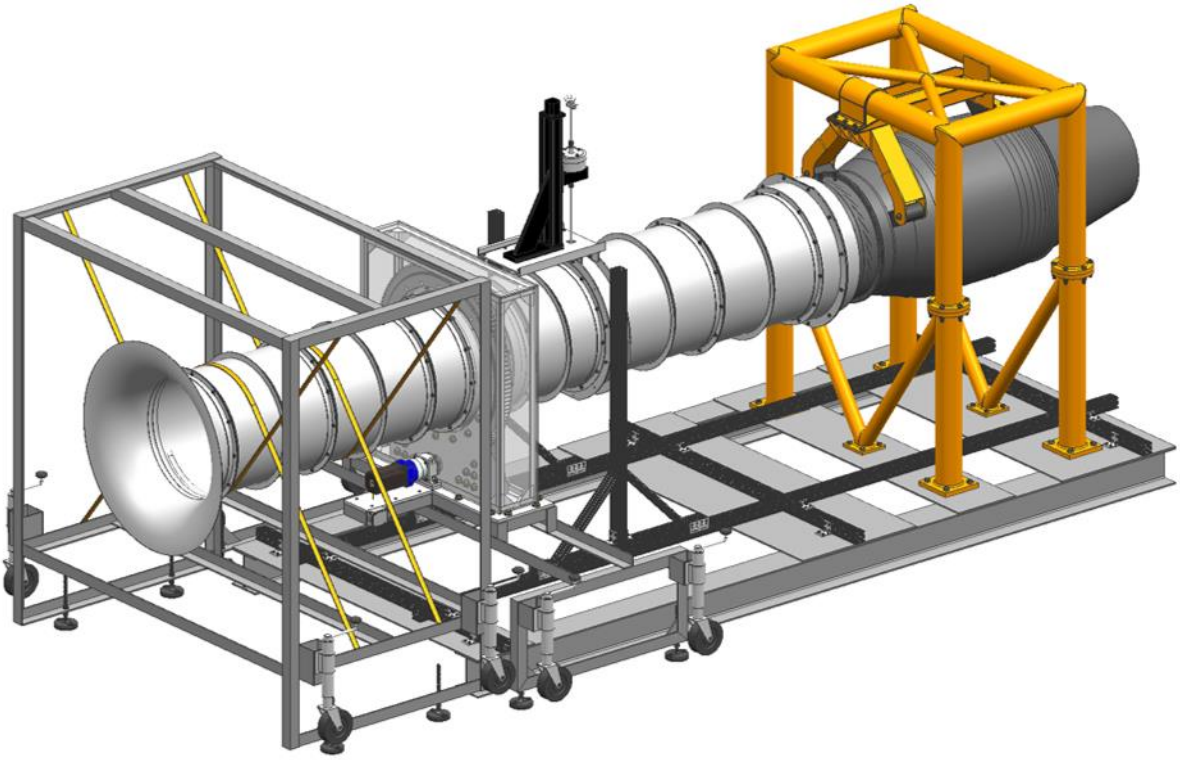

Figure 5.1: Turbofan Engine Ground Test Platform

Utilizing the modularity of the facility, the distortion generators, measurement devices, and turbofan engine can be assembled in various setups depending on the test requirements. Empty cylindrical duct sections can be utilized to isolate the distortion devices far upstream of the turbofan engine, eliminating interactions between the devices and turbomachinery, and effectively creating wind tunnel flow conditions. These empty duct sections can also be removed to allow for close coupling of distortions with the turbofan for investigations of turbomachinery response to inlet flow distortions.

5.2.2 Mass Flow Rate Calibrated Bellmouth Inlet

Air at local atmospheric conditions entered the experimental turbofan engine setup via a bell-shaped inlet adapter attached to a constant area, straight cylindrical inlet duct two diameters in length. The bellmouth inlet ensured smooth flow acceleration and steady flow development while allowing air mass flow rate measurement entering the turbofan engine. Following ASME standard design guidelines, four wall static pressure taps were equally spaced around the circumference of the cylindrical inlet duct at a streamwise distance of one and one half diameters downstream of the bellmouth. The measured static pressure was then interpolated to a calibration curve to determine the inlet air mass flow rate.

5.2.3 ScreenVane Distortion Device

As discussed in Chapter 3, Section 3.3.3, the ScreenVane combined total pressure and swirl distortion generator (Figure 5.2) was manufactured by positioning a conventional total pressure distortion Screen immediately upstream of a conventional swirl distortion StreamVane. The total pressure distortion Screen was fabricated by attaching layers of fine wire mesh distortion screens to a coarse wire mesh backer screen. The Screen layout was then clamped into a flanged frame for installation into the inlet duct. The StreamVane was fabricated using large format additive manufacturing. Individual turning vanes were connected to cylindrical shroud at wall intersection locations and a flange was added for installation into the inlet duct. Materials specified for the Screen and StreamVane were 304 Stainless Steel wire mesh and ULTEM 9085 fused deposition model material, respectively.

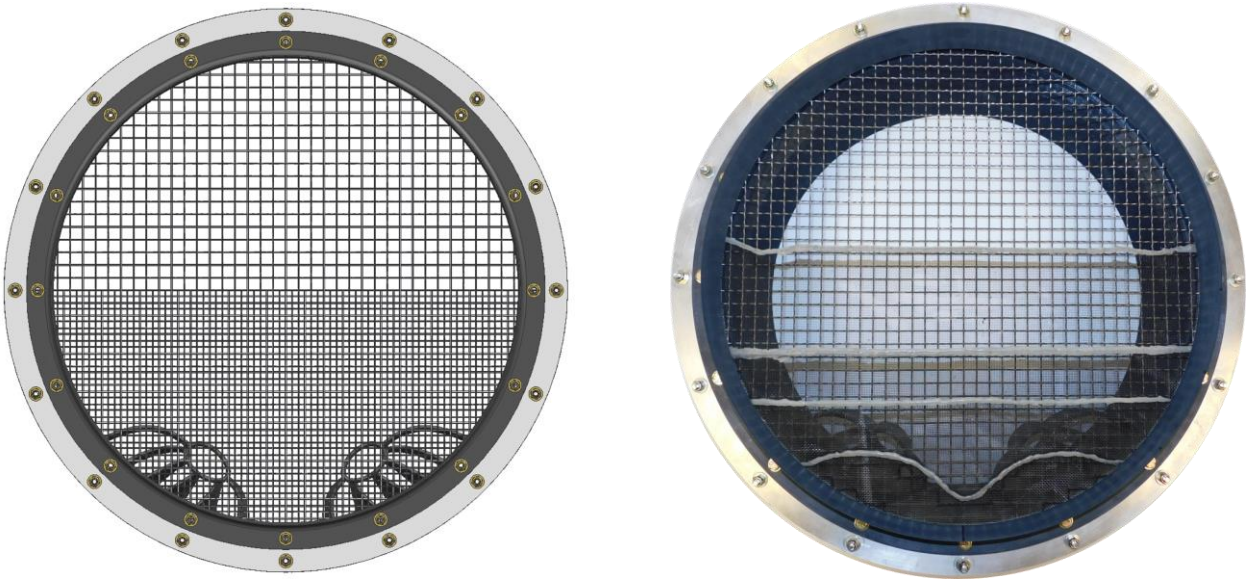

Figure 5.2: Combined Total Pressure and Swirl Distortion ScreenVane – Device

5.2.4 Distortion Device Rotating Mount and Housing

For inlet distortion ground tests, the ScreenVane was installed in a rotating mount and encased in an airtight housing. The rotating mount and housing (Figure 5.3) were necessary for reducing setup complexity; rather than installing multiple data collection devices or moving the data collection devices, the distortion generator was incrementally rotated to revolve the distortion profile. This procedure assumed that the engine hardware was either symmetric or had negligible implications on the distortion development. Because the turbofan engine used in this test includes no upstream hardware (struts, inlet guide vanes, or other), this assumption was satisfied.

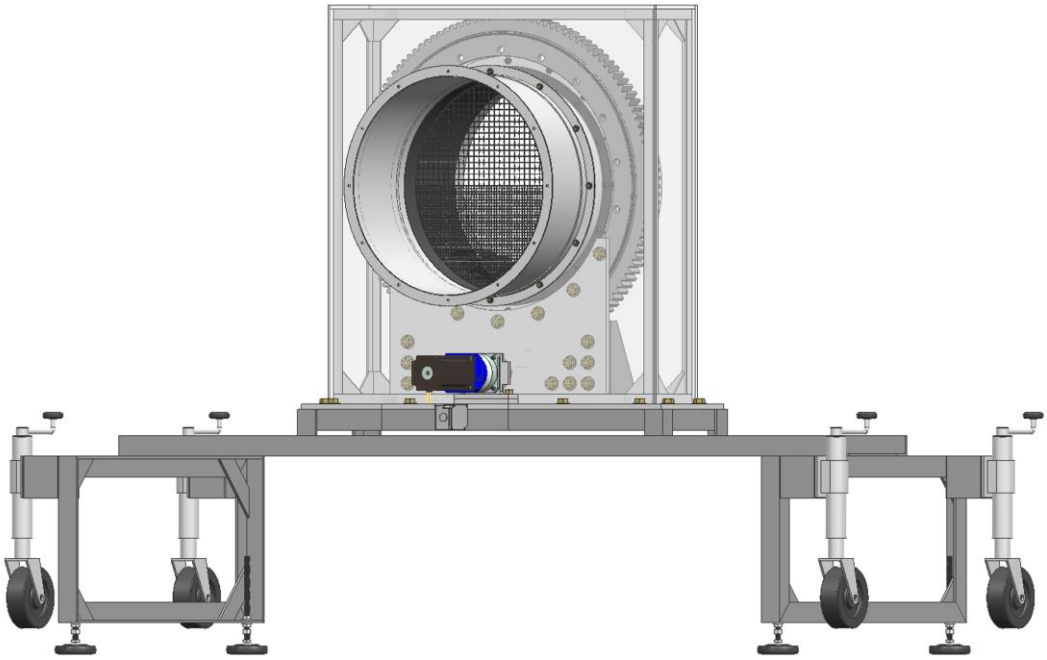

Figure 5.3: Distortion Device Rotating Mount and Housing

A stepper motor (Anaheim Automation – 34Y314S-LW8) connected to a torque multiplying planetary gear box (Anaheim Automation – GBPH-0902-NS-050-AA341-625) rotated a pinion gear (Rotek – P4-3.5D2) which rotated a large slip ring gear bearing (Rotek – L629E9Z(P)). The stepper motor was computer controlled via USB communication with a stepping motor controller (Anaheim Automation – MLA10641). The calculated rotational positioning accuracy of the gear system was approximately ±0.002° and the effective rotational positioning accuracy due to transients and integer step truncation was approximately ±0.010°.

5.2.5 Modified Turbofan Engine

All inlet distortion ground tests were conducted using the modified Pratt & Whitney Canada JT15D-1 turbofan engine. Several important engine parameters are summarized in Table 5.1. A two-stage axial turbine powered a centrifugal core compressor and a twenty-one inch fan producing 2,200 pounds of thrust. The fan rotor of this particular engine model included two design features that made it ideal for inlet distortion testing – a mid-span shroud and a part-span stiffener. These features enhanced the strength and durability of the fan blades, reducing the risk of aeromechanical failure associated with dynamic loading as the fan cycles through the distortion profile. Important fan geometry data are summarized in Table 5.2.

Table 5.1: P&WC JT15D-1 – Engine Parameters at Design (100%) Corrected Fan Speed

Fan Speed	16000 RPM
Fan Blade Tip Speed	1466 ft/s
Mass Flow Rate	73.10 lb_m/s
Fan Pressure Ratio	1.5
Bypass Ratio	3.3
Thrust	2200 lb_f

Table 5.2: P&WC JT15D-1 – Fan Geometry Data

Fan Diameter	21.000 in
Number of Blades	28
Blade Root Chord Length	2.436 in
Blade Tip Chord Length	3.047 in
Blade Root Radius	4.250 in (40% Blade Tip Radius)
Blade Mid-Span Shroud Radius	7.750 in (74% Blade Tip Radius)
Blade Part-Span Stiffener Radius	9.190 in (88% Blade Tip Radius)
Blade Tip Radius	10.500 in (100% Blade Tip Radius)
Core/Bypass Splitter Case Radius	6.500 in (62% Blade Tip Radius)

In addition to conventional engine instrumentation (fan-spool tachometer/generator, core-spool tachometer/generator, inter-turbine-temperature system, and fuel flow meter), the fan case included two penetrations for experimental instrumentation installation. These ports were circumferentially located at top-dead-center within one fan tip chord length axially from the leading and trailing edges of the fan rotor.

5.2.6 Five-Hole Three-Dimensional Flow Probe Measurement Spool

Experimental flow data was collected using a five-hole three-dimensional flow probe with integrated thermocouple (United Sensor – DAT-187-35-J-33-CD-K-LW). Illustrated in Figure 5.4, the 3/16 inch diameter probe featured a prism-style five-hole pressure port arrangement with a shielded thermocouple protruding from the probe tip. The five simultaneously measured pressures were normalized into four pressure coefficients [111] and interpolated to calibration data. The flow parameters measured (via interpolation to calibration data) were radial flow angle, tangential flow angle, total pressure, static pressure, and total temperature.

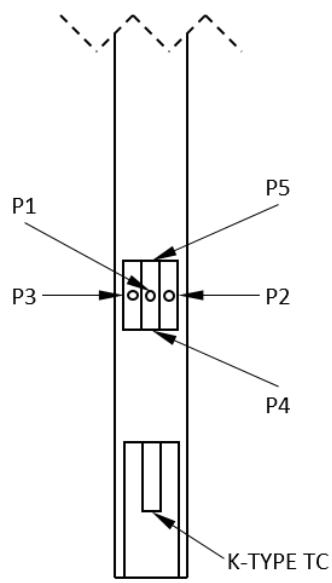

Figure 5.4: Five-Hole Three-Dimensional Flow Probe – Schematic

The probe was mounted to a radial traverse by way of a small rotary table allowing for two degrees of positioning freedom. The radial traverse (Velmex, Inc. – MN10-0150-E01-15) included a

platform attached to a stepper motor driven linear lead screw and allowed the probe sensing area to plunge radially within the flow path. The stepper motor (Vexta – PK266-03B-P2) was computer controlled via RS-232 serial communication with a stepping motor controller (Velmex, Inc. – VXM-2). A manually controlled rotary table (Velmex, Inc. – A4872TS) was attached to the traversing platform and allowed probe alignment with respect to the streamwise axis during installation in the fixture. The entire radial traverse assembly was then mounted to a thick walled cylindrical duct section that could be axially positioned at any streamwise location along the flow path. Figure 5.5 shows a detailed view of the five-hole three-dimensional flow probe measurement spool.

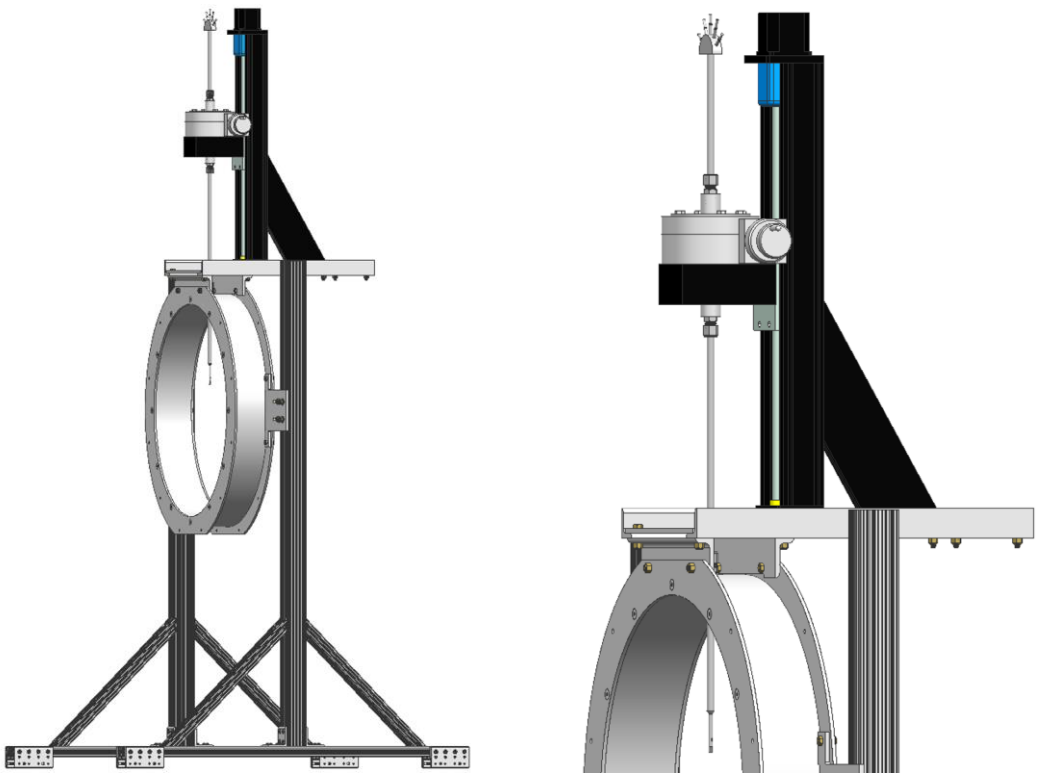

Figure 5.5: Five-Hole Three-Dimensional Flow Probe – Measurement Spool

5.2.7 Data Acquisition System

The fan-spool and core-spool speeds were monitored and measured using on-board tachometer/generators. These devices convert mechanical rotation to an alternating current electrical signal. The frequency of the AC electrical signal is directly proportional to the mechanical rotational speed. The signals were then input to two digital oscilloscopes (Tektronix – TPS 2024B), processed real-time to obtain frequency information, and transmitted to a data collection computer via RS-232 serial communication. The frequency data was then converted to spool-speed and recorded.

Engine fuel consumption was monitored and measured using a fuel flow transducer (Electronics International – FT-180). This device converts mechanical rotation of a fuel flow driven rotor into

a square wave electrical signal indicating revolutions. The frequency of the square wave electrical signal is directly proportional to the mechanical rotational speed of the fuel flow driven rotor. The signal was then input to a digital oscilloscope (Tektronix – TDS 2012C), processed real-time to obtain frequency information, and transmitted to a data collection computer via USB communication. The frequency data was then converted to fuel flow rate and recorded.

The four bellmouth static pressures and the five pressures impinging on the five-hole three-dimensional flow probe were measured using multi-channel pressure scanners (Scannivalve Corp. – ZOC17IP/8Px-APC). The bellmouth static pressures were measured using a ±2.5 psid pressure scanner. AIP five-hole three-dimensional flow probe pressures were measured using a ±5.0 psid pressure scanner. Fan rotor exit plane five-hole three-dimensional flow probe pressures were measured using a ±15.0 psid pressure scanner.

Excitation voltage for the pressure scanners was supplied by two direct current power supplies (Agilent – E3610A) cross-linked to provide ±15.0 VDC. Voltage outputs from the 24 channel pressure scanner assembly were measured and recorded using voltage analog input data acquisition cards (National Instruments – NI 9201) housed in a data acquisition chassis (National Instruments – NI cDAQ-9172) connected to a computer via USB communication.

The inter-turbine-temperature thermopile system and the five-hole three-dimensional flow probe thermocouple temperatures were measured and recorded using K-Type thermocouple input data acquisition cards (National Instruments – NI 9211) housed in a data acquisition chassis (National Instruments – NI cDAQ-9172) connected to a computer via USB communication.

Five second data collection periods were acquired at a sample rate of 100 Hz. Following any motion activities (either radial traverse or device rotator), a three second dwell period was used to allow the flow to reach steady state. Data acquisition and motor control was facilitated through the use of a custom National Instruments LabView software package.

5.3 The ScreenVane Experimental Validation Ground Test

5.3.1 Isolated Experimental Setup

The isolated experimental setup, shown in Figure 5.6, began at the fan case with the turbofan engine mounted in a custom pylon. A thick-walled, 0.37 diameter axial length, constant area, cylindrical inlet duct section was bolted to the fan case using existing hardpoints on the fan case. This empty inlet duct section provided a mounting location for an optical once-per-revolution fan speed sensor. During the course of the current investigation, the engine data acquisition system was improved such that the optical once-per-revolution fan speed sensor was deemed obsolete and was not utilized. The thick-walled inlet duct section remained installed for the isolated test setup and provided additional isolation length, but was removed for the coupled test setup. A thin-walled, two diameter axial length, constant area, cylindrical inlet duct section (isolation duct) was bolted to the thick-walled inlet duct section. The empty inlet duct section allowed sufficient distance to eliminate turbomachinery interactions from propagating forward into the measurement plane. Previous research suggested that turbofan engine components (fan rotor and nose cone)

influence the fluid volume at a distance of up to one half of a diameter upstream [88]. To ensure isolation, the standoff distance was extended to two full diameters. The isolation duct was installed for the isolated test setup, but was removed for the coupled test setup.

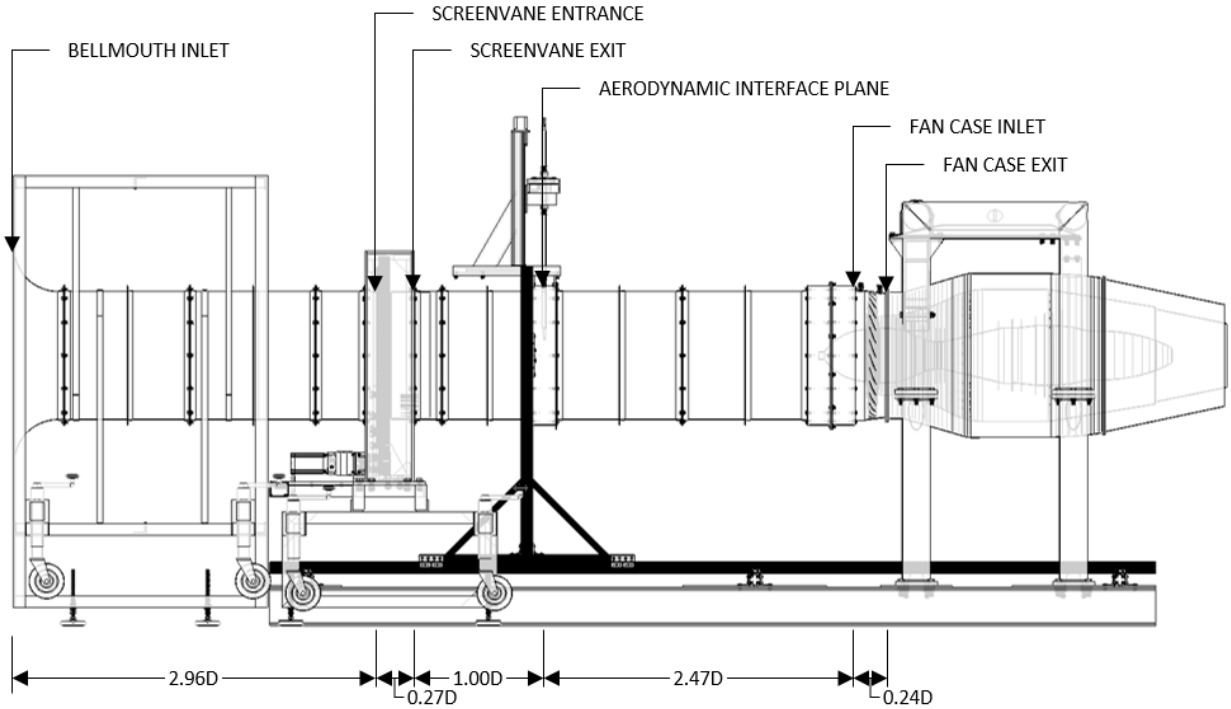

Figure 5.6: ScreenVane EXP Validation – Isolated Ground Test Setup

Continuing upstream, the measurement spool was assembled and installed. First, a thick-walled, 0.20 diameter axial length, constant area, cylindrical inlet duct section was attached to a t-slotted aluminum support frame. The frame supported the weight of the duct section and instrumentation mount, maintained centerline concentricity, and allowed for axial positioning of instrumentation by way of sliding connection to a floor mounted rail system. The downstream flange of the measurement spool was bolted to the upstream flange of the isolation duct. In the coupled experimental setup, the measurement spool was bolted directly to existing hardpoints on the fan case. A universal mounting plate was attached to the thick-walled inlet duct section at top-dead-center and served as a hardpoint for the radial traverse. The radial traverse was then attached to the universal mounting plate, followed by a small rotary table attached to the radially traversing platform. The rotational axis of the small rotary table was aligned with the incorporated measurement spool wall penetration instrumentation port. The radial traverse allowed instrumentation to plunge through the fan case wall and across the flow path. The rotary table assisted with instrumentation alignment during installation.

The five-hole three-dimensional flow probe was inserted through the rotary table and measurement spool wall. Compression fittings on the exterior of the measurement spool as well as the top and bottom of the rotary table secured the probe throughout testing. PTFE ferrules allowed the probe to smoothly plunge radially, while set screw shaft collars located above and below the rotary table mount effectively locked the probe from slipping in the radially traversing mount. Probe installation procedure continued as follows:

1) Install the probe through the rotary table and measurement spool wall compression fittings.
2) Secure the probe within the rotary table using set screw shaft collars to eliminate slip in the radially traversing mount.
3) Retract the tip of the probe just beyond the inner wall of the measurement spool.
4) Using a small piece of thin shim stock placed flush with the inner wall surface, slowly plunge the probe radially inward until probe tip comes contacts the shim stock. At the instant of contact, the probe is radially "zeroed".
5) Set the limit switch of the radial traverse.
6) Install a custom rotary alignment apparatus to the upstream measurement spool flange. The rotary alignment apparatus consists of a stiff aluminum frame and small free-jet tube. The free-jet tube is assumed to be parallel to the engine axis.
7) Plunge the probe radially inward until the probe sensing area is aligned with the small free-jet tube.
8) Connect a handheld digital manometer (Dwyer 477A-1) to the yaw angle sensing ports of the probe.
9) Apply compressed air to the free-jet tube.
10) Exploiting the nulling nature of the prism style five-hole three-dimensional flow probe, rotate the rotary table while monitoring the handheld digital manometer until the measured differential pressure was stable near zero. Once accomplished, the probe is aligned with the streamwise fluid direction.

    [Note: Because testing procedure requires both distorted and non-distorted data collection, perfect probe alignment is not critical. This alignment process is only used to ensure that the probe is nearly nulled with streamwise flow and flow angles are measured in the center of the uniform calibration where greatest accuracy is known.]
11) Remove the custom rotary alignment apparatus and handheld digital manometer.
12) Retract the probe to the zeroed radial position.
13) Connect the five pressure ports to desired pressure scanner channels.
14) Connect the thermocouple plug to the desired temperature acquisition channel.

Next, a thin-walled, 0.70 diameter axial length, constant area, cylindrical inlet duct section (settling duct) was bolted to the upstream flange of the measurement spool. This tunnel section was used to position the ScreenVane at an appropriate upstream location. The offset distance allowed the small-scale wake structures generated by the turning vanes of the ScreenVane device to dissipate before entering the measurement plane and fan rotor.

The ScreenVane rotator was bolted to the upstream flange of the settling duct. The ScreenVane was aligned in the rotator using indexed markings on the ScreenVane shroud and rotator duct wall.

[Note: For the non-distorted baseline test, the ScreenVane was removed from the rotator and replaced by a uniform wire mesh screen. This screen was made from wire mesh identical to that used as the backer screen material for the total pressure distortion Screen. The use of this screen assisted in controlling inlet air mass flow rates for non-distorted baseline tests. Because the flow was assumed uniform in the non-distorted test, five-hole three-dimensional flow probe measurements were taken at the top-dead-center circumferential location at all plunge depths matching the distorted test.]

Finally, the bellmouth inlet was bolted to the upstream flange of the rotator. The static pressure taps (located at one and one half diameters downstream of the bellmouth inlet) were connected to the desired pressure scanner channels.

5.3.2 Coupled Experimental Setup

The coupled experimental setup, shown in Figure 5.7, followed the isolated experimental setup (Section 5.3.1) identically with the exception of the installation of the isolation duct. In this arrangement, the measurement spool was bolted directly to the fan case, positioning the AIP on the nose cone and allowing interactions between the turbomachinery components and the measurement domain.

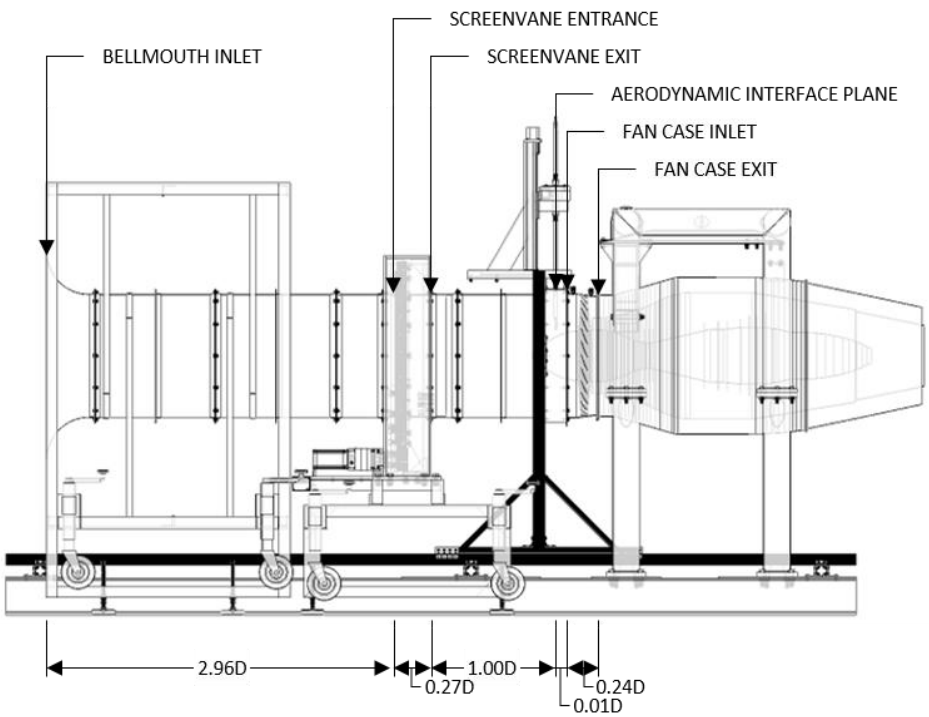

Figure 5.7: ScreenVane EXP Validation – Coupled Ground Test Setup

5.3.3 Experimental Test Matrix

At the onset of this investigation, decisions regarding the experimental ground test conditions directed many of the assumptions and conditions used in the computational analysis. For instance, setting the fan speed resulted in a known mass flow, while available facility hardware influenced the location of both the measurement planes and the distortion device, which in turn led to the selection of the AIP location and an upstream propagation distance. Most of these decisions were made using prior knowledge of the ground test facility hardware and capabilities built from extensive experience conducting previous research. That said, engineering judgement and critical thinking provided the guidance for previously unexplored areas of research.

A comprehensive experiment was desired that efficiently provided useful data in support of ScreenVane methodology verification and validation. To conduct a test that produced the most relevant data for modern turbofan engines, the maximum achievable inlet air mass flow rate was preferred. Due to the inlet duct hardware and the distortion generator, the turbofan engine used in this facility was known to reach maximum safe continuous operating conditions at 80% design maximum fan speed under distorted inlet conditions. This setting led to an air mass flow rate of approximately 50 lb_m/s and a fan blade tip Mach number of approximately 1.05. The mass flow condition was significant because it directed the boundary conditions for computational analysis. The fan blade tip Mach number was significant because it implied operation in the transonic regime.

Streamwise locations of measurement planes was dictated by the existing experimental hardware available at the turbofan engine ground test facility. Modular inlet duct sections provided some degree of flexibility in the experimental setup, but ultimately limitations were imposed by physical devices. The AIP was desired to be as close to the fan case as possible in order to quantify flow properties entering the engine with highest certainty. The AIP location relative to the fan case was governed by the dimensions of the five-hole three-dimensional flow probe measurement spool. The measurement spool bolted directly to the fan case and offset the measurement plane approximately 0.10 fan diameters upstream of the fan case bolt flange. Due to distortion device rotator dimensions and the desire to allow unintentional wake structures generated by the distortion devices to dissipate before reaching the measurement plane, an axial separation distance between the ScreenVane and AIP was set to one diameter. The isolation duct length used in the isolated experimental turbofan ground test setup was selected based on previous research. A conclusion of the previous research suggested that turbofan engine components (fan rotor and nose cone) influenced the fluid volume at a distance of up to one half of a diameter upstream. To ensure isolation and again rely on available experimental hardware, the standoff distance was extended to two full diameters.

In an attempt to balance fuel consumption and experimental expense with the most useful data, decisions regarding number of data collections and number of test replications were made. A priority was placed on spatial resolution of data rather than repetitive tests. This was only possible by leveraging previous research that focused on uncertainty quantification and reduction through the use of multiple test replications [62,63,79]. Citing this previous work, Table 5.3 summarizes the approximate measurement uncertainties associated with the significant measured parameters.

Table 5.3: ScreenVane EXP Validation – Approximate Measurement Uncertainties

Total Pressure	±0.03 psia
Total Temperature	±2.00 °F
Swirl Angle	±1.50°
Corrected Fan Speed	±0.25%
Corrected Inlet Air Mass Flow Rate	±2.00 lb_m/s

For the isolated test setup, the probe travel was unlimited by turbofan engine geometry and allowed to plunge to the duct centerline. Due to the radial and circumferential motion of the probe and distortion device, a uniformly spaced grid was not appropriate, as inner radii (near centerline) would be unnecessarily highly sampled while outer radii (near wall) would be sparsely sampled. Therefore, engineering judgement was used to distribute data samples to a relatively evenly

spaced, non-uniform grid. Radially, measurements were taken at 0.25 – 1.00 inch intervals; circumferentially measurements were taken at 5.00 – 45.00 degree increments. Figure 5.8 illustrates the five-hole three-dimensional flow probe measurement locations at the isolated AIP. As shown, the measurement locations at the innermost radii were located on a sparse circumferential interval. Moving outward from centerline, additional circumferential intervals were incorporated to obtain a nearly evenly spaced arrangement. The smallest circumferential intervals were utilized at the wall where arc length is greatest and significant distortion elements exist. Due to the boundary layer gradients, dense radial increments were used within small distances along the outer wall.

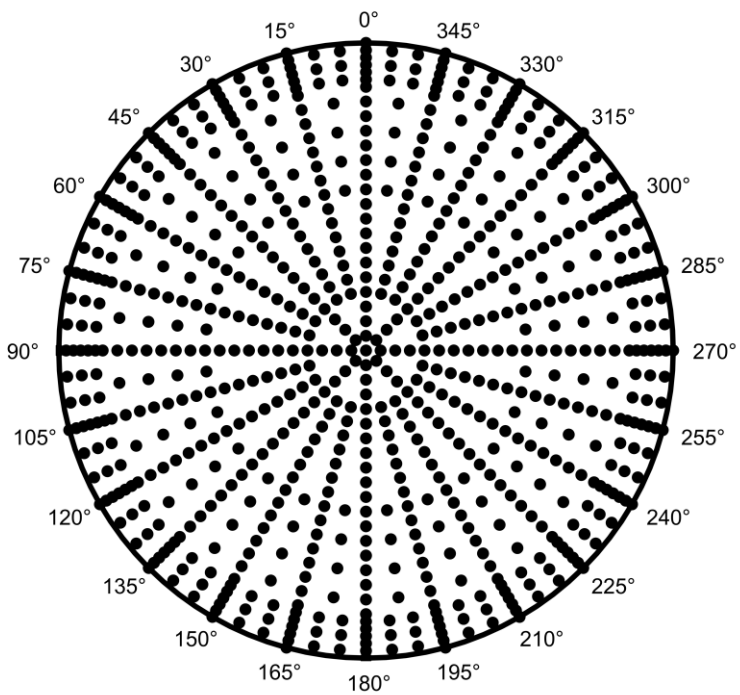

Figure 5.8: ScreenVane EXP Validation – Isolated AIP Measurement Locations

For the coupled test setup, the probe was limited by turbofan engine geometry and constrained to plunge only to the nose cone surface. A technique very similar to the isolated AIP measurement location specification was used to define the coupled AIP measurement locations. Due to the radial and circumferential motion of the probe and distortion device, a uniformly spaced grid was not appropriate, as inner radii (near nose cone) would be unnecessarily highly sampled while outer radii (near wall) would be sparsely sampled. Therefore, engineering judgement was used to distribute data samples to a relatively evenly spaced, non-uniform grid. Radially, measurements were taken at 0.25 – 0.50 inch intervals; circumferentially measurements were taken at 5.00 – 15.00 degree increments. Figure 5.9 illustrates the five-hole three-dimensional flow probe measurement locations at the coupled AIP. As shown, the measurement locations at the innermost radii were located on a sparse circumferential interval. Moving outward from centerline, additional circumferential intervals were incorporated to obtain a nearly evenly spaced arrangement. The smallest circumferential intervals were utilized at the wall where arc length is

greatest and significant distortion elements exist. Due to the boundary layer gradients, dense radial increments were used within small distances along the nose cone surface and the outer wall.

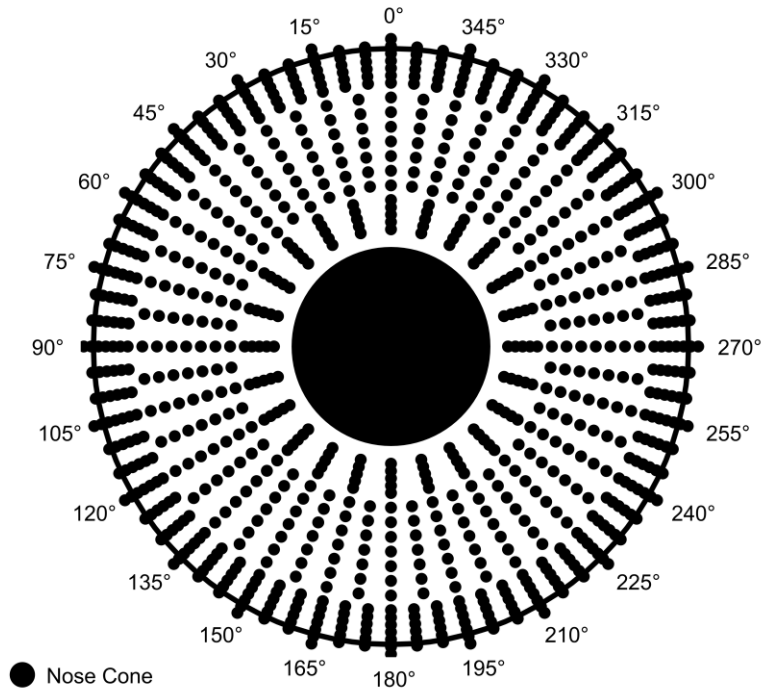

Figure 5.9: ScreenVane EXP Validation – Coupled AIP Measurement Locations

Again using previous experience, data collection and settling times were defined. Experimental data was collected for five seconds at each measurement location to obtain a steady state time-averaged value. After each movement but before each collection, a three second settling period was set to allow the flow to reach steady state conditions. These settings have been proven to provide ample time for an accurate measurement without unnecessary excess.

The following tables summarize the complete turbofan engine ground test matrix used to validate the ScreenVane distortion device.

Table 5.4: ScreenVane EXP Validation – Engine Settings and Experimental Parameters

Corrected Fan Speed (% Max. of 16000 RPM)	80% Max. (Approx. 12800 RPM)
Fan Blade Tip Speed	1200 ft/s (Approx. 1.05 Mach)
Corrected Inlet Mass Flow Rate	50 lb_m/s (Nominal)
Fan Pressure Ratio	1.35 (Nominal)
Data Sampling Time	5 seconds
Data Settling Time	3 seconds

Table 5.5: ScreenVane EXP Validation – Isolated AIP Measurement Locations

Radial Location	Circumferential Location
r/r_w	θ
0.00	0-315° by 45°
0.05	0-315° by 45°
0.10	0-315° by 45°
0.14	0-315° by 45°
0.19	0-345° by 15°
0.24	0-345° by 15°
0.29	0-345° by 15°
0.33	0-345° by 15°
0.38	0-345° by 15°
0.43	0-345° by 15°
0.48	0-345° by 15°
0.52	0-352.5° by 7.5°
0.57	0-345° by 15°
0.62	0-352.5° by 7.5°
0.67	0-345° by 15°
0.71	0-352.5° by 7.5°
0.76	0-345° by 15°
0.81	0-352.5° by 7.5°
0.86	0-345° by 15°
0.88	0-355° by 5°
0.90	0-345° by 15°
0.93	0-355° by 5°
0.95	0-345° by 15°
0.98	0-355° by 5°
1.00	0-345° by 15°

Table 5.6: ScreenVane EXP Validation – Coupled AIP Measurement Locations

Radial Location	Circumferential Location
r/r_w	θ
0.38	0-345° by 15°
0.40	0-345° by 15°
0.43	0-345° by 15°
0.45	0-345° by 15°
0.48	0-345° by 15°
0.52	0-352.5° by 7.5°
0.57	0-352.5° by 7.5°
0.62	0-352.5° by 7.5°
0.67	0-352.5° by 7.5°
0.71	0-352.5° by 7.5°
0.76	0-352.5° by 7.5°
0.81	0-352.5° by 7.5°
0.86	0-355° by 5°
0.88	0-355° by 5°
0.90	0-355° by 5°
0.93	0-355° by 5°
0.95	0-355° by 5°
0.98	0-355° by 5°
1.00	0-345° by 15°

To determine the deviations in flow properties from nominal uniform inlet flow conditions, the ScreenVane was removed from the rotator and replaced by a uniform wire mesh screen. This screen was made from wire mesh identical to that used as the backer screen material for the total pressure distortion Screen. The use of this screen assisted in controlling inlet air mass flow rates for non-distorted baseline tests. Because the flow was assumed uniform in the non-distorted test, five-hole three-dimensional flow probe measurements were taken at the top-dead-center circumferential location at all plunge depths matching the distorted test. Additionally, a range of fan speeds was tested to bracket the distorted test flow conditions. The absence of the ScreenVane blockage allowed elevated inlet air mass flow rates to enter the turbofan engine. By incrementally varying the fan speed, results were compared at a matching fan speed and matching inlet air mass flow rate.

5.3.4 Experimental Procedure

With the engine setup complete, a typical ground test began with energizing all electronic equipment and calibrating the pressure scanners. A six-point, full-scale calibration of the ±2.5 psid and ±5.0 psid pressure scanners was conducted using a regulated pressure supply manifold and a handheld digital manometer (Dwyer 477A-3) as a reference pressure indicator. Pressure was incrementally supplied to the reference port of the differential pressure transduces representing sub-atmospheric pressures in the inlet duct upstream of the fan. The voltage output was recorded with the data acquisition system and individual calibration curves were generated for each pressure transducer. Following calibration, the reference pressure port was vented in preparation for testing.

A custom National Instruments LabView software package was then initialized on the data acquisition computer. This software allowed the user to set data acquisition sample rates and times for the various instruments, to define positions for both the ScreenVane rotator and radial traverse, and to monitor instrumentation signals throughout the test. All experimental values were set prior to engine start and automatically called upon during data collection.

The turbofan engine was then started and allowed to idle for several minutes to warm components to safe operating temperatures. After warming, the throttle position was set to an uncorrected fan speed calculated from the local atmospheric temperature and again allowed to stabilize. Once stable, the data acquisition software commanded the radial traverse to plunge the five-hole three-dimensional flow probe to the desired depth. A brief settling period after moving allowed the measurements to reach steady state before all data acquisition channels were simultaneously recorded. The probe then moved to the subsequent radial location and the data collection process was repeated. After collecting a radial survey, the rotator engaged and rotated the ScreenVane to the next desired circumferential location and the radial plunge process with data collection was repeated. Through the coordinated process of incrementally plunging the five-hole three-dimensional flow probe and incrementally rotating the ScreenVane distortion device, the entire test matrix was measured. A flowchart summarizing the probe movement, device rotation, and data collection sequencing can be found in Figure 5.10.

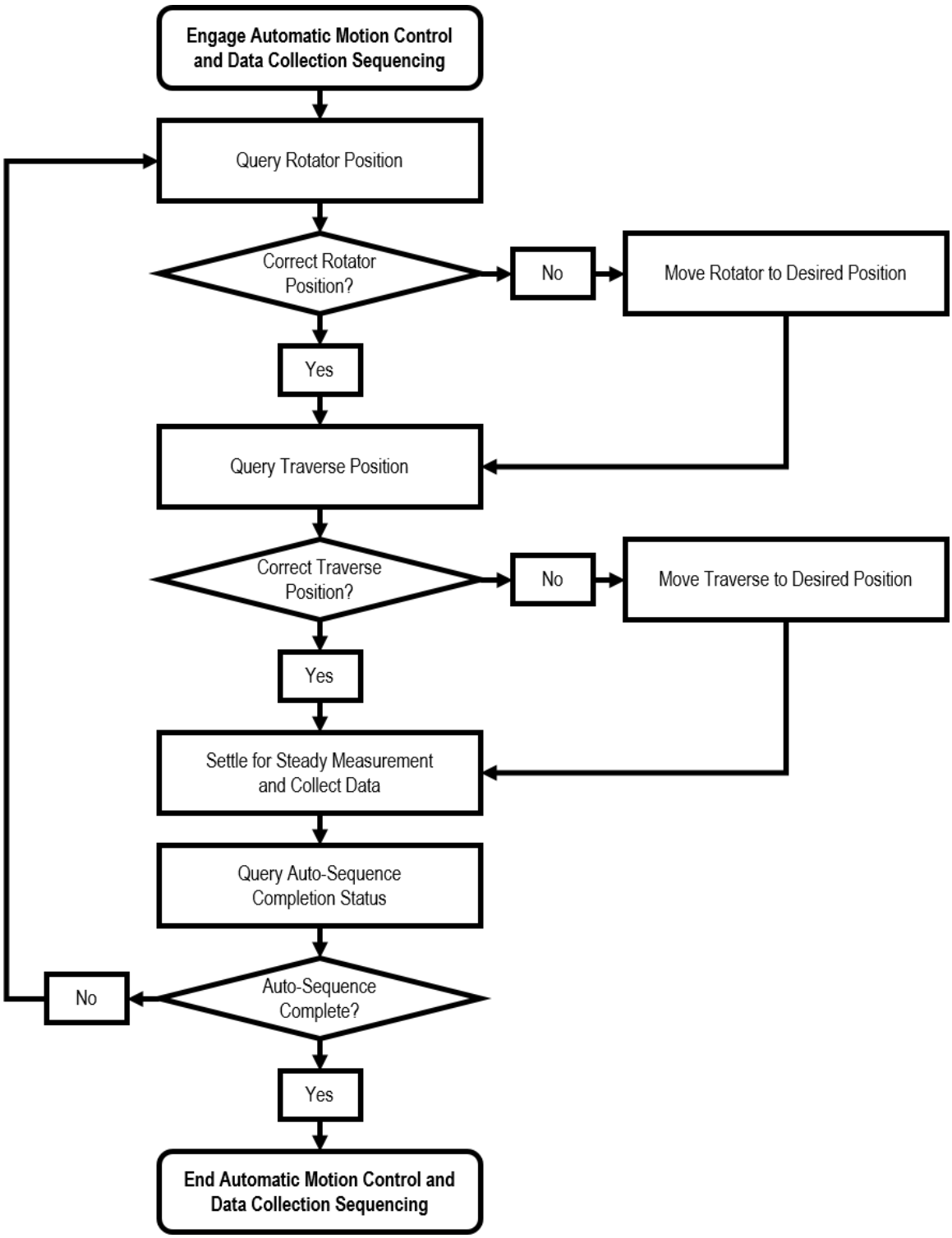

Figure 5.10: ScreenVane EXP Validation – Motion Control and Data Collection Process Map

Upon completion of the desired test matrix, the turbofan engine was shutdown, the experimental setup was inspected for any inconsistencies from startup conditions, and the pressure transducers were recalibrated using an identical process as previously defined.

5.4 The ScreenVane Experimental Validation Data Analysis

5.4.1 Instrument Data Reduction

Five distinct instruments were utilized to acquire experimental data. Tachometer/generators measured shaft speeds for both the fan and core spools, a rotary flow meter measured fuel flow rate, a thermopile measured the inter-turbine-temperature system, pressure transducers measured the bellmouth wall static pressures and the five-hole three-dimensional flow probe pressures, and a thermocouple measured the five-hole three-dimensional flow probe total temperature. Each of these instruments required a unique data reduction process to extract useful information regarding engine parameters and flow conditions within the turbofan engine ground test facility during experimental distortion testing.

In many measured values, correction factors were required to maintain congruity of data over the course of many days of data collection. These factors relate to sea-level standard atmospheric conditions and are defined in Equation 5.1 and Equation 5.2 for pressure correction and temperature correction, respectively.

$$\delta = \frac{P_{atm}}{P_{std}} \; where \; P_{std} = 14.696 \; psia \tag{5.1}$$

$$\theta = \frac{T_{atm}}{T_{std}} \; where \; T_{std} = 518.67 \; °R \tag{5.2}$$

The tachometer/generators used by the turbofan speed monitoring system output an alternating current at a frequency corresponding to the rotational velocity of the fan and core shafts. The tachometer/generators contain internal gearing to limit the speed of the instruments. This gear ratio was applied to the measured output frequency to obtain uncorrected speed data. Because atmospheric conditions change, the time-averaged uncorrected speed was corrected to standard atmospheric conditions according to Equation 5.3. This corrected speed served as a means of reporting identical experimental conditions among subsequent tests regardless of local atmospheric conditions.

$$N_{corrected} = \frac{N_{measured}}{\sqrt{\theta}} \tag{5.3}$$

Similar to the tachometer/generators, the fuel flow meter outputs a square wave at a frequency corresponding to the rotational velocity of a fuel flow driven rotor. A known gauge factor converted this frequency measurement to uncorrected fuel flow rate. Because atmospheric conditions change, the time-averaged uncorrected fuel flow rate was corrected to standard atmospheric conditions according to Equation 5.4. This corrected fuel flow served as a means of reporting identical experimental conditions among subsequent tests regardless of local atmospheric conditions.

$$\dot{m}_{f_{corrected}} = \frac{\dot{m}_{f_{measured}}}{\delta\sqrt{\theta}} \tag{5.4}$$

The pressure measurement system consists of individual pressure transducers arranged in pressure scanner housing. Each pressure transducer outputs a voltage linearly proportional to the applied pressure. Prior to and following each experimental test, the pressure transducers were calibrated to a specific range by supplying several known reference pressures and recording the associated output voltages. Linear fit models relating pressure to voltage were calculated for each transducer (Equation 5.5).

$$P_{measured} = mV_{measured} + b \tag{5.5}$$

The recorded voltages were processed using the linear fit models and time-averaged, resulting in a single steady state pressure data point. Because atmospheric conditions change, the time-averaged measured pressure was corrected to standard atmospheric conditions according to Equation 5.6. This corrected pressure served as a means of reporting identical experimental conditions among subsequent tests regardless of local atmospheric conditions.

$$P_{corrected} = \frac{P_{measured}}{\delta} \tag{5.6}$$

Temperature data from the thermopile used in the inter-turbine-temperature monitoring system and the thermocouple embedded in the five-hole three-dimensional flow probe were time averaged and corrected to standard atmospheric conditions (Equation 5.7). This corrected temperature served as a means of reporting identical experimental conditions among subsequent tests regardless of local atmospheric conditions.

$$T_{corrected} = \frac{T_{measured}}{\theta} \tag{5.7}$$

5.4.2 Bellmouth Inlet Mass Flow Rate

The time-averaged value of the bellmouth static pressure measurements along with the total pressure within the inlet (assuming no losses, the total pressure in the inlet is equal to the atmospheric pressure) were used to calculate the Mach number at the defined bellmouth inlet plane (Equation 5.8). This Mach number was used to calculate an ideal mass flow rate (Equation 5.9) [112] from which the Reynolds number of the flow can be calculated (Equation 5.10).

$$M = \sqrt{\frac{2}{\gamma - 1}\left(\left(\frac{P_0}{P}\right)^{\frac{\gamma-1}{\gamma}} - 1\right)} \tag{5.8}$$

$$\dot{m}_{a_{ideal}} = \frac{P_0\sqrt{\gamma}}{\sqrt{RT_0}}\left(\frac{2}{\gamma+1}\right)^{\frac{\gamma+1}{2(\gamma-1)}} \tag{5.9}$$

$$Re = \frac{4\dot{m}_{a_{ideal}}}{\pi\mu D} \tag{5.10}$$

The Reynolds number dependent discharge coefficient of the actual bellmouth inlet was interpolated from calibration tables using the ideal Reynolds number input (Equation 5.11). The discharge coefficient was then used as a correction factor to calculate the actual inlet mass flow rate from the ideal inlet mass flow rate (Equation 5.12). Because corrected pressures and temperatures were used in the initial calculations of Mach number and ideal mass flow rate, the resulting air mass flow rate from Equation 5.12 was already corrected to standard atmospheric conditions and no further correction was necessary.

$$C_d = f(Re) \tag{5.11}$$

$$\dot{m}_{a_{corrected}} = C_d\dot{m}_{a_{ideal}} \tag{5.12}$$

5.4.3 Five-Hole Three-Dimensional Flow Probe Measurements

Planar results profiles were obtained using a traversing five-hole three-dimensional flow probe situated at various axial locations within the inlet duct of the turbofan engine research platform. The resulting data sets include radial flow angle, tangential flow angle, total pressure, static pressure, Mach number, total temperature, static temperature, and velocity components. Each parameter required a unique data processing technique to extract useful data from the raw pressures and temperatures measured by the instrument.

Processing radial and tangential flow angles and total and static pressures involved normalizing measured probe pressures to form pressure coefficients that were then correlated to calibration curves [111]. The probe calibration was conducted in-house using a two-axis rotary table. By setting the radial and tangential angle of the probe within the fixture, pressures were measured at each of the five sensing locations on the probe. The measured pressures where then normalized using Equations 5.13 – 5.17, and recorded as functions of radial and tangential flow angle in Figure 5.11.

$$\bar{P} = \frac{P_2 + P_3 + P_4 + P_5}{4} \tag{5.13}$$

$$Cp_{\alpha_r}(\alpha_r, \alpha_\theta) = \frac{P_4 - P_5}{P_1 - \bar{P}} \tag{5.14}$$

$$Cp_{\alpha_\theta}(\alpha_r, \alpha_\theta) = \frac{P_2 - P_3}{P_1 - \bar{P}} \tag{5.15}$$

$$Cp_{P_0}(\alpha_r, \alpha_\theta) = \frac{P_1 - P_0}{P_1 - \bar{P}} \tag{5.16}$$

$$Cp_P(\alpha_r, \alpha_\theta) = \frac{\bar{P} - P}{P_1 - \bar{P}} \tag{5.17}$$

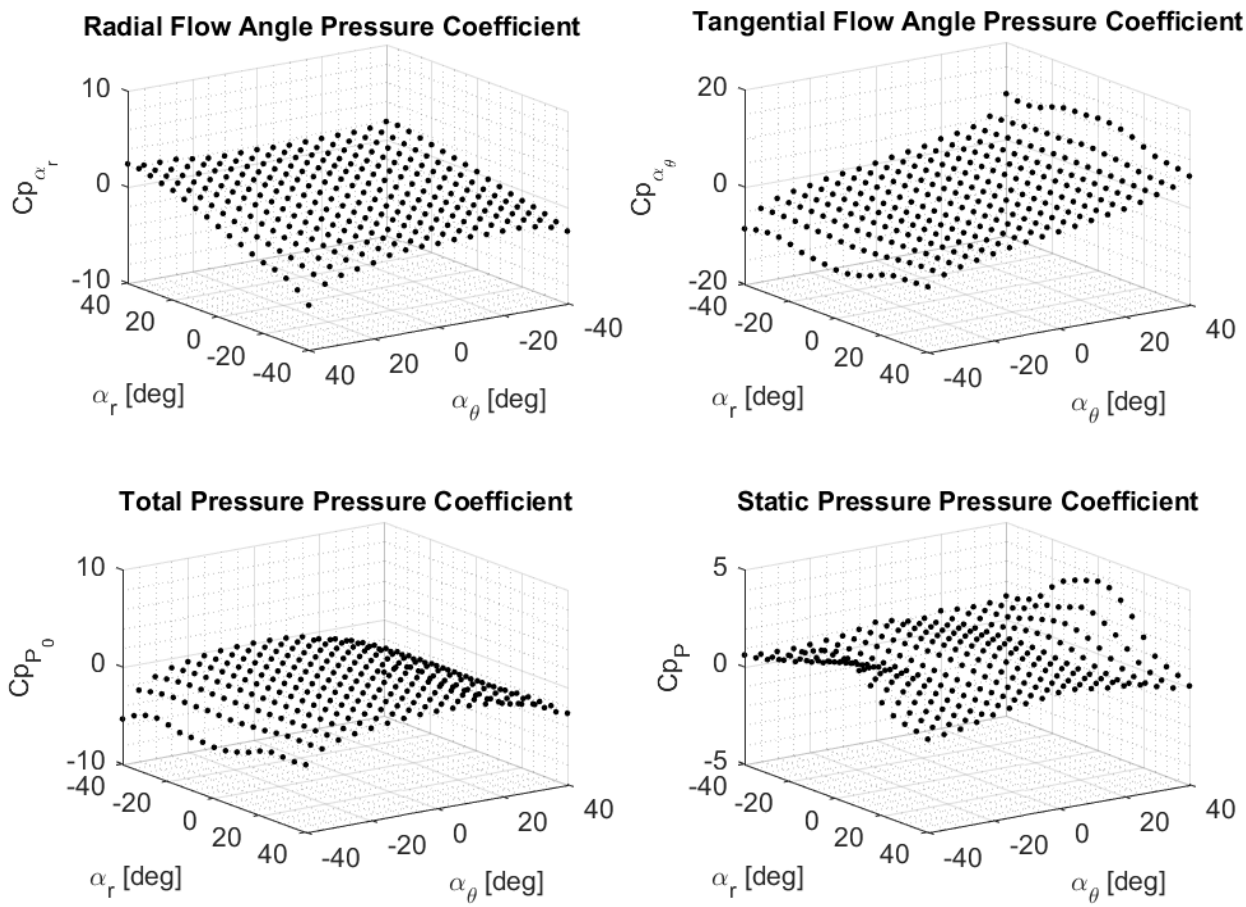

Figure 5.11: ScreenVane EXP Validation – Five-Hole Probe Calibration

During experimental turbofan engine ground test data processing, the radial and tangential flow angles are the first terms extracted. The pressure coefficients relating to the flow angles (Equation 5.14 and Equation 5.15) were calculated and interpolated to the known calibration data to obtain radial and tangential flow angle measurements.

With the flow angles known, the pressure coefficients relating to total pressure and static pressure were interpolated from specific calibration data as functions of radial and tangential flow angle. These pressure coefficients were then used to calculate the total pressure and static pressure using Equation 5.18 and Equation 5.19, respectively.

$$P_0 = P_1 - Cp_{P0}(P_1 - \bar{P}) \tag{5.18}$$

$$P = \bar{P} - Cp_P(P_1 - \bar{P}) \tag{5.19}$$

Utilizing the isentropic flow assumptions, the Mach number was calculated from the relationship between the total and static pressures (Equation 5.20).

$$M = \sqrt{\frac{2}{\gamma - 1}\left[\left(\frac{P_0}{P}\right)^{\frac{\gamma-1}{\gamma}} - 1\right]} \tag{5.20}$$

The total temperature was directly measured from the thermocouple embedded in the five-hole three-dimensional flow probe. Again utilizing the isentropic flow assumptions, the static temperature was calculated from the relationship between the total temperature and Mach number (Equation 5.21).

$$T = \frac{T_0}{1 + \frac{\gamma - 1}{2}M^2} \tag{5.21}$$

Finally, with the radial flow angles, tangential flow angles, Mach number, and static temperature known, the velocity profile was computed. First, the velocity magnitude was calculated from the Mach number and local speed of sound according to Equation 5.22 and Equation 5.23.

$$a = \sqrt{\gamma RT} \tag{5.22}$$

$$C_{r\theta z} = Ma \tag{5.23}$$

Next, the velocity magnitude was decomposed into the three-dimensional velocity components using the measured flow angles. Figure 5.12 illustrates the coordinate vector system which relates the velocity components and velocity magnitude.

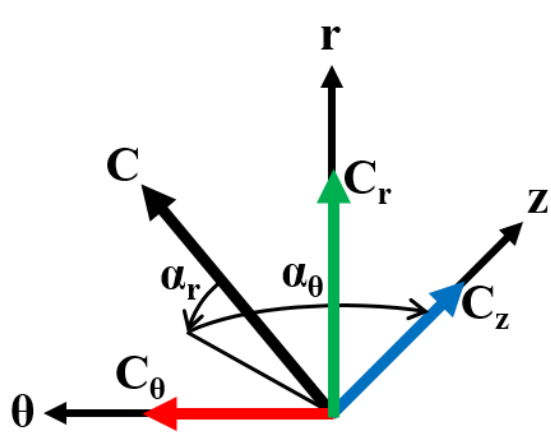

Figure 5.12: ScreenVane EXP Validation – Three-Dimension Velocity Components

From the figure, the relationship of radial flow angle, tangential flow angle, and velocity magnitude was defined. Due to the compound flow angles found within the flow field, a coordinate transformation (Equations 5.24-5.26) was derived to calculate the radial, tangential, and axial velocity components.

$$C_r = C_{r\theta z} \sin(\alpha_r) \tag{5.24}$$

$$C_\theta = C_{r\theta z} \cos(\alpha_r) \sin(\alpha_\theta) \tag{5.25}$$

$$C_z = C_{r\theta z} \cos(\alpha_r) \cos(\alpha_\theta) \tag{5.26}$$

5.5 The ScreenVane Experimental Validation Results

5.5.1 Total Pressure Distortion Profile

Total pressure distortion profiles were measured at the AIP and are presented in Figure 5.13. The circular cross sections (left) illustrate the full-field planer total pressure recovery as normalized by the maximum in-plane total pressure. From these profiles, the total pressure distortion remained highly discretized downstream of initiation. This was attributed to the discrete regions of distortion screens used to generate the total pressure distortion. In the lower semi-circular region, the two lobes of low total pressure recovery merged as desired to form a once-per-revolution total pressure distortion.

The circumferential trends (right) unwrap the distortion profile beginning at top-dead-center (0°), moving counterclockwise through bottom-dead-center (180°), and returning counterclockwise to top-dead-center (360°). The colors displayed here correspond to normalized radius. The total pressure distortion was concentrated near the outer wall, where recovery values experienced the largest fluctuations. In the upper semi-circular region, the total pressure was nearly fully recovered with values greater than 97% for all radii. In the lower semi-circular region, recovery values descended to a minimum of approximately 92% at the outermost radii. All results are presented forward-looking-aft.

Comparing the total pressure distortion profiles from the ScreenVane experimental results with the ScreenVane computational results provided useful model validation; while comparing ScreenVane experimental results with the S-duct computational results provided useful method validation. Figure 5.14 and Figure 5.15 show the comparison between the ScreenVane computational and experimental total pressure distortion profiles at the AIP and the comparison between S-duct computational and ScreenVane experimental total pressure distortion profiles at the AIP, respectively. For both results, the comparison data was calculated according to Equation 5.27.

$$Comparison = |Experimental| - |Computational| \tag{5.27}$$

Qualitatively, the ScreenVane computational model predicted the experimental conditions with great success. The overall shapes and extents were well represented with the majority of error found in intensity levels. The experimental device was found to produce a slightly stronger overall distortion; however, a large portion of the profile agreed within ±1% recovery and nearly all of the profile agreed within ±2% percent recovery. Quantitatively, the full-field total pressure recovery profile matched within 1% RMSD.

Upon inspection of the comparison between the original S-duct computational results and the ScreenVane experimental results, the ScreenVane over produced total pressure losses in the lower semi-circular region of the AIP. While approximately 50% of the profile agreed within ±1% recovery, a non-negligible area of the profile differed by greater than ±2% recovery. Quantitatively, the full-field total pressure recovery profile RMSD echoed the inspected disagreement with values approaching 1.5%.

The errors found in this comparison were determined to be associated with the discretized wire mesh total pressure distortion Screen. The largest errors were often found in areas of mild gradients where the discrete wire meshes produced near step changes in total pressure recovery profile.

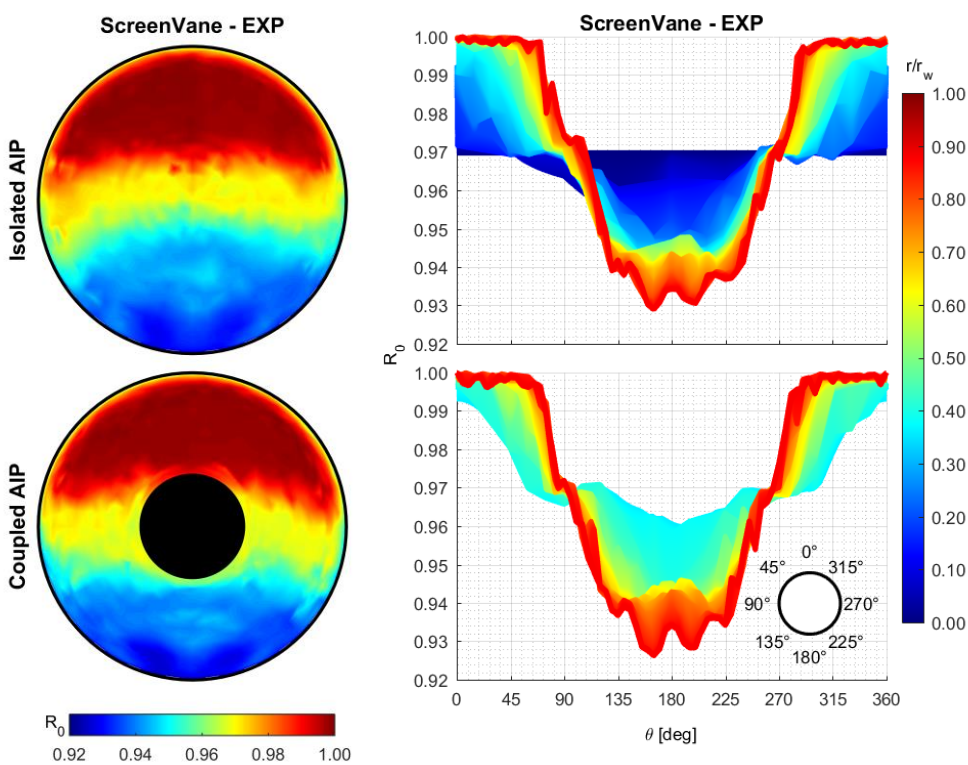

Figure 5.13: ScreenVane EXP Validation – AIP Total Pressure Recovery Profiles and Trends

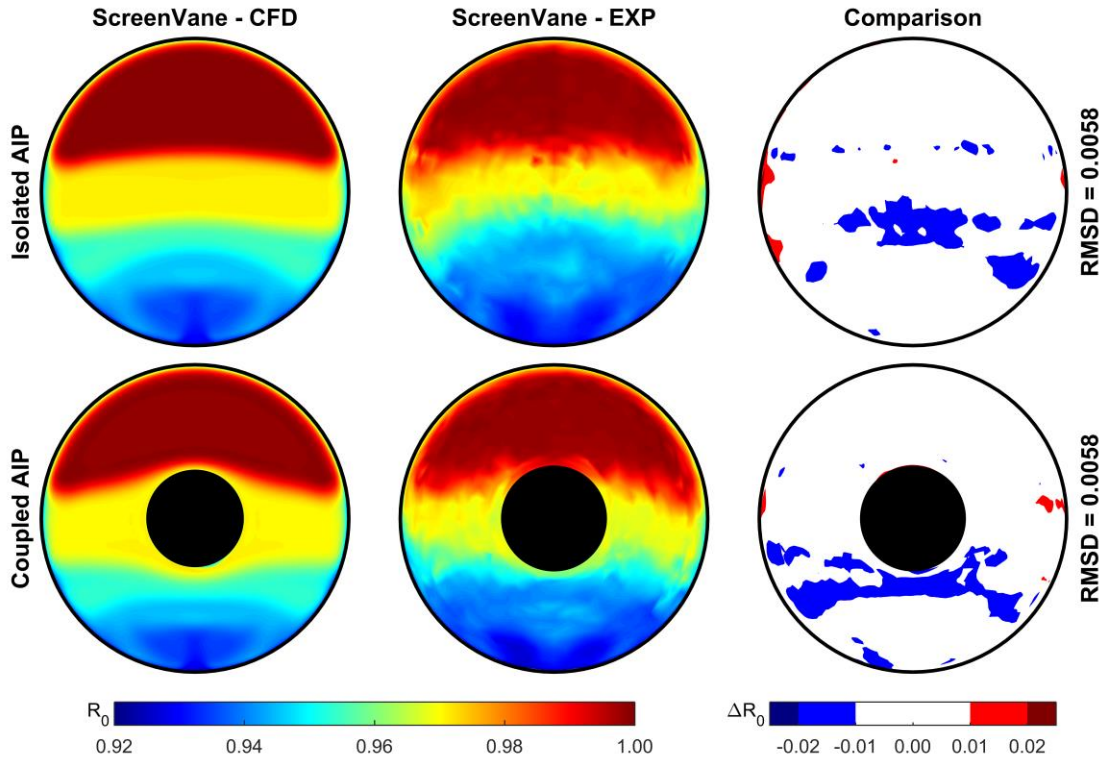

Figure 5.14: ScreenVane Model Validation – AIP Total Pressure Recovery Comparison

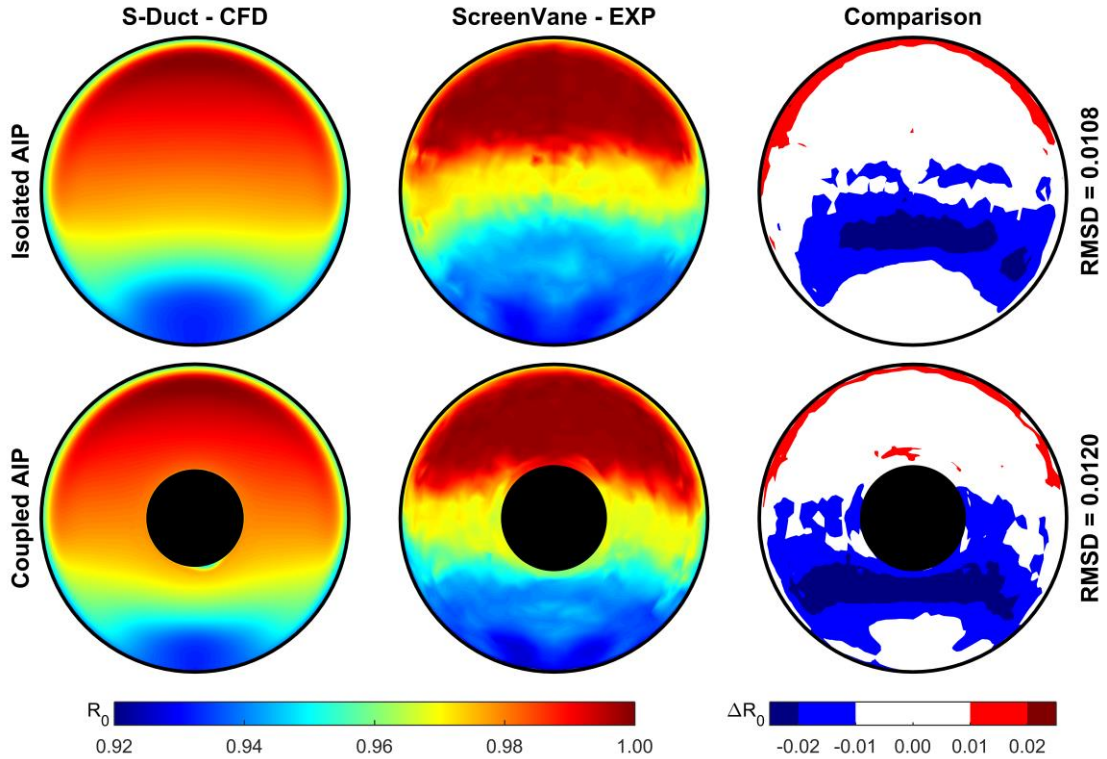

Figure 5.15: ScreenVane Method Validation – AIP Total Pressure Recovery Comparison

5.5.2 Swirl Distortion Profile

Swirl distortion profiles were measured at the AIP and are presented in Figure 5.16. The circular cross sections (left) illustrate the full-field planer swirl angle. From these profiles, the swirl angle results showed paired swirl in the lower semi-circular region. The incorporation of turbofan engine geometry caused a slight attenuation in the maximum measured swirl angle. Outside the region of influence of the paired swirl, the turbofan components and associated cross-sectional area reduction produced significant mass flow redistribution. Flow angles indicated an overall downward flow direction from the upper semi-circular region to the lower semi-circular region.

The circumferential trends (right) unwrap the distortion profile beginning at top-dead-center (0°), moving counterclockwise through bottom-dead-center (180°), and returning counterclockwise to top-dead-center (360°). The colors displayed here correspond to normalized radius. Swirl distortion was concentrated in the outermost radii. The twin-vortices of the paired swirl feature were clearly defined as a large gradient near bottom-dead-center where flow angle fluctuates between ±12°. In both sets of experimental results, the measured swirl angles were well organized, clearly apparent, and remarkably symmetric. All results are presented forward-looking-aft.

Comparing the swirl distortion profiles from the ScreenVane experimental results with the ScreenVane computational results provided useful model validation; while comparing ScreenVane experimental results with the S-duct computational results provided useful method validation. Figure 5.17 and Figure 5.18 show the comparison between the ScreenVane computational and experimental swirl distortion profiles at the AIP and the comparison between S-duct computational and ScreenVane experimental swirl distortion profiles at the AIP, respectively. For both results, the comparison data was calculated according to Equation 5.27.

Qualitatively, the ScreenVane experimental results support the computational model within ±1.5° of predicted swirl angle and small areas exceeding that value. In the cases including nose cone geometry, the downward fluid motion was exacerbated in the experimental results, likely due to the slightly over produced total pressure distortion discussed in the previous section leading to increased fluid redistribution from areas of relatively high pressure waldo to areas of relatively low pressure. Quantifying the error resulted in full-field profile RMSD values of approximately 1.75° in the isolated test and just over 2.50° in the coupled test.

Upon inspection of the comparison between the original S-duct computational results and the ScreenVane experimental results, the ScreenVane performed exceptionally as a ground test device. Qualitatively, the distortion profile shapes and extents matched nearly perfectly with the majority of error involving slightly elevated distortion intensity. Nearly all of the experimental profile matched the original S-duct distortions within ±1.5° with significant errors occurring only at the outer wall (where boundary layer profiles were not specifically designed to match) and in areas of high gradients (where small errors in feature location result in amplified intensity error). Quantifying the error resulted in full-field profile RMSD values of approximately 2.50° in the isolated test and just under 3.00° in the coupled test. These errors are likely increased by mismatched boundary layer flows between the two different geometries.

The errors found in this comparison were determined to relate to a mismatch in the boundary layer representation at the wall and small location differences in significantly distorted regions. Transitioning from the computational realm (smooth, non-slip wall boundary conditions with perfect geometry) to the experimental realm (wall roughness and imperfect geometry) makes perfect replication of boundary layer flows extremely difficult. Additionally, the experimental devices and setup compound location errors of significant distortion features where high gradients exist. This means that small location errors can produce large errors in measured distortion parameters.

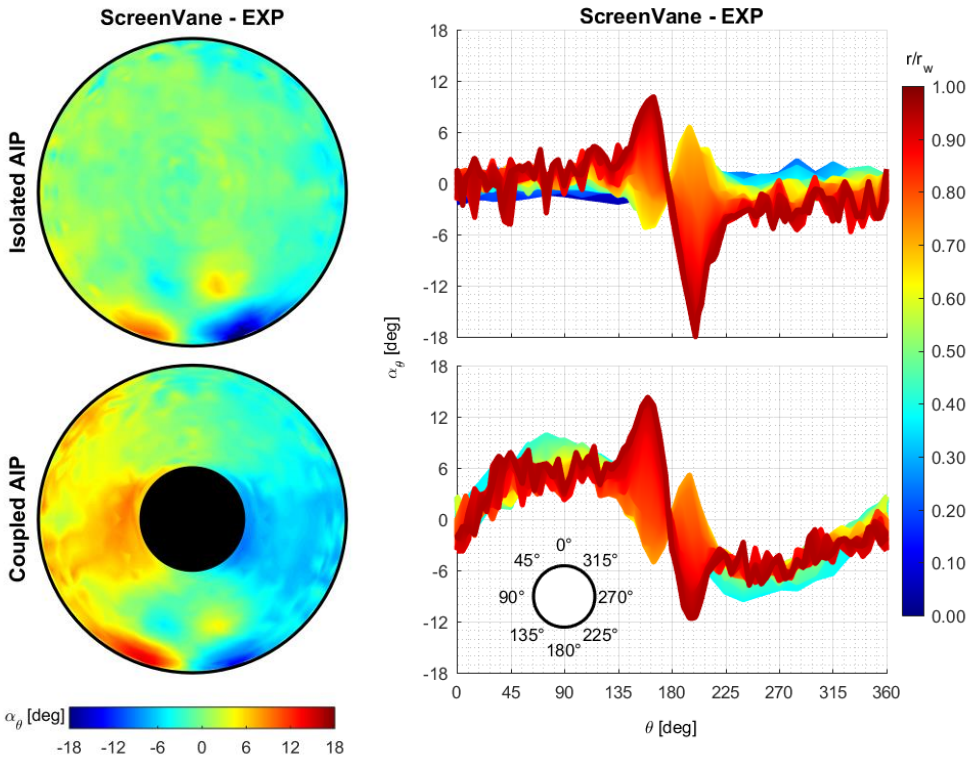

Figure 5.16: ScreenVane EXP Validation – AIP Swirl Angle Profiles and Trends

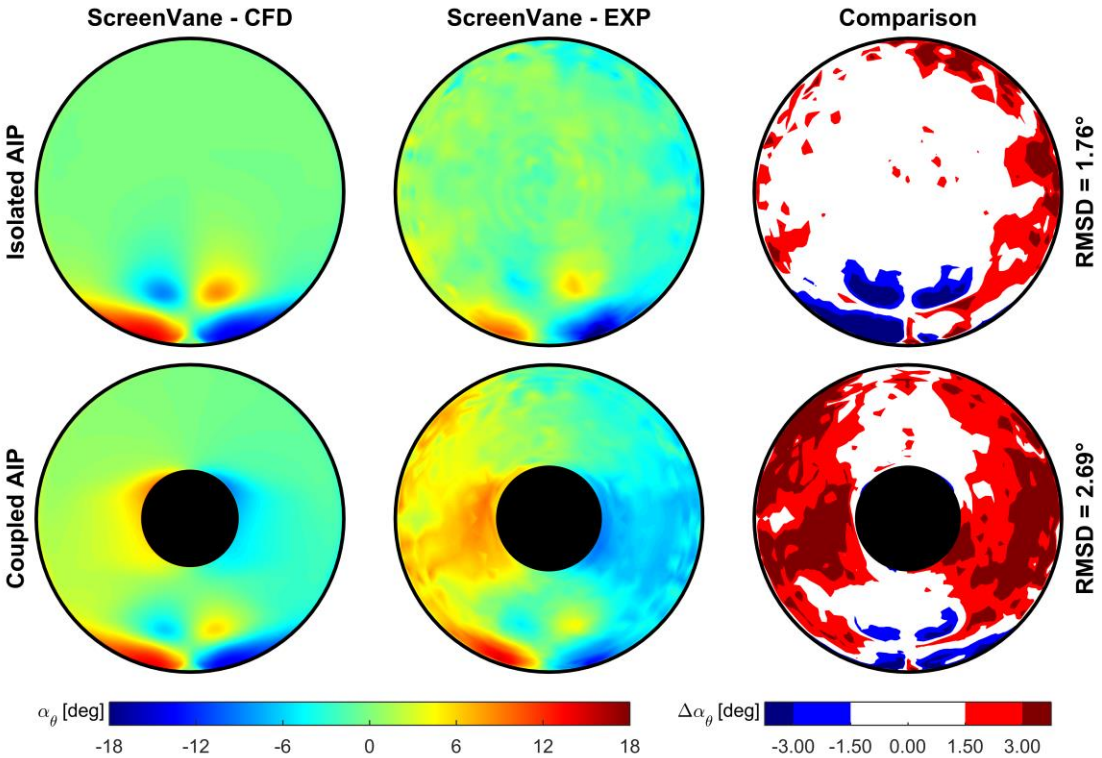

Figure 5.17: ScreenVane Model Validation – AIP Swirl Angle Comparison

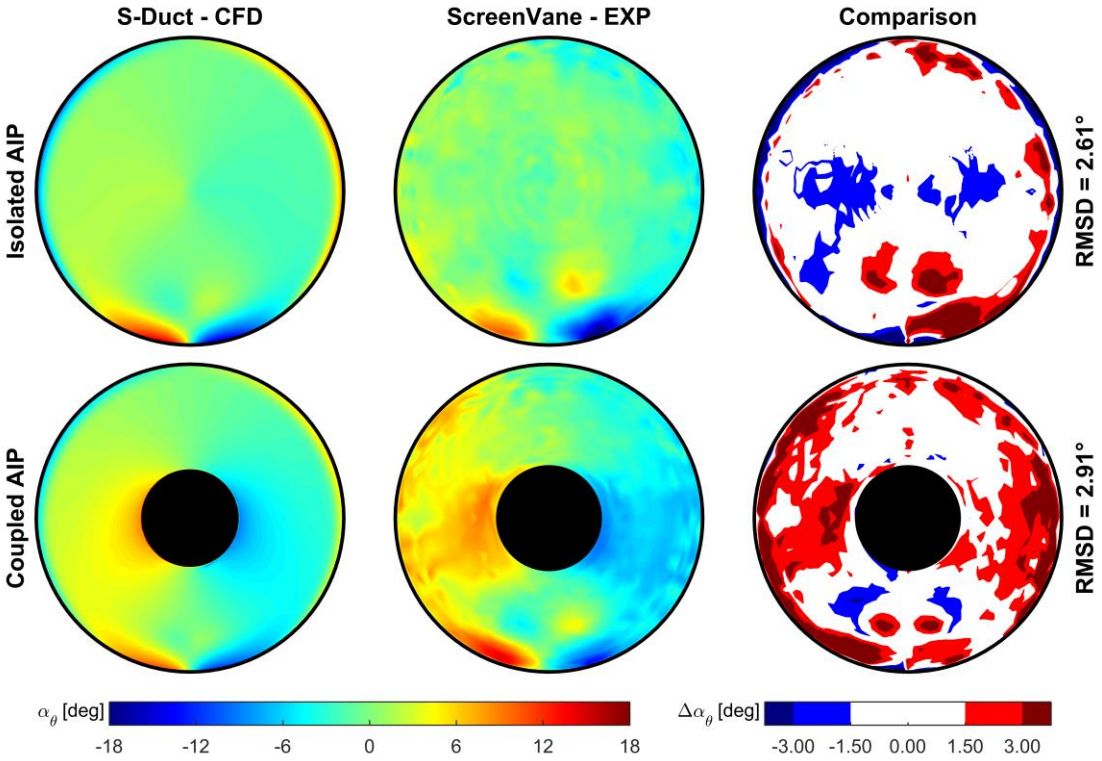

Figure 5.18: ScreenVane Method Validation – AIP Swirl Angle Comparison

5.5.3 S-16 Distortion Descriptors

Comparison of the S-16 Distortion Descriptors (Figure 5.19) confirmed the over production of distortion from the experimental ScreenVane device. The experimental total pressure circumferential distortion intensity followed an identical trend to both computational analyses with elevated intensity levels. The experimental total pressure radial distortion intensity agreed nearly perfectly with both computational analyses. The isolated test arrangement produced swirl intensity with near perfect agreement; however, the incorporation of turbofan engine hardware produced slightly elevated swirl intensity levels.

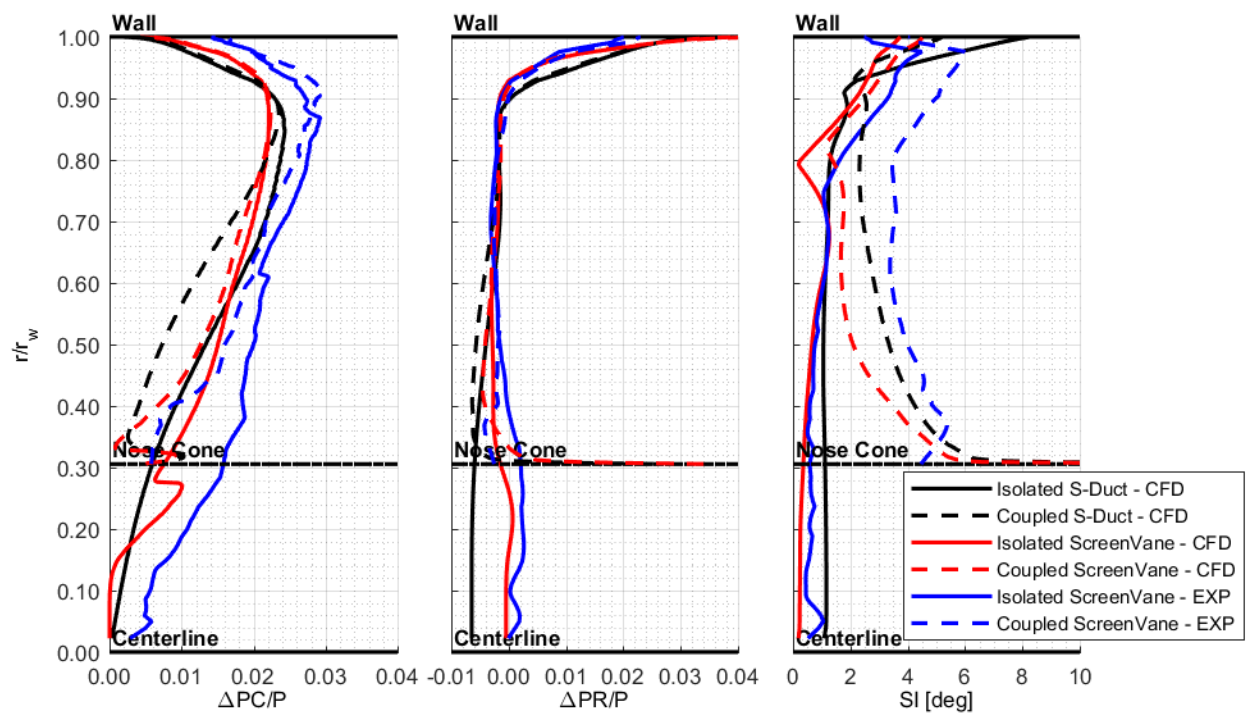

Figure 5.19: ScreenVane EXP Validation – AIP S-16 Distortion Intensity Trend Comparison

5.6 Summary

Turbofan engine ground tests were conducted to verify the ScreenVane design methodology and to validate computational models. Experimental hardware was manufactured and installed in the inlet duct of a turbofan engine ground test platform. A rigorous and thorough test setup and procedure was designed and followed to examine the capability of the ScreenVane to produce a combined total pressure and swirl distortion profile matching predicted flow conditions exiting an S-duct turbofan engine inlet.

The ScreenVane experimental setups matched computational analysis simulations in configuration, scale, and initial flow conditions. Fan speed was set to 80% to allow sufficient turbomachinery stability margin and maintain safe continuous operating conditions while

ingesting an inlet air mass flow rate of approximately 50 lb_m/s. Furthermore, identical AIP locations were used in isolated and coupled configurations to provide congruent data sets for comparison of ScreenVane experimental results to both predicted ScreenVane computational results and to S-duct computational results.

ScreenVane generated distortion profiles were measured at the AIP for analysis and comparison to computational predictions. Experimental results were first compared to ScreenVane computational results. In both the isolated and coupled setups, the experimental and computational total pressure distortion results agreed exceptionally well with nearly the entire total pressure recovery profile matching within one percent. Swirl angle agreement errors between the experimental and computational results were slightly larger, with the majority of the flow profile matching within one and one half degrees for the isolated setup and two and one half degrees in the coupled setup. This error was found to be strongly dependent on the relatively small scale distortion features and large gradients within the distortion features which locally amplified discrepancies.

Experimental ScreenVane results were then compared to the S-duct computational results. Once again, total pressure distortion results demonstrated excellent agreement with a significant portion of the total pressure recovery profile matching within one percent and nearly all of the remaining portion of the total pressure recovery profile matching within two percent. Swirl angle error was nearly identical to the ScreenVane computational comparison. The isolated setup produced slightly better profile agreement with swirl angle errors measured at approximately two and one half degrees and coupled setup differences reaching almost three degrees across the full-field results.

The experimental analysis proved that total pressure distortion matching was possible using the ScreenVane method and design. Qualitatively, swirl distortion profiles consisted of elements of appropriate size and scale and the paired swirl feature in the lower semi-circular region of the distortion was well represented with the ScreenVane experimental hardware. The significant error in the swirl distortion generation was attributable to relatively small scale features and small misalignments in areas of strong angular gradients leading to amplified error. Overall, the ScreenVane was considered to have performed exceptionally well for the first experimental validation of a novel inlet flow distortion generating device.

Chapter 6 – Evaluating the Turbomachinery

6.1 Overview

The final step toward understanding turbofan engine response to complex inlet flow distortions is conducting experimental tests that produce turbomachinery specific data. This can be achieved in several different ways. Simplified rig tests can indicate changes in component level performance and efficiency through focused isolation of individual engine components. Full scale turbofan engine ground tests can indicate changes in component level performance and efficiency through focused isolation of individual engine components, as well as changes in system level performance and efficiency through comprehensive monitoring of flow and mechanical conditions throughout the turbofan engine system. Full scale flight tests can indicate changes in performance and efficiency in a truly installed configuration. Varying degrees of complexity, expense, and value exist within each test style, but a turbomachinery application is never fully proven until tested in an installed configuration.

For this investigation, a full scale turbofan engine ground test was used to indicate turbomachinery response to combined total pressure and swirl inlet flow distortion. With the specific inlet distortion defined from computational analysis of a conceptual boundary layer ingesting S-duct turbofan engine inlet and a novel distortion generator capable of simultaneously producing combined total pressure and swirl inlet distortion invented, designed, computational analyzed, and experimentally validated, the ScreenVane was once again employed to acquire turbomachinery specific data. Experimental data planes located at the AIP and in the fan rotor exit flow path effectively isolated the component for detailed analysis of fan rotor response to the specific inlet flow distortion. Furthermore, inlet air mass flow specific fuel consumption was monitored to indicate changes in system level performance and efficiency. Based on the agreement between ScreenVane manufactured inlet flow distortions and S-duct manufactured inlet flow distortions, it is expected that impacts on turbomachinery component and system performance generated by ScreenVane manufactured inlet flow distortions will be analogous to S-duct manufactured inlet flow distortions.

The following chapter documents an experimental turbofan engine ground test operating in distorted inflow conditions generated by a ScreenVane combined total pressure and swirl distortion generator. Specifications of the turbofan ground test facility and experimental setup are discussed. Data processing techniques are explained and resulting flow profiles measured at the aerodynamic interface plane (AIP) and the fan rotor exit plane (FREP) are then presented and

examined to indicate fan rotor response to the inlet flow distortion. Additionally, turbofan engine system efficiency analysis is presented and discussed to indicate efficiency changes when the turbofan engine is subjected to distortion ingestion.

6.2 The Turbofan Engine Response Ground Test

6.2.1 Turbofan Engine Ground Test Platform

Turbofan engine response to inlet flow distortion experimental ground tests were conducted in the same turbofan engine ground test facility discussed in Chapter 5, Section 5.2. The significant difference for this series of ground tests was the focus shift from validating the ScreenVane distortion device to measuring the implications of ingested distortion on the performance metrics of the turbofan engine.

The turbofan engine research platform includes instrumentation ports on the fan case that permit flow measurements in the passage between the fan rotor (upstream) and fan exit guide vanes (downstream). Using the fan rotor outlet instrumentation port at top-dead-center, five-hole three-dimensional flow probe measurements were collected in the fan outlet flow stream. Again, the radial traverse and distortion device rotator were critical for collecting full-field flow measurements. Rather than installing multiple data collection devices or moving the data collection devices (each requiring multiple fan case penetrations which reduce structural integrity of the component), the distortion generator incrementally rotated while the radially traversing probe incrementally plunged to fully survey the distortion profile. This was only possible with the assumption that engine hardware was either symmetric or has negligible implications on the distortion development. Because the turbofan engine used in this test includes no upstream hardware (struts, inlet guide vanes, or other) and contains an axisymmetric arrangement of fan exit guide vanes, this assumption was considered satisfied.

The remaining experimental ground test hardware was identical to that discussed in Chapter 5, Section 5.2.

6.2.2 Experimental Setup

The fan rotor exit experimental ground test setup, shown in Figure 6.1, followed the coupled experimental setup (Chapter 5, Section 5.3.2) identically with the exception of the installation of the five-hole three-dimensional flow probe. The downstream flange of the measurement spool was bolted directly to existing hardpoints on the fan case. A universal mounting plate was attached to the thick-walled inlet duct section at top-dead-center and served as a hardpoint for the radial traverse. The radial traverse was then attached to the universal mounting plate, followed by a small rotary table attached to the radially traversing platform. The rotational axis of the small rotary table was aligned with the fan exit instrumentation port. The radial traverse allowed instrumentation to plunge through the fan case wall and across the flow path. The rotary table assisted with instrumentation alignment during installation.

The five-hole three-dimensional flow probe was inserted through the rotary table and fan case wall. Compression fittings on the exterior of the fan case wall as well as the top and bottom of the rotary table secured the probe throughout testing. PTFE ferrules allowed the probe to smoothly plunge radially, while set screw shaft collars located above and below the rotary table mount effectively locked the probe from slipping in the radially traversing mount. Probe installation procedure continued as follows:

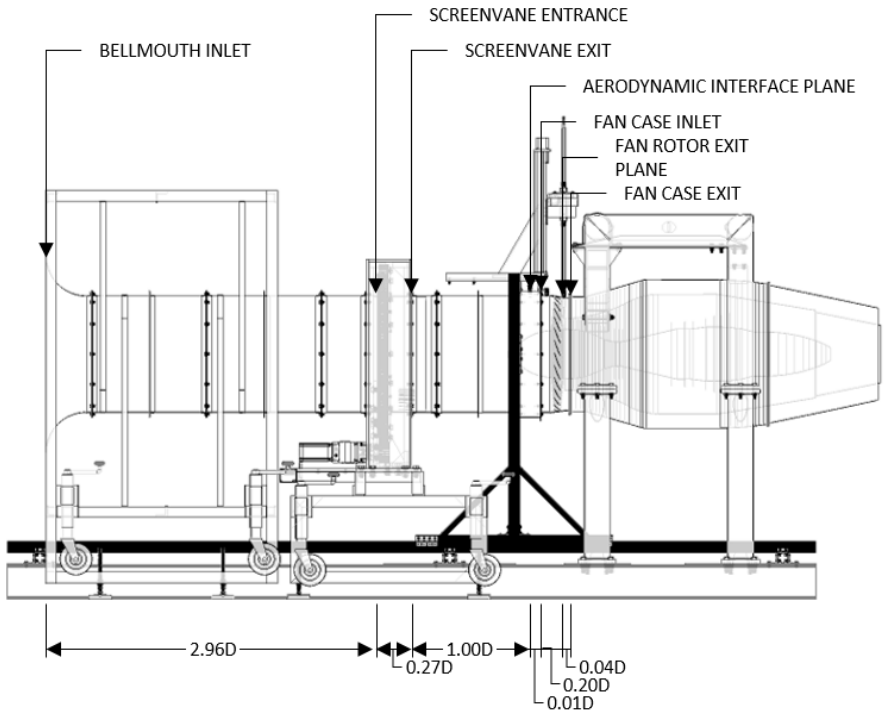

Figure 6.1: Turbofan Engine Response – Ground Test Setup

1) Install the probe through the rotary table and fan case wall compression fittings.
2) Secure the probe within the rotary table using set screw shaft collars to eliminate slip in the radially traversing mount.
3) Retract the tip of the probe just beyond the inner wall of the fan case.
4) Using a small piece of thin shim stock placed flush with the inner wall surface, slowly plunge the probe radially inward until probe tip comes contacts the shim stock. At the instant of contact, the probe is radially "zeroed".
5) Set the limit switch of the radial traverse.
6) Install a custom rotary alignment apparatus to the radial traverse mount. The rotary alignment apparatus consists of a stiff aluminum frame and small free-jet tube. The free-jet tube is assumed to be perpendicular to the engine axis.
7) Extract the probe radially outward until the probe sensing area is aligned with the small free-jet tube.
8) Connect a handheld digital manometer (Dwyer 477A-1) to the yaw angle sensing ports of the probe.
9) Apply compressed air to the free-jet tube.
10) Exploiting the nulling nature of the prism style five-hole three-dimensional flow probe, rotate the rotary table while monitoring the handheld digital manometer until the measured

differential pressure was stable near zero. Once accomplished, the probe is aligned perpendicular to streamwise fluid direction.

11) Rotate the probe 90° to align with the streamwise fluid direction.
12) Rotate the probe a desired offset angle to align with the known fan rotor blade turning angle. By aligning the probe in this manner, the measured relative flow angle will be small and fall near the center of the probe calibration where accuracy is greatest. To determine absolute flow angles, the offset value is simply added to the relative flow angle.

    [Note: Because testing procedure requires both distorted and non-distorted data collection, perfect probe alignment is not critical. This alignment process is only used to ensure that the probe is nearly nulled with flow direction and flow angles are measured in the center of the uniform probe calibration where greatest accuracy is known.]
13) Remove the custom rotary alignment apparatus and handheld digital manometer.
14) Plunge the probe to the zeroed radial position.
15) Connect the five pressure ports to desired pressure scanner channels.
16) Connect the thermocouple plug to the desired temperature acquisition channel.

The remaining experimental ground test setup followed the coupled experimental setup (Chapter 5, Section 5.3.2) identically.

6.2.3 Experimental Test Matrix

Because congruent flow data were desired for comparing fan rotor inlet conditions and fan rotor outlet conditions, the turbofan speed was again set to the maximum safe operating condition of 80% maximum design speed. This resulted in a comparable inlet air mass flow rate (approximately 50 lbm/s) and fan blade tip Mach number (approximately 1.05).

The streamwise location of the fan rotor exit measurement plane was dictated by existing experimental hardware available at the turbofan engine ground test facility. The fan rotor outlet measurement port positioned the measurement plane well within one fan tip chord length (approximately 25% fan tip chord length) from the fan rotor blade trailing edge. This distance was extremely close to the rotating hardware, but was essential for isolating the fan rotor for detailed analysis.

Again, only one test repetition was conducted to maximize spatial resolution within the time and fuel budget. This was only possible by leveraging previous research that focused on uncertainty quantification and reduction through the use of multiple test replications [62,63,79].

For the fan rotor exit test setup, the probe was limited by turbofan engine geometry and constrained to plunge only to the core stream mean line. A technique very similar to the AIP measurement location specification was used to define the fan rotor exit measurement locations. Due to the radial and circumferential motion of the probe and distortion device, a uniformly spaced grid was not appropriate, as inner radii would be unnecessarily highly sampled while outer radii (near wall) would be sparsely sampled. Therefore, engineering judgement was used to distribute data samples to a relatively evenly spaced, non-uniform grid. Radially, measurements were taken at 0.25 – 0.50

inch intervals; circumferentially measurements were taken at 5.00 – 15.00 degree increments. Figure 6.2 illustrates the five-hole three-dimensional flow probe measurement locations at the FREP. As shown, the measurement locations at the innermost radii were located on a sparse circumferential interval. Moving outward from centerline, additional circumferential intervals were incorporated to obtain a nearly evenly spaced arrangement. The smallest circumferential intervals were utilized at the wall where arc length is greatest and significant distortion elements exist. Due to the boundary layer gradients, dense radial increments were used within small distances along the outer wall.

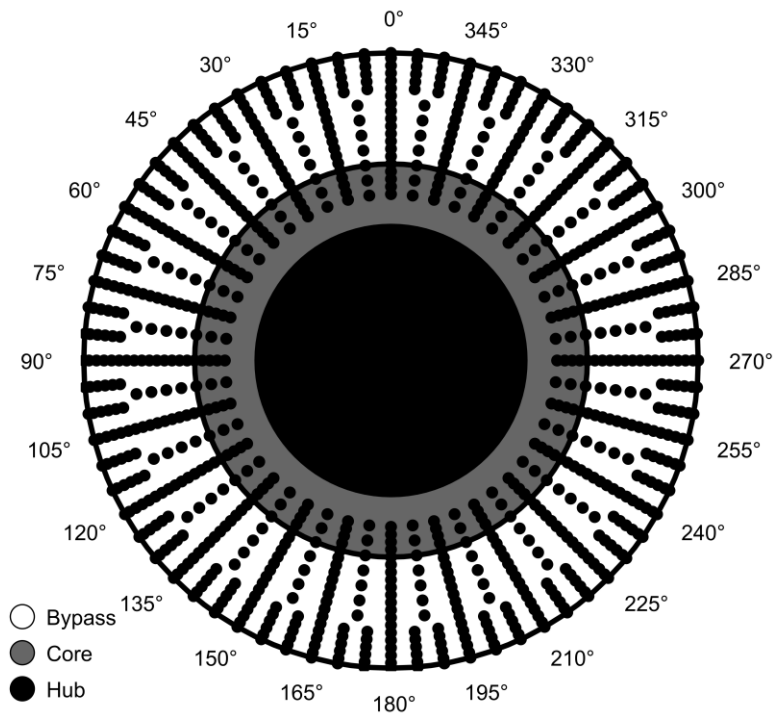

Figure 6.2: Turbofan Engine Response – FREP Measurement Locations

Again using previous experience, data collection and settling times were defined. Experimental data was collected for five seconds at each measurement location to obtain a steady state time-averaged value. After each movement but before each collection, a three second settling period was set to allow the flow to reach steady state conditions. These settings have been proven to provide ample time for an accurate measurement without excessive conservatism.

The following tables summarize the complete turbofan engine ground test matrix used to validate the ScreenVane distortion device.

Table 6.1: Turbofan Engine Response – Engine Settings and Experimental Parameters

Corrected Fan Speed (% Max. of 16000 RPM)	80% Max. (Approx. 12800 RPM)
Fan Blade Tip Speed	1200 ft/s (Approx. 1.05 Mach)
Corrected Inlet Mass Flow Rate	50 lb_m/s (Nominal)
Fan Pressure Ratio	1.35 (Nominal)
Data Sampling Time	5 seconds
Data Settling Time	3 seconds

Table 6.2: Turbofan Engine Response – FREP Measurement Locations

Radial Location	Circumferential Location
r/r_w	θ
0.52	0-345° by 15°
0.55	0-345° by 15°
0.57	0-345° by 15°
0.60	0-345° by 15°
0.62	0-345° by 15°
0.64	0-345° by 15°
0.67	0-345° by 15°
0.69	0-352.5° by 7.5°
0.71	0-352.5° by 7.5°
0.74	0-352.5° by 7.5°
0.76	0-352.5° by 7.5°
0.79	0-352.5° by 7.5°
0.81	0-352.5° by 7.5°
0.83	0-352.5° by 7.5°
0.86	0-355° by 5°
0.88	0-355° by 5°
0.90	0-355° by 5°
0.93	0-355° by 5°
0.95	0-355° by 5°
0.97	0-355° by 5°
0.98	0-355° by 5°

To determine the deviations in flow properties from nominal uniform inlet flow conditions, the ScreenVane was removed from the rotator and replaced and replaced by a uniform wire mesh screen. This screen was made from wire mesh identical to that used as the backer screen material for the total pressure distortion Screen. The use of this screen assisted in controlling inlet air mass flow rates for non-distorted baseline tests. Because the flow was assumed uniform in the non-distorted test, five-hole three-dimensional flow probe measurements were taken at the top-dead-center circumferential location at all plunge depths matching the distorted test. Additionally, a range of fan speeds was tested to bracket the distorted test flow conditions. The absence of the ScreenVane blockage allowed elevated inlet air mass flow rates to enter the turbofan engine. By incrementally varying the fan speed, results were compared at a matching fan speed and matching inlet air mass flow rate.

6.2.4 Experimental Procedure

The fan rotor exit experimental ground test procedure followed the AIP experimental ground test procedure (Chapter 5, Section 5.3.4) identically.

6.3 The Turbofan Engine Response Results

6.3.1 Experimental Data Reduction and Analysis

The fan rotor exit experimental ground test instrument data reduction followed the AIP experimental ground test instrument data reduction (Chapter 5, Section 5.4) identically.

The data analysis technique for monitoring flow conditions through the fan rotor involved observing planar results and calculating impact of distortion on the performance of the turbomachinery. First, planar results at the AIP and fan rotor exit plane (FREP) were compared to make observations about the relative extents, intensities, and locations of significant distortion features. Then, total pressure and total temperature rise through the fan rotor were calculated in an attempt to approximate the impact of distortion on the efficiency and performance of the component. Finally, inlet air mass flow rate specific fuel consumption was calculated to approximate the impact of distortion on the efficiency and performance of the turbofan system.

Where appropriate, results are compared at both equivalent fan spool speed and inlet air mass flow rate. Additionally, the following key assists several of the plots.

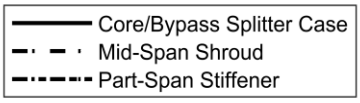

Figure 6.3: Turbofan Engine Response – Profile Results Key

6.3.2 Total Pressure Distortion Profile

Total pressure distortion profiles measured at the AIP and FREP are presented in Figure 6.4. The circular cross sections (left) illustrate the full-field planer total pressure recovery as normalized by the maximum in-plane total pressure measured at the AIP (Equation 6.1). The circumferential trends (right) unwrap the distortion profile beginning at top-dead-center (0°), moving counterclockwise through bottom-dead-center (180°), and returning counterclockwise to top-dead-center (360°). The colors displayed here correspond to normalized radius. All results are presented forward-looking-aft.

From these profiles, the highly discretized AIP total pressure distortion was well mixed through interactions with the rotor. Along the tip radii, the fan rotor recovered to a near uniform exit total pressure. Blade geometry was discovered to have a significant effect on the mixing of the distortion with annuli of relatively constant total pressure recovery bounded by the part-span stiffener, the mid-span shroud, and the core/bypass splitter case.

The significant feature of the exit total pressure recovery results was the relatively poor fan rotor recovery near the hub as it rotates counter-clockwise into the low recovery region. With information about the flow direction at the AIP known, it was determined that the low fan total pressure recovery at this location was attributable to co-swirling flow. The co-swirl reduced the

work of the fan rotor and decreased the local total pressure rise through the fan. As the fan cycles through bottom-dead-center, rotor incidence angles switch to a counter-swirl condition resulting in increased fan rotor work and elevated pressure rise.

$$R_0 = \frac{P_0}{\max(P_{0_{AIP}})} \tag{6.1}$$

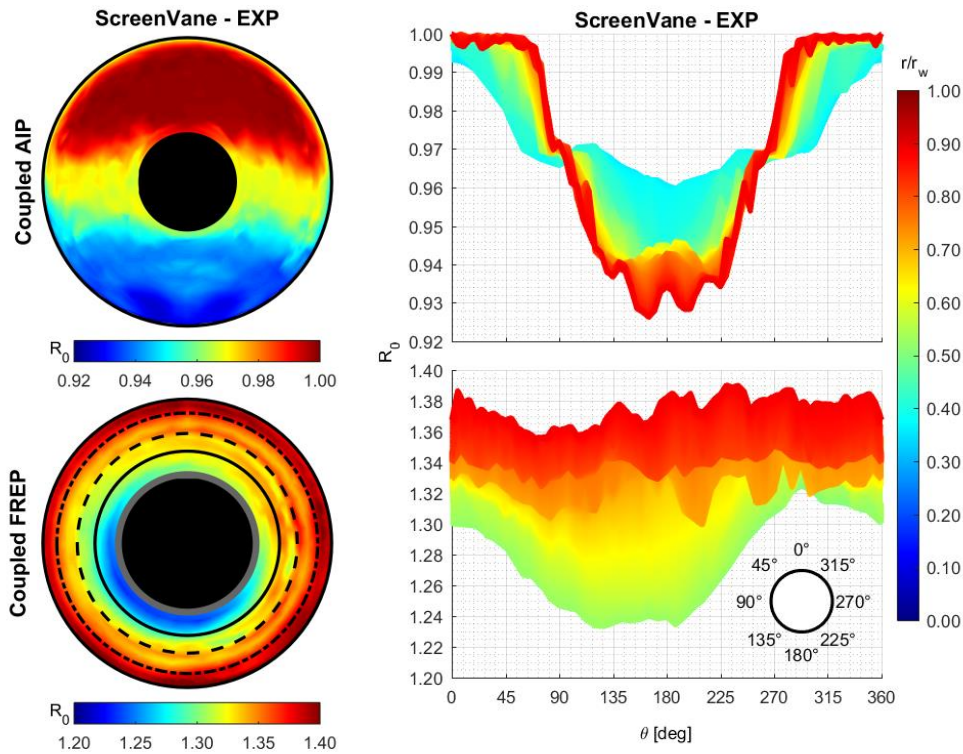

Figure 6.4: Turbofan Engine Response – Total Pressure Recovery Profiles and Trends

6.3.3 Swirl Distortion Profile

Swirl distortion profiles measured at the AIP and FREP are presented in Figure 6.5. The circular cross sections (left) illustrate the full-field planer swirl angle. The circumferential trends (right) unwrap the distortion profile beginning at top-dead-center (0°), moving counterclockwise through bottom-dead-center (180°), and returning counterclockwise to top-dead-center (360°). The colors displayed here correspond to normalized radius. All results are presented forward-looking-aft.

From the contours, it was apparent that co-rotating swirl was more difficult to overcome than counter-rotating swirl. The maximum positive swirl angle remained nearly unchanged through interactions with the fan rotor. Conversely, the counter-rotating, negative swirl was nearly eliminated through interactions with the fan rotor. This finding was again attributed to incidence angle and work done by the fan rotor. A co-swirling flow reduces the overall turning of the blade (assuming the flow remains attached) which reduces the work and results in the fan pushing the air rather than turning.

Further evidence of this phenomenon was found in the circumferential trends of swirl angle. Both the inlet (AIP) and exit (FREP) swirl angle profiles exhibited a full-cycle once-per-revolution pattern as well as a limited extent paired-swirl distortion. Upon inspection, the larger scale distortion feature was phase shifted approximately 60° in the direction of fan rotation (counter-clockwise) with dramatic intensity attenuation of approximately 50%. The smaller scale distortion feature remained mostly intact with nearly negligible attenuation, especially in the positive direction.

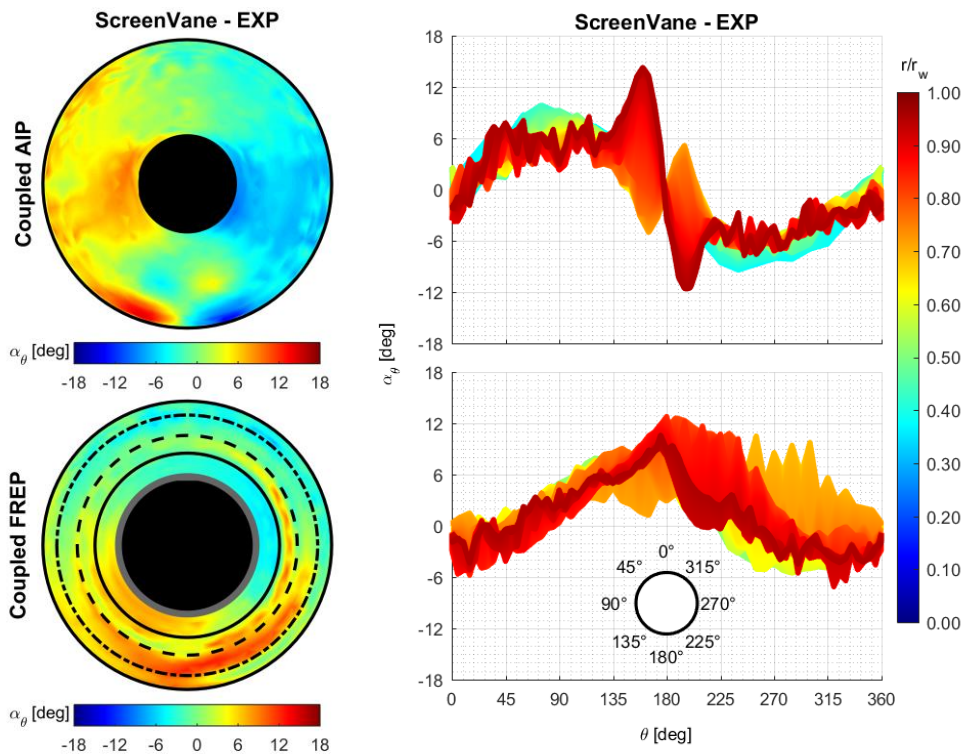

Figure 6.5: Turbofan Engine Response – Swirl Angle Profiles and Trends

6.3.4 Fan Rotor Adiabatic Efficiency

With total pressure and total temperature measurements surrounding the fan rotor, an attempt was made to approximate the impact of distortion on the fan rotor adiabatic efficiency. The process began with collecting and processing both distorted and non-distorted (nominal) flow measurements. In the case of the non-distorted inlet flow test, a range of fan speeds was surveyed to generate data that matched the distorted inlet flow test fan speed and bracketed the distorted inlet air mass flow rate.

The collected and processed data was then interpolated to an equal area grid such that area weighted face averaged and mass flow weighted face averaged total pressure and total temperature could be calculated. The weighted face averaged fan rotor exit values were then normalized by the AIP counterparts to obtain fan total pressure ratio (Equation 6.2) and fan total temperature ratio (Equation 6.3). Finally, the adiabatic fan efficiency was calculated (Equation 6.4).

$$FTPR = \frac{areaAve(P_{0_{FREP}})}{areaAve(P_{0_{AIP}})} \quad and \quad FTPR = \frac{massAve(P_{0_{FREP}})}{massAve(P_{0_{AIP}})} \tag{6.2}$$

$$FTTR = \frac{areaAve(T_{0_{FREP}})}{areaAve(T_{0_{AIP}})} \quad and \quad FTTR = \frac{massAve(T_{0_{FREP}})}{massAve(T_{0_{AIP}})} \tag{6.3}$$

$$\eta_f = \frac{FTPR^{\frac{\gamma-1}{\gamma}} - 1}{FTTR - 1} \tag{6.4}$$

The resulting trends across the surveyed fan speeds and associated inlet mass flow rates are presented in Figure 6.6 and Figure 6.7, respectively.

While the weighted face average total pressure was reduced in both the inlet and exit flow fields of the distorted inlet flow test, the total pressure ratio remained nearly unchanged when compared to the non-distorted inlet flow test at the test fan speed of 80%. Likewise, the fan total temperature ratio was negligibly impacted by the existence of distortion and the approximated adiabatic efficiency indicated insignificant change under nominal or distorted test conditions, regardless of weighted average calculation method. This result should be considered specific to this particular engine and distortion investigation.

The inlet air mass flow rate was significantly reduced in the presence of distortion. This result indicates that while the calculated fan rotor component efficiency was unaffected by the distorted inlet flow, the overall system efficiency was likely reduced due to increased shaft speeds required to move equivalent volumes of air.

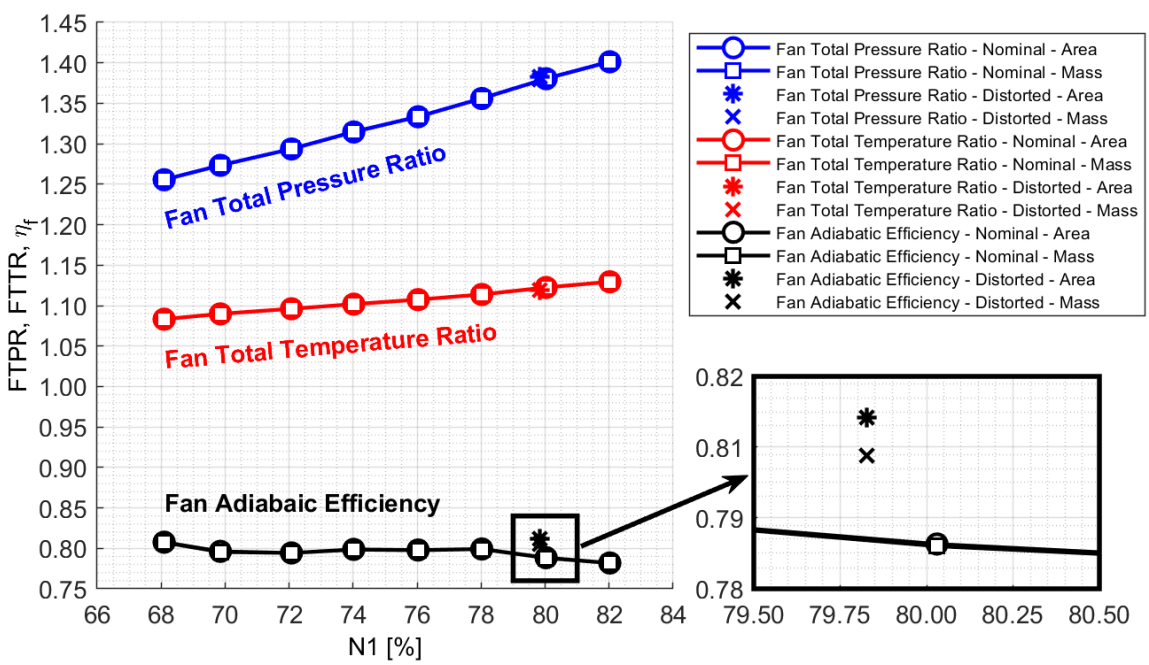

Figure 6.6: Turbofan Engine Response – Equivalent Mechanical Speed Fan Performance

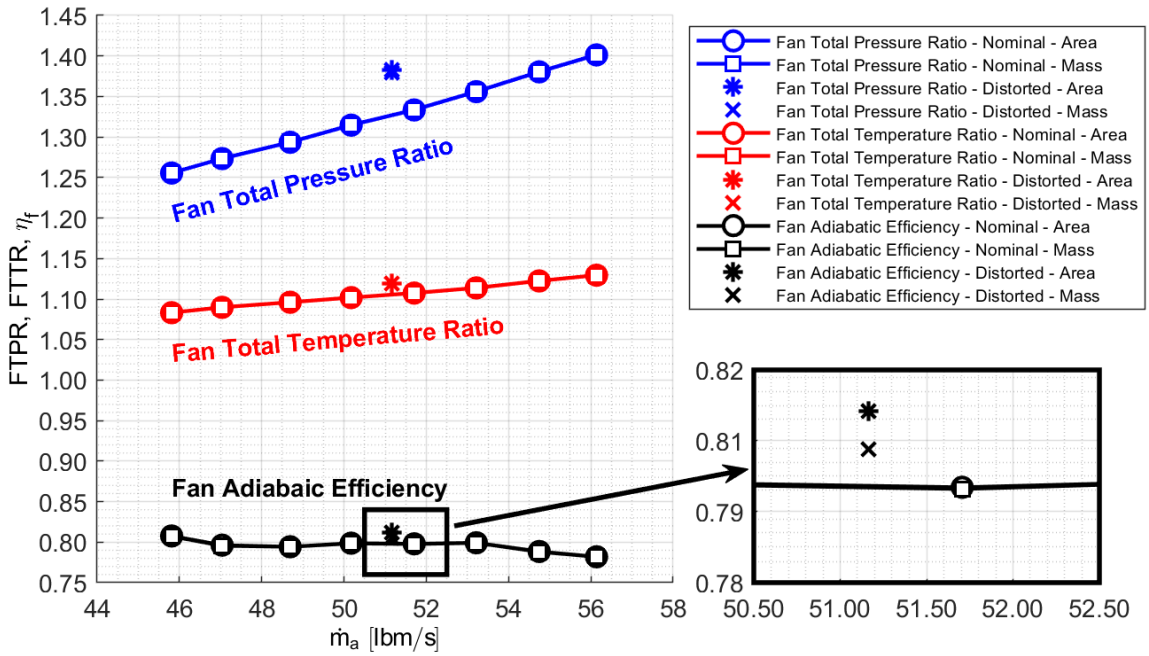

Figure 6.7: Turbofan Engine Response – Equivalent Mass Flow Fan Performance

6.3.5 Inlet Air Mass Flow Specific Fuel Consumption

Continuing from the observation that inlet air mass flow rate was significantly reduced in the presence of the distortion at a constant fan speed, fuel consumption measurements indicated system level performance and efficiency impact. The inlet air mass flow specific fuel consumption is a measure of the energy required to move air and create thrust. While no thrust measurements were collected for this investigation, the inlet air mass flow specific fuel consumption variation can be considered similar to the thrust specific fuel consumption.

The inlet air mass flow rate and the fuel consumption rate were monitored at each probe measurement location resulting in a large data set as these parameters were assumed independent of distortion location. Inlet air mass flow specific fuel consumption was calculated using Equation 6.5 and is presented in Figure 6.8 across the surveyed fan speeds included in this investigation.

$$\dot{m}SFC = \frac{\dot{m}_f}{\dot{m}_a} \tag{6.5}$$

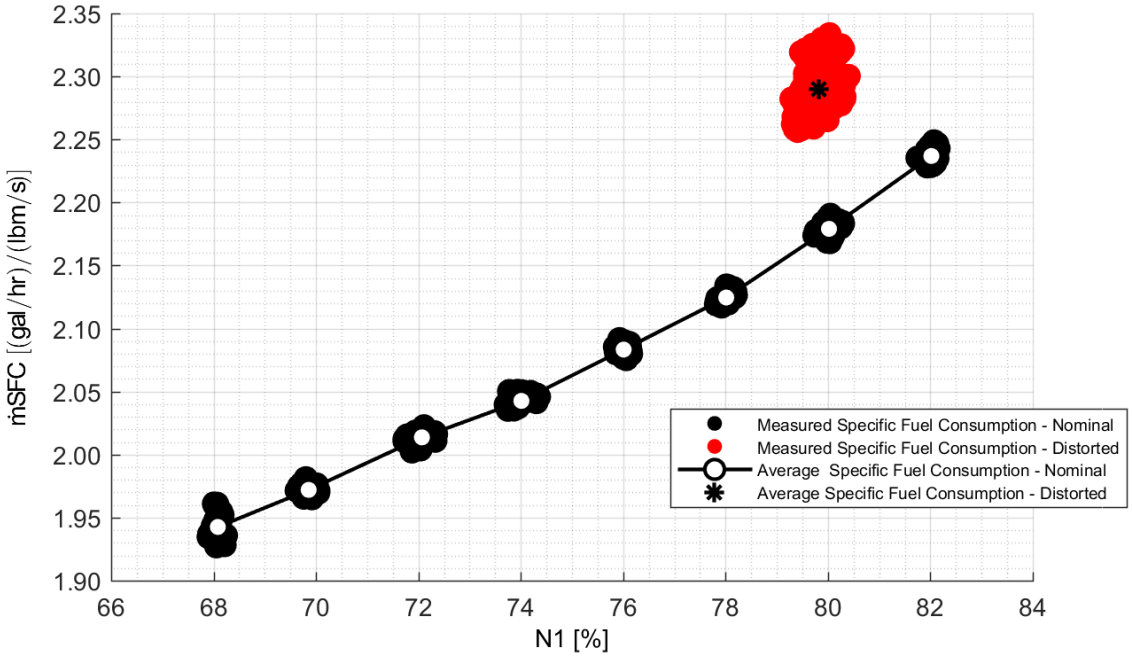

Figure 6.8: Turbofan Engine Response – Equivalent Mechanical Speed System Efficiency

The resulting inlet air mass flow specific fuel consumption increased more than 5% in the distorted inlet flow test when compared to the non-distorted inlet flow test at the test fan speed of 80%. While the specific fuel consumption was elevated in the distorted inlet flow condition, it did not necessarily indicate a poor inlet design or a poor inlet/engine match; rather, the inlet distortion caused turbofan system efficiency degradation that must be overcome by the benefits of optimized boundary layer ingestion aircraft configurations.

6.4 Summary

A follow on turbofan engine ground test was conducted to acquire data in support of turbofan engine response to ScreenVane manufactured combined total pressure and swirl distortion ingestion. A rigorous and thorough test setup and procedure was designed and followed to examine the implications of operating a turbofan engine with continuous inlet flow distortion. Identical experimental hardware used during ScreenVane experimental validation ground testing was repurposed and installed in the fan rotor outlet flow path (immediately downstream of the fan rotor and immediately upstream of the fan exit guide vanes). Fan speed was set to 80% to allow sufficient turbomachinery stability margin and maintain safe continuous operating conditions while ingesting an inlet air mass flow rate of approximately 50 lb_m/s.

By examining flow data at the AIP and FREP, the fan rotor was effectively isolated for component analysis. Highly discretized AIP total pressure distortion was well mixed through interactions with the fan rotor. The fan rotor tip was found to recover to near uniform circumferential total pressure while total pressure recovery was poorest at hub radii especially as the fan approached the low pressure region in the lower semi-circular region of the flow distortion. The fan response

to swirl distortion indicated that co-rotating swirl was more difficult to overcome than counter-rotating swirl as significant co-rotating swirl existed in the fan rotor exit measurement plane while counter-rotating swirl was nearly mitigated. Swirl angle measurements also indicated that relatively large extent distortions were significantly attenuated through fan interactions and phase shifted along the direction of fan rotation while relatively small extent distortions pass nearly unchanged through fan interactions.

Critically evaluating both the total pressure and swirl angle profiles exiting the fan rotor simultaneously led to several interesting observations. Fan rotor features and internal engine geometry was discovered to have a significant effect on the mixing of the distortion with annuli of relatively constant total pressure recovery and swirl angle bounded by the part-span stiffener, the mid-span shroud, and the core/bypass splitter case. The combination of co-rotating swirl and negative total pressure gradient experienced as the fan rotor cycled counter-clockwise from top-dead-center to bottom-dead-center reduced the local blade incidence angle, blade turning effectiveness, blade work output, and total pressure rise in this region. As the fan cycles through bottom-dead-center, rotor incidence angles switch to a counter-swirl condition and the total pressure gradient becomes positive resulting in increased fan rotor work and elevated pressure rise.

Fan rotor performance was measured by calculating the adiabatic efficiency of the component using weighted face averaged total pressure ratio and total temperature ratio. Fan total pressure and total temperature ratios were dependent on fan speed. At constant fan speed, the overall total pressure and total temperature ratios demonstrated negligible change from non-distorted inlet conditions resulting in insignificant changes in adiabatic efficiency. Examining the inlet air mass flow rate between the distorted and non-distorted inflow conditions demonstrated that while total pressure and total temperature ratios remained constant at constant fan speed, the inlet air mass flow was significantly reduced by approximately 4%. This result should be considered specific to this particular engine and distortion investigation.

Because mechanical speed was controlled by turbine energy extraction from combusted fuel, the fuel consumption was constant at constant fan speed. As discussed, the inlet air mass flow rate was reduced in the distorted test configuration when compared to nominal inlet air mass flow rate in the non-distorted test configuration. The inlet air mass flow specific fuel consumption increased by more than 5% when subjecting the turbofan engine to inlet flow distortion ingestion. While the specific fuel consumption was elevated in the distorted inlet flow condition, it did not necessarily indicate a poor inlet design or a poor inlet/engine match; rather, the inlet distortion caused turbofan system efficiency degradation that must be overcome by the benefits of optimized boundary layer ingestion aircraft configurations.

Chapter 7 – Summary

7.1 Motivation for the Current Investigation

Modern conceptual aircraft designs are increasingly shifting turbofan engine installations away from pylon mounts in conventional tube-and-wing airframes toward highly integrated, often embedded, engine/airframe arrangements associated with boundary layer ingesting blended wing body architectures. These unified engine/airframe systems offer superior efficiency and performance in terms of lift-to-drag ratio, fuel consumption, range, and noise abatement and are currently viewed as the most promising solution to rising fuel costs, ever tightening airfield restrictions, and declining passenger comfort.

Boundary layer ingestion is a potentially revolutionary technology advancement for the aviation industry. Capitalizing on the benefits of boundary layer ingestion requires focused research and development of propulsion system components into integrated engine/airframe configurations. Significant challenges encountered by turbofan engines installed in conceptual next generation aircraft designs center on inlet flow distortion interaction with the initial stages of the turbomachinery. Solving these challenges requires innovative ground test equipment that enhance experimental investigations allowing for design optimization. This ground test hardware must be cost-effective, rapidly produced, easily iterated, and accurate.

Short of full-scale coupled turbofan engine/inlet wind tunnel tests, there currently exists no extensively validated technology capable of accurately simulating complex, non-uniform inlet flow conditions, composed of both total pressure and swirl distortions, for turbofan engine ground tests. Previously, inlet total pressure distortion elements and inlet swirl distortion elements have been decoupled for ground test purposes. As a contribution to the ongoing turbofan engine integration research efforts throughout the aviation industry, a novel technology, the ScreenVane combined total pressure and swirl distortion device, was invented and motivated the current investigation.

The current state-of-the-art total pressure distortion generators claim profile reproduction accuracy within ±1.0% total pressure recovery while swirl distortion generators claim profile reproduction accuracy within ±1.5° swirl angle. Therefore, as an aggressive goal, the new combined device was intended to match both inlet total pressure and swirl distortion profiles within similar margins. Once validated, the remaining objective of the current research was to quantify effects of inlet distortion on turbofan engine performance and efficiency through component and system analysis.

7.2 Defining the Distortion

The first step toward understanding turbofan engine response to complex inlet flow distortions is to define the distortion profile. For the current investigation, the distortion profile was defined using computational analysis of a conceptual boundary layer ingesting S-duct turbofan engine inlet. The geometry was modeled at an appropriate scale, and computational analysis was conducted at flow conditions matching the size and capabilities of the turbofan engine ground test platform at the Virginia Tech Turbomachinery and Propulsion Research Laboratory. Defining the initial distortion using a predetermined engine/inlet configuration produced results that were readily applicable to distortion device design. While this analysis approach is not necessarily required, it does remove any scaling of the distortion profile geometrically, aerodynamically, or otherwise.

A computational case study was conducted to develop a portfolio of turbofan engine inlet flow distortion profiles. A single bend S-duct boundary layer ingesting turbofan engine inlet served as a candidate inlet geometry grounded in reality and relevance. Varying amounts of boundary layer ingestion spanned a predicted range for aircraft inlets of this design. Baseline flow analysis performed with the inlet duct isolated from turbofan hardware was compared to turbofan flow analysis performed with the inlet duct coupled to simplified turbofan hardware.

By systematically varying the amount of boundary layer ingestion, the case study produced corresponding AIP flow profile results with varying extents and intensities of total pressure and swirl distortion. From analysis and observations, the underlying features (including a once-per-revolution total pressure distortion and paired-swirl swirl distortion) of the distortion profiles were largely independent of the amount of boundary layer ingested. This was especially true at the upper end of the tested boundary layer heights, greater than approximately 20% entrance height. Further evaluation of the AIP results indicated that the generated distortions generally increase in intensity with increasing amounts of boundary layer ingestion. This was especially true at the lower end of the tested boundary layer heights, less than approximately 20% entrance height, where distortion intensities rapidly increased in magnitude.

7.3 Designing the Distortion Generator

In the current investigation, a single AIP distortion profile from the S-duct turbofan inlet computational case study results was selected as the candidate profile for ScreenVane design, validation, and ground testing. The candidate profile was desired to produce significant levels of distortion to demonstrate the current state-of-the-art ScreenVane methodology while maintaining realistic flow conditions simulating embedded turbofan engine installations; therefore, the single case for ScreenVane development was selected to be 25% BLI. This case aligned with predicted boundary layer ingestion amounts found in conceptual aircraft, yielded measurable distortion levels, and encompassed attributes of resulting distortion profiles from over half of the case study. The selection also posed a significant challenge to turbomachinery due to the concentration of distortion near the wall and the increased susceptibility of blade tip stall.

Once the candidate profile was selected, the first step in ScreenVane design involved inverse propagation of the distortion to create an axial separation between the physical device and the measurement plane. The axial separation was necessary for two reasons; to allow wake disturbances to dissipate prior to the measurement plane and to allow for installation into the experimental ground test hardware. The wake disturbances associated with total pressure distortion screens and swirl distortion StreamVanes created unintentional distortion in the device outlet flow; therefore, it was desirable to allow sufficient streamwise development length to mix these small scale features into the bulk flow. Constraints within the experimental turbofan engine ground test facility also required axial separation between the distortion generators and measurement planes. Based on available hardware and equipment at the facility, the axial separation distance was set to one fan diameter from the ScreenVane design plane (or trailing edge of the StreamVane component) and the aerodynamic interface plane (AIP). The known AIP profile was then projected upstream to the ScreenVane design plane using a vorticity transport method with total pressure corrections. This new upstream profile served as the desired flow conditions to be manufactured by the ScreenVane combined total pressure and swirl distortion device. The flow profile then exited the ScreenVane and naturally developed into the desired AIP distortion profile at the AIP.

ScreenVane design then followed conventional total pressure distortion Screen and swirl distortion StreamVane design practices. The Screen component consisted of varying layers of fine wire mesh installed in the flow to generate tailored total pressure losses according to the desired total pressure distortion profile. The StreamVane component consisted of a unique arrangement of turning vanes installed in the flow to generate the tailored secondary flow according to the desired swirl distortion profile. Combining the two devices by installing the Screen immediately upstream of the StreamVane resulted in the ScreenVane combined total pressure and swirl distortion generator.

7.4 Analyzing the Distortion Generator

Computational analysis of the ScreenVane combined total pressure and swirl distortion generator was conducted to verify that the device manufactured appropriate flow conditions simulating the S-duct turbofan inlet. Of interest, the ability of the ScreenVane to match total pressure recovery and swirl angle profiles at the AIP was quantified. This procedure was necessary to verify and iterate the ScreenVane design prior to fabrication of turbofan engine ground test equipment.

The ScreenVane computational domains were similar to the S-duct turbofan inlet case study. Matching AIP locations were used in isolated and coupled configurations to provide congruent data sets for comparison of S-duct generated flow distortions and ScreenVane generated flow distortions. This process involved modeling the Screen and StreamVane components and subjecting the ScreenVane to turbofan engine inlet flow rates. The Screen component was simulated using porous domain settings that match analytical loss models. The StreamVane component was simulated as a series of solid turning vanes submerged in the inlet flow. Boundary conditions were desired to match the turbofan ground test facility with air ingested at standard atmospheric conditions and propelled to a flow rate of approximately 50 lb_m/s.

ScreenVane generated distortion profiles were extracted at the AIP for analysis and comparison to S-duct generated distortions. Total pressure recovery results demonstrated excellent profile generation and agreement to the desired S-duct total pressure distortion profile. Full-field total pressure recovery error was measured to be less than one percent for both the isolated and coupled domains. Swirl angle results indicated excellent reproduction of significant distortion features (paired-swirl located near bottom-dead-center) with moderate agreement to full-field error approximated to two and one half degrees. The error was found to be greatly influenced by small discrepancies in distortion gradients; however, as a first attempt at a novel combined distortion generator, these errors were considered acceptable to warrant experimental testing and validation.

7.5 Validating the Distortion Generator

Turbofan engine ground tests were conducted to verify the ScreenVane design methodology and to validate computational models. Experimental hardware was manufactured and installed in the inlet duct of a turbofan engine ground test platform. A rigorous and thorough test setup and procedure was designed and followed to examine the capability of the ScreenVane to produce a combined total pressure and swirl distortion profile matching predicted flow conditions exiting an S-duct turbofan engine inlet.

The ScreenVane experimental setups matched computational analysis simulations in configuration, scale, and initial flow conditions. Fan speed was set to 80% to allow sufficient turbomachinery stability margin and maintain safe continuous operating conditions while ingesting an inlet air mass flow rate of approximately 50 lb_m/s. Furthermore, identical AIP locations were used in isolated and coupled configurations to provide congruent data sets for comparison of ScreenVane experimental results to both predicted ScreenVane computational results and to S-duct computational results.

ScreenVane generated distortion profiles were measured at the AIP for analysis and comparison to computational predictions. Experimental results were first compared to ScreenVane computational results. In both the isolated and coupled setups, the experimental and computational total pressure distortion results agreed exceptionally well with nearly the entire total pressure recovery profile matching within one percent. Swirl angle agreement errors between the experimental and computational results were slightly larger, with the majority of the flow profile matching within one and one half degrees for the isolated setup and two and one half degrees in the coupled setup. This error was found to be strongly dependent on the relatively small scale distortion features and large gradients within the distortion features which locally amplified discrepancies.

Experimental ScreenVane results were then compared to the S-duct computational results. Once again, total pressure distortion results demonstrated excellent agreement with a significant portion of the total pressure recovery profile matching within one percent and nearly all of the remaining portion of the total pressure recovery profile matching within two percent. Swirl angle error was nearly identical to the ScreenVane computational comparison. The isolated setup produced slightly better profile agreement with swirl angle errors measured at approximately two and one

half degrees and coupled setup differences reaching almost three degrees across the full-field results.

The experimental analysis proved that total pressure distortion matching was possible using the ScreenVane method and design. Qualitatively, swirl distortion profiles consisted of elements of appropriate size and scale and the paired swirl feature in the lower semi-circular region of the distortion was well represented with the ScreenVane experimental hardware. The significant error in the swirl distortion generation was attributable to relatively small scale features and small misalignments in areas of strong angular gradients leading to amplified error. Overall, the ScreenVane was considered to have performed exceptionally well for the first experimental validation of a novel inlet flow distortion generating device.

7.6 Evaluating the Turbomachinery

A follow on turbofan engine ground test was conducted to acquire data in support of turbofan engine response to ScreenVane manufactured combined total pressure and swirl distortion ingestion. A rigorous and thorough test setup and procedure was designed and followed to examine the implications of operating a turbofan engine with continuous inlet flow distortion. Identical experimental hardware used during ScreenVane experimental validation ground testing was repurposed and installed in the fan rotor outlet flow path (immediately downstream of the fan rotor and immediately upstream of the fan exit guide vanes). Fan speed was set to 80% to allow sufficient turbomachinery stability margin and maintain safe continuous operating conditions while ingesting an inlet air mass flow rate of approximately 50 lb_m/s.

By examining flow data at the AIP and FREP, the fan rotor was effectively isolated for component analysis. Highly discretized AIP total pressure distortion was well mixed through interactions with the fan rotor. The fan rotor tip was found to recover to near uniform circumferential total pressure while total pressure recovery was poorest at hub radii especially as the fan approached the low pressure region in the lower semi-circular region of the flow distortion. The fan response to swirl distortion indicated that co-rotating swirl was more difficult to overcome than counter-rotating swirl as significant co-rotating swirl existed in the fan rotor exit measurement plane while counter-rotating swirl was nearly mitigated. Swirl angle measurements also indicated that relatively large extent distortions were significantly attenuated through fan interactions and phase shifted along the direction of fan rotation while relatively small extent distortions pass nearly unchanged through fan interactions.

Critically evaluating both the total pressure and swirl angle profiles exiting the fan rotor simultaneously led to several interesting observations. Fan rotor features and internal engine geometry was discovered to have a significant effect on the mixing of the distortion with annuli of relatively constant total pressure recovery and swirl angle bounded by the part-span stiffener, the mid-span shroud, and the core/bypass splitter case. The combination of co-rotating swirl and negative total pressure gradient experienced as the fan rotor cycled counter-clockwise from top-dead-center to bottom-dead-center reduced the local blade incidence angle, blade turning effectiveness, blade work output, and total pressure rise in this region. As the fan cycles through

bottom-dead-center, rotor incidence angles switch to a counter-swirl condition and the total pressure gradient becomes positive resulting in increased fan rotor work and elevated pressure rise.

Fan rotor performance was measured by calculating the adiabatic efficiency of the component using weighted face averaged total pressure ratio and total temperature ratio. Fan total pressure and total temperature ratios were dependent on fan speed. At constant fan speed, the overall total pressure and total temperature ratios demonstrated negligible change from non-distorted inlet conditions resulting in insignificant changes in adiabatic efficiency. Examining the inlet air mass flow rate between the distorted and non-distorted inflow conditions demonstrated that while total pressure and total temperature ratios remained constant at constant fan speed, the inlet air mass flow was significantly reduced by approximately 4%. This result should be considered specific to this particular engine and distortion investigation.

Because mechanical speed was controlled by turbine energy extraction from combusted fuel, the fuel consumption was constant at constant fan speed. As discussed, the inlet air mass flow rate was reduced in the distorted test configuration when compared to nominal inlet air mass flow rate in the non-distorted test configuration. The inlet air mass flow specific fuel consumption increased by more than 5% when subjecting the turbofan engine to inlet flow distortion ingestion. While the specific fuel consumption was elevated in the distorted inlet flow condition, it did not necessarily indicate a poor inlet design or a poor inlet/engine match; rather, the inlet distortion caused turbofan system efficiency degradation that must be overcome by the benefits of optimized boundary layer ingestion aircraft configurations.

Chapter 8 – Conclusions

8.1 The ScreenVane Inlet Distortion Generator

8.1.1 Validation of the ScreenVane Methodology

Prior to this investigation, turbofan engine inlet distortion ground tests were either limited in scope (using decoupled total pressure distortion or swirl distortion devices) or overwhelmingly complicated (using full-scale turbofan engine/inlet hardware and wind tunnel simulated flight conditions). The ScreenVane combined total pressure and swirl distortion generator has been shown to replicate an example S-duct inlet manufactured distortion profile with high accuracy. Total pressure profile reproduction was computationally verified within one-percent total pressure recovery error and experimentally validated within one and one-half percent total pressure recovery error. Swirl distortion profile reproduction was computationally verified within two and one-half degrees swirl angle and experimentally validated within three degrees swirl angle. In each parameter, significant distortion features were qualitatively well matched in pattern, shape, extent, and intensity.

The results of this investigation, while specific to a single distortion profile, indicated that the ScreenVane technology has been developed to a level compatible with full-scale turbofan engine experimental ground tests. The device was proven to have sufficient strength and durability to survive the flow conditions entering a turbofan engine while providing sufficient fidelity to simulate the specified distortion profile. Following the methodology outlined in this investigation, nearly any combined total pressure and swirl distortion profile can be replicated through the use of a ScreenVane.

8.1.2 Recommendations for Improving the ScreenVane Methodology

Several areas for methodology improvement exist. Updating the existing two-dimensional inverse flow propagation solver and total pressure correction with a full three-dimensional flow propagation solver would enhance the definition of the ScreenVane design profile. Improved pressure Screen and StreamVane interaction prediction would enhance the distortion profile matching. Optimized Screen and StreamVane manufacturing processes including variable wire mesh porosity and reduced loss airfoil vane geometry would enhance device capabilities. While the resulting errors in total pressure and swirl distortion were slightly greater than the aggressive

goals defined at the beginning of this investigation, for an initial attempt at end-to-end ScreenVane design and deployment, beginning with a realistic distortion profile and culminating with a full-scale turbofan engine test, the results of this investigation were extremely promising.

8.1.3 Potential Impact on the Future of Turbofan Engine Ground Test Practices

The ScreenVane combined total pressure and swirl distortion device has been evaluated in a turbofan engine experimental ground test facility. The turbofan inlet distortion profile manufactured by the device closely matched the resulting distortion profile manufactured by an arbitrary S-duct inlet. Furthermore, the ScreenVane distortion profile interacted with turbomachinery in a similar manner to the predicted inlet duct distortion profile. These conclusions validate the ScreenVane for use in turbofan engine inlet distortion ground tests where simultaneously tailored total pressure and swirl distortion profiles are desired. This device has the potential to complement full-scale turbofan engine/inlet hardware tested at wind tunnel simulated flight conditions by providing the ability to rapidly iterate inlet design as well as test implications of turbofan engine inlet distortion ingestion.

Prior to this investigation there existed no combined inlet total pressure and swirl distortion simulator for turbofan engine experimental ground test applications; with the invention of the ScreenVane, there now does.

8.2 The Turbofan Engine Response to Inlet Distortion

8.2.1 Influence of the Turbofan Engine on the Inlet Distortion

At the conclusion of this investigation, several significant results relating to the influence of the turbofan engine on the inlet distortion were discovered.

In the flow upstream of the fan rotor, the fan rotor blades were found to have negligible effect on the distortion profile development. By comparing simplified CFD (devoid of fan rotor blades) with experimental results (in close proximity to the fan rotor blades), nearly no difference was computed. This was not true with the nose cone centerbody effects. The solid body avoidance, combined with significant area reduction, accelerated flow in both the radial and axial directions. The net result was an attenuation of swirl angle entering the fan rotor. This finding had significance due to the incidence angle entering the fan rotor blade more closely matching non-distorted inlet flow conditions.

In the flow downstream of the fan rotor, interactions with the turbofan engine component were shown to have significant effects on the distortion profile. The total pressure profile exiting the fan rotor was well mixed circumferentially by the fan rotor; however, blade and engine geometry features (mid-span shroud, part-span stiffener, and core/bypass splitter case) bounded annuli of relatively constant total pressure. Additionally, the fan rotor was discovered to have reduced performance entering a low total pressure recovery region compared to exiting. The swirl angle

profile exiting the fan rotor was also well mixed circumferentially, especially in the counter-rotating regions of swirl. These results implied that the fan rotor generally contributes to a decrease in distortion exiting the component; however, distortion elements were proven to exist in the fan rotor outlet flow.

8.2.2 Influence of the Inlet Distortion on the Turbofan Engine

At the conclusion of this investigation, several significant results relating to the influence of the inlet distortion on the turbofan engine were discovered.

Fan rotor component level analysis was conducted through the calculation of total pressure ratio, total temperature ratio, and adiabatic efficiency. Although the weighted face averaged total pressures entering and exiting the component were decreased in the presence of distortion, the total pressure ratio across the fan rotor remained constant between distorted and non-distorted conditions. This result indicated that the fan rotor essentially operated at a reduced inlet total pressure condition and never experienced stall conditions. The total temperature ratio across the fan rotor also remained constant between distorted and non-distorted conditions. This result indicated that the work input to the flow at a matching mechanical fan speed was constant and that the average turning produced by the fan rotor was constant between distorted and non-distorted conditions.

These results were only possible if the fan rotor aerodynamic losses were negligible (weak distortion with no stall) and/or reversible (symmetric distortion with no stall). In the current investigation, the symmetric distortion profile contributed to balanced performance fluctuations in the fan rotor component. The increased performance attributed to counter-rotating swirl offset the decreased performance attributed to co-rotating swirl resulting in negligible changes in fan rotor work. Because fan rotor work was constant, total temperature ratio across the fan rotor was also constant between distorted and non-distorted conditions. Since the total pressure distortion was not adequately severe to cause fan rotor stall, the inlet swirl distortion was not adequately severe to cause fan rotor flow separation, and the combined total pressure and swirl distortion was symmetric, a negligible change in fan rotor adiabatic efficiency was discovered.

Turbofan engine system level analysis was conducted through the calculation of inlet air mass flow specific fuel consumption. In the current investigation, the specific fuel consumption increased by approximately 5% under distorted inlet conditions. The result indicated that the turbofan system required increased energy input to move an equivalent volume of air. This result also indicated that in order to move an equivalent volume of air, an increase in mechanical speed was necessary. This increase in mechanical speed reduces stall margin in rotating components and limits operability. While the specific fuel consumption was elevated in the distorted inlet flow condition, it did not necessarily indicate a poor inlet design or a poor inlet/engine match; rather, the inlet distortion caused turbofan system efficiency degradation that must be overcome by the benefits of optimized boundary layer ingestion aircraft configurations.

Bibliography

[1] Daggett, D. L., "Ultra Efficient Engine Technology Systems Integration and Environmental Assessment," *NASA Contractor Report*, No. NASA/CR-2002-211754, July 2002, Boeing Commercial Airplane Group, Seattle, Washington.

[2] Liebeck, R. H., "Design of the Blended Wing Body Subsonic Transport," *Journal of Aircraft*, AIAA, Vol. 41, No. 1, January-February 2004.

[3] Velicki, A., Thrash, P., and Jegley, D., "Airframe Development for the Hybrid Wing Body Aircraft," *47th AIAA Aerospace Sciences Meeting including the New Horizons Forum and Aerospace Exposition*, No. AIAA 2009-0932, AIAA, Orlando, Florida, January 2009.

[4] Greitzer, E., Bonnefoy, P., De la Rosa Blanco, E., Dorbian, C., Drela, M., Hall, D., Hansman, R., Hileman, J., Liebeck, R., Lovegren, J., Mody, P., Pertuze, J., Sato, S., Spakovszky, Z., Tan, C., Hollman, J., Duda, J., Fitzgerald, N., Houghton, J., Kerrebrock, J., Kiwada, G., Kordonowy, D., Parrish, J., Tylko, J., Wen, E., and Lord, W., "N+3 Aircraft Concept Designs and Trade Studies, Final Report, Volume 1," *NASA Contractor Report*, No. NASA/CR-2010-216794/VOL1, December 2010.

[5] Drela, M., "Development of the D8 Transport Configuration," *29th AIAA Applied Aerodynamics Conference*, No. AIAA 2011-3970, AIAA, Honolulu, Hawaii, June 2011.

[6] Gatlin, G. M., Vicroy, D. D., and Carter, M. B., "Experimental Investigation of the Low-Speed Aerodynamic Characteristics of a 5.8-Percent Scale Hybrid Wing Body Configuration," *30th AIAA Applied Aerodynamics Conference*, No. AIAA 2012-2669, AIAA, New Orleans, Louisiana, June 2012.

[7] Pandya, S. A., "External Aerodynamics Simulations for the MIT D8 'Double-Bubble' Aircraft Design," *7th International Conference on Computational Fluid Dynamics*, No. ICCFD7-4304, ICCFD7, Big Island, Hawaii, July 2012.

[8] Hooker, J. R. and Wick, A., "Design of the Hybrid Wing Body for Fuel Efficient Air Mobility Operations," *52nd Aerospace Sciences Meeting*, No. AIAA 2014-1285, AIAA, National Harbor, Maryland, January 2014.

[9] Flamm, J. D., James, K. D., and Bonet, J. T., "Overview of ERA Integrated Technology Demonstration (ITD) 51A Ultra-High Bypass (UHB) Integration for Hybrid Wing Body," *54th Aerospace Sciences Meeting*, No. AIAA 2016-0007, AIAA, San Diego, California, January 2016.

Bibliography

[10] Welstead, J. R., and Felder, J. L., "Conceptual Design of a Single-Aisle Turboelectric Commercial Transport with Fuselage Boundary Layer Ingestion" *54th Aerospace Sciences Meeting*, No. AIAA 2016-1027, AIAA, San Diego, California, January 2016.

[11] Yutko, B., Titchener, N., Courtin, C., Lieu, M., Wirsing, L., Tylko, J., Chambers, J., Roberts, T., and Church, C., "Conceptual Design of a D8 Commercial Aircraft," *17th AIAA Aviation Technology, Integration, and Operations Conference*, No. AIAA 2017-3590, AIAA, Denver, Colorado, June 2017.

[12] Smith, L. H., "Wake Ingestion Propulsion Benefit," *Journal of Propulsion and Power*, AIAA, Vol. 9, No. 1, January-February 1993.

[13] Daggett, D. L., Kawai, R., and Friedman, D., "Blended Wing Body Systems Studies: Boundary Layer Ingestion Inlets with Active Flow Control," *NASA Contractor Report*, No. NASA/CR-2003-212670, December 2003.

[14] Kawai, R. T., Friedman, D. M., and Serrano, L., "Blended Wing Body (BWB) Boundary Layer Ingestion (BLI) Inlet Configuration and System Studies," *NASA Contractor Report*, No. NASA/CR-2006-214534, December 2006, Boeing Phantom Works, Huntington Beach, California.

[15] Thomas, R. H., Burley, C. L., and Olson, E. D., "Hybrid Wing Body Aircraft System Noise Assessment with Propulsion Airframe Aeroacoustic Experiments," *16th AIAA/CEAS Aeroacoustics Conference*, No. AIAA 2010-3913, AIAA, June 2010.

[16] Collier, F., Thomas, R., Burley, C., Nickol, C., Lee, C., and Tong, M., "Environmentally Responsible Aviation – Real Solutions for Environmental Challenges Facing Aviation," *27th International Congress of the Aeronautical Sciences*, No. ICAS 2010-1.6.1, ICAS, Nice, France, September 2010.

[17] Hardin, L. W., Tillman, G., Sharma, O. P., Berton, J., and Arend, D. J., "Aircraft System Study of Boundary Layer Ingesting Propulsion," *48th AIAA/ASME/SAE/ASEE Joint Propulsion Conference & Exhibit*, No. AIAA 2012-3993, AIAA, Atlanta, Georgia, August 2012.

[18] Thomas, R. H., Czech, M. J., and Doty, M. J., "High Bypass Ratio Jet Noise Reduction and Installation Effects Including Shielding Effectiveness," *51st AIAA Aerospace Sciences Meeting including the New Horizons Forum and Aerospace Exposition*, No. AIAA 2013-0541, AIAA, Grapevine, Texas, January 2013.

[19] Uranga, A. Drela, M., Greitze, E. M., Titchener, N. A., Lieu, M. K., Siu, N. M., Huang, A. C., Gatlin, G. M., and Hannon, J. A., "Preliminary Experimental Assessment of the Boundary Layer Ingestion Benefit for the D8 Aircraft," *52nd Aerospace Sciences Meeting*, No. AIAA 2014-0906, AIAA, National Harbor, Maryland, January 2014.

[20] Sabo, K. and Drela, M., "Benefits of Boundary Layer Ingestion Propulsion," *53rd Aerospace Sciences Meeting*, No. AIAA 2015-1667, AIAA, Kissimmee, Florida, January 2015.

[21] Hall, D. K., Huang, A. C., Uranga, A., Greitzer, E. M., Drela, M., and Sato, S., "Boundary Layer Ingestion Propulsion Benefit for Transport Aircraft," *Journal of Propulsion and Power*, AIAA, Vol. 33, No. 5, September-October 2017.

[22] Uranga, A., Drela, M., Hall, D. K., and Greitzer, E. M., "Analysis of the Aerodynamic Benefit from Boundary Layer Ingestion for Transport Aircraft," *AIAA Journal*, AIAA, Vol. 56, No. 11, November 2018.

[23] Pazur, W. and Fottner, L., "The Influence of Inlet Swirl Distortions on the Performance of a Jet Propulsion Two-Stage Axial Compressor," *Journal of Turbomachinery*, ASME, Vol. 113, April 1991.

[24] Hamed, A. and Numbers, K., "Inlet Distortion Considerations for High Cycle Fatigue in Gas Turbine Engine," *33rd Joint Propulsion Conference and Exhibit*, No. AIAA 1997-3364, AIAA, Seattle, Washington, June 1997.

[25] Cousins, W. T., "History, Philosophy, Physics, and Future Directions of Aircraft Propulsion System/Inlet Integration," *Proceedings of ASME Turbo Expo 2004: Power for Land, Sea, and Air*, No. GT2004-54210, ASME, Vienna, Austria, June 2004.

[26] Kurzke, J., "Effects of Inlet Flow Distortion on the Performance of Aircraft Gas Turbines," *Proceedings of ASME Turbo Expo 2006: Power for Land, Sea, and Air*, No. GT2006-90419, ASME, Barcelona, Spain, May 2006.

[27] Plas, A. P., Sargeant, M. A., Madani, V., Crichton, D., Greitzer, E. M., Hynes, T. P., and Hall, C. A., "Performance of Boundary Layer Ingesting (BLI) Propulsion System," *45th AIAA Aerospace Sciences Meeting and Exhibit*, No. AIAA 2007-0450, AIAA, Reno, Nevada, January 2007.

[28] Davis, M. and Hale, A., "A Parametric Study on the Effects of Inlet Swirl on Compression System Performance and Operability using Numerical Simulations," *Proceedings of ASME Turbo Expo 2007: Power for Land, Sea, and Air*, No. GT2007-27033, ASME, Montreal, Canada, May 2007.

[29] Sheoran, Y., Bouldin, B., and Krishnan, P. M., "Compressor Performance and Operability in Swirl Distortion," *Journal of Turbomachinery*, ASME, Vol. 134, July 2012.

[30] Choi, M., Vahdati, M., and Imregun, M., "Effects of Fan Speed on Rotating Stall Inception and Recovery," *Journal of Turbomachinery*, ASME, Vol. 133, October 2011.

[31] Bakhle, M. A., Reddy, T. S. R., Herrick, G. P., Shabbir, A., and Florea, R. V., "Aeromechanics Analysis of a Boundary Layer Ingesting Fan," *48th AIAA/ASME/SAE/ASEE Joint Propulsion Conference & Exhibit*, No. AIAA 2012-3995, AIAA, Atlanta, Georgia, August 2012.

[32] Arend, D. J., Tillman, G., and O'Brien, W. F., "Generation After Next Propulsor Research: Robust Design for Embedded Engine Systems," *48th AIAA/ASME/SAE/ASEE Joint Propulsion Conference & Exhibit*, No. AIAA 2012-4041, AIAA, Atlanta, Georgia, August 2012.

[33] Ferrar, A. M., and O'Brien, W. F., "Progress in Boundary Layer Ingesting Embedded Engine Research," *48th AIAA/ASME/SAE/ASEE Joint Propulsion Conference & Exhibit*, No. AIAA 2012-4283, AIAA, Atlanta, Georgia, August 2012.

[34] Bakhle, M. A., Reddy, T. S. R., Herrick, G. P., Shabbir, A., and Florea, R. V., "Aeromechanics Analysis of a Boundary Layer Ingesting Fan," *NASA Technical Memorandum*, No. NASA/TM-2013-217730, January 2013.

[35] Lucas, J. R., "Effect of BLI-Type Inlet Distortion on Turbofan Engine Performance," M.S. Thesis, Mechanical Engineering Department, Virginia Polytechnic Institute and State University, June 2013.

[36] Gunn, E. J., Tooze, S. E., Hall, C. A., and Colin, Y., "An Experimental Study of Loss Sources in a Fan Operating with Continuous Inlet Stagnation Pressure Distortion," *Journal of Turbomachinery*, ASME, Vol. 135, September 2013.

[37] Pardo, A. C., Mehdi, A., Pachidis, V., and MacManus D. G., "Numerical Study of the Effect of Multiple Tightly-Wound Vortices on a Transonic Fan Stage Performance," *Proceedings of ASME Turbo Expo 2014: Turbine Technical Conference and Exposition*, No. GT2014-26481, ASME, Düsseldorf, Germany, June 2014.

[38] Lucas, J. R., O'Brien, W. F., and Ferrar, A. M., "Effect of BLI-Type Inlet Distortion on Turbofan Engine Performance," *Proceedings of ASME Turbo Expo 2014: Turbine Technical Conference and Exposition*, No. GT2014-26666, ASME, Dusseldorf, Germany, June 2014.

[39] Perovic, D., Hall, C. A., and Gunn, E. J., "Stall Inception in a Boundary Layer Ingestion Fan," *Proceedings of ASME Turbo Expo 2015: Turbine Technical Conference and Exposition*, No. GT2015-43025, ASME, Montreal, Canada, June 2015.

[40] Lord, W. K., Hendricks, G. J., Kirby, M. J., Ochs, S. S., Lin, R., and Hardin, L., "Impact of Ultra High Bypass/Hybrid Wing Body Integration of Propulsion System Performance and Operability," *54th AIAA Aerospace Sciences Meeting*, No. AIAA 2016-0267, AIAA, San Diego, California, January 2016.

[41] Min, J. B., Reddy, T. S. R., Bakhle, M. A., Coroneos, R. M., Stefko, G. L., Provenza, A. J., and Duffy, K. P., "Cyclic Symmetry Finite Element Forced Response Analysis of a Distortion-Tolerant Fan with Boundary Layer Ingestion," *2018 AIAA Aerospace Sciences Meeting*, No. AIAA 2018-1890, AIAA, Kissimmee, Florida, January 2018.

[42] Bakhle, M. A, Reddy, T. S. R., Coroneos, R. M., Min, J. B., Provenza, A. J., Duffy, K. P., Stefko, G. L., and Heinlein, G. S., "Aeromechanics Analysis of a Distortion-Tolerant Fan with Boundary Layer Ingestion," *2018 AIAA Aerospace Sciences Meeting*, No. AIAA 2018-1891, AIAA, Kissimmee, Florida, January 2018.

[43] Provenza, A. J., Duffy, K. P., and Bakhle, M. A., "Aeromechanical Response of a Distortion Tolerant Boundary Layer Ingesting Fan," *Proceedings of ASME Turbo Expo 2018: Turbomachinery Technical Conference and Exposition*, No. GT2018-77094, ASME, Oslo, Norway, June 2018.

[44] Rannie, W. D. and Marble, F. E., "Unsteady Flows in Axial Turbomachines," Office of Naval Research, 1957.

[45] Wadia, A. R., Yao, J., and Gorrell, S. E., "Numerical Investigation of Inlet Distortion Induced Swirl in Multistage Fans," *26th International Congress of the Aeronautical Sciences*, ICAS, Anchorage, Alaska, September 2008.

[46] Davis, M. W., Hale, A. A., Vining, C., and Cousins, W. T., "Application of Numerical Analysis Tools for Airframe-Propulsion Integrated Test and Evaluation," *Proceedings of ASME Turbo Expo 2008: Power for Land, Sea, and Air*, No. GT2008-50194, ASME, Berlin, Germany, June 2008.

[47] Chima, R. V., Arend, D. J., Castner, R. S., Slater, J. W., and Truax, P. P., "CFD Models of a Serpentine Inlet, Fan, and Nozzle," *48th AIAA Aerospace Sciences Meeting including the New Horizons Forum and Aerospace Exposition*, No. AIAA 2010-0033, AIAA, Orlando, Florida, January 2010.

[48] Sanders, D. D. and List, M. G., "CFD Performance Predictions of a Serpentine Diffuser Configuration in an Annular Cascade Facility," *51st AIAA Aerospace Sciences Meeting including the New Horizons Forum and Aerospace Exposition*, No. AIAA 2013-0220, AIAA, Grapevine, Texas, January 2013.

[49] Florea, R. V., Voytovych, D., Tillman, G., Stucky, M., Shabbir, A., Sharma, O., and Arend, D., "Aerodynamic Analysis of Boundary-Layer-Ingesting Distortion-Tolerant Fan," *Proceedings of ASME Turbo Expo 2013: Turbine Technical Conference and Exposition*, No. GT2013-94656, ASME, San Antonio, Texas, USA, June 2013.

[50] Ochs, S. S., Tilman, G., Joo, J., Voytovych, D. M., "CFD-based Analysis of Boundary Layer Ingesting Propulsion," *51st AIAA/SAE/ASEE Joint Propulsion Conference*, No. AIAA 2015-3800, AIAA, Orlando, Florida, July 2015.

[51] Ochs, S. S., Tilman, G., Joo, J., Voytovych, D. M., "Computational Fluid Dynamics-Based Analysis of Boundary Layer Ingesting Propulsion," *Journal of Propulsion and Power*, AIAA, Vol. 33, No. 2, March-April 2017.

[52] Cousins, W. T., Voytovych, D., Tilman, G., and Gray, E., "Design of a Distortion-Tolerant Fan for a Boundary-Layer Ingesting Embedded Engine Application," *53rd AIAA/SAE/ASEE Joint Propulsion Conference*, No. AIAA 2017-5042, AIAA, Atlanta, Georgia, July 2017.

[53] Arend, D. J., Castner, R. S., and Frate, F. C., "A Low Cost, Compact and Versatile Rig for Integrated Inlet and Propulsion Systems Research," *44th AIAA Aerospace Sciences Meeting and Exhibit*, No. AIAA 2006-1313, AIAA, Reno, Nevada, January 2006.

[54] Ferrar, A. M., "Measurements of Flow in Boundary Layer Ingesting Serpentine Inlets," M.S. Thesis, Mechanical Engineering Department, Virginia Polytechnic Institute and State University, 2011.

[55] Nessler, C. A., Copenhaver, W. W., and List, M. G., "Serpentine Diffuser Performance with Emphasis on Future Introduction to a Transonic Fan," *51st AIAA Aerospace Sciences Meeting including the New Horizons Forum and Aerospace Exposition*, No. AIAA 2013-1133, AIAA, Grapevine, Texas, January 2013.

[56] Zachos, P. K., MacManus, D. G., Prieto, D. G., and Chiereghin, N., "Flow Distortion Measurements in Convoluted Aeroengine Intakes," *AIAA Journal*, AIAA, Vol. 54, No. 9, September 2016.

[57] Arend, D. J., Wolter, J. D., Hirt, S. M., Provenza, A. J., Gazzaniga, J. A., Cousins, W. T., Hardin, L. W., and Sharma, O. P., "Experimental Evaluation of an Embedded Boundary Layer Ingesting Propulsor for Highly Efficient Subsonic Cruise Aircraft," *53rd AIAA/SAE/ASEE Joint Propulsion Conference*, No. AIAA 2017-5041, AIAA, Atlanta, Georgia, July 2017.

[58] Hirt, S. M., Arend, D. J., Wolter, J. D., and Johnson, A., "Development of a Flow Field for Testing a Boundary-Layer-Ingesting Propulsor," *53rd AIAA/SAE/ASEE Joint Propulsion Conference*, No. AIAA 2017-5043, AIAA, Atlanta, Georgia, July 2017.

[59] Ferrar, A. M. and O'Brien, W. F., "Fan Response to Total Pressure Distortions Produced by Boundary Layer Ingesting Serpentine Inlets," *48th AIAA/ASME/SAE/ASEE Joint Propulsion Conference & Exhibit*, No. AIAA 2012-3996, AIAA, Atlanta, Georgia, August 2012.

[60] Bailey, J. M., and O'Brien, W. F., "The Influence of Duct Development Distance on Screen Generated Total Pressure Distortion Profiles," *49th AIAA/ASME/SAE/ASEE Joint Propulsion Conference*, No. AIAA 2013-3602, AIAA, San Jose, California, July 2013.

[61] Bailey, J. M., "The Influence of Development and Fan/Screen Interaction on Screen-Generated Total Pressure Distortion Profiles," M.S. Thesis, Mechanical Engineering Department, Virginia Polytechnic Institute and State University, December 2013.

[62] Ferrar, A. M., "Measurement and Uncertainty Analysis of Transonic Fan Response to Total Pressure Inlet Distortion," Ph.D. Dissertation, Mechanical Engineering Department, Virginia Polytechnic Institute and State University, February 2015.

[63] Bailey, J. M., "Full Scale Experimental Transonic Fan Interactions with a Boundary Layer Ingesting Total Pressure Distortion," Ph.D. Dissertation, Mechanical Engineering Department, Virginia Polytechnic Institute and State University, November 2016.

[64] Ferrar, A. M., Schneck, W. C., Bailey, J. M., Hoopes, K. M., and O'Brien, W. F., "Application of Additive Manufacturing to Rapidly Produce High-Resolution Total Pressure Distortion Screens," *50th AIAA Aerospace Sciences Meeting including the New Horizons Forum and Aerospace Exposition*, No. AIAA 2012-0929, AIAA, Nashville, Tennessee, January 2012.

[65] Gunn, E. J. and Hall, C. A., "Aerodynamics of Boundary Layer Ingesting Fans," *Proceedings of ASME Turbo Expo 2014: Turbine Technical Conference and Exposition*, No. GT2014-26142, ASME, Düsseldorf, Germany, June 2014.

[66] Beale, D. K., Cramer, K. B., and King, P. S., "Development of Improved Methods for Simulating Aircraft Inlet Distortion in Turbine Engine Ground Tests," *22nd AIAA Aerodynamic Measurement Technology and Ground Testing Conference*, No. AIAA 2002-3045, AIAA, St. Louis, Missouri, June 2002.

[67] Beale, D., Davis, M., and Sirbaugh, J., "Requirements and Advances in Simulating Aircraft Inlet Total-Pressure Distortion in Turbine Engine Ground Tests," *Proceedings of ASME Turbo Expo 2006: Power for Land, Sea, and Air*, No. GT2006-90038, ASME, Barcelona, Spain, May 2006.

[68] Beale, D., Wieland, S., Reed, J., and Wilhite, L., "Demonstration of a Transient Total-Pressure Distortion Generator for Simulating Aircraft Inlet Distortion in Turbine Engine Ground Tests," *Proceedings of ASME Turbo Expo 2007: Power for Land, Sea, and Air*, No. GT2007-27222, ASME, Montreal, Canada, May 2007.

[69] Genssler, H. P., Meyer, W., and Fottner, L., "Development of Intake Swirl Generators for Turbo Jet Engine Testing," *66th Propulsion and Energetics Specialists' Meeting*, No. AD-P005 473, DTIC, Munich, Germany, September 1986

[70] Beale, D., "Demonstration of a Remotely-Controlled Swirl Generator for Simulating Aircraft Inlet Secondary Flows during Turbine Engine Ground Tests," *Proceedings of ASME Turbo Expo 2018: Turbomachinery Technical Conference and Exposition*, No. GT2018-75749, ASME, Oslo, Norway, June 2018.

[71] Davis, M., Beale, D., and Sheoran, Y., "Integrated Test and Evaluation Techniques as Applied to an Inlet Swirl Investigation Using the F109 Gas Turbine Engine," *Proceedings of ASME Turbo Expo 2008: Power for Land, Sea, and Air*, No. GT2008-50074, ASME, Berlin, Germany, June 2008.

[72] Sheoran, Y. and Bouldin, B., "A Versatile Design of a Controlled Swirl Distortion Generator for Testing Gas Turbine Engines," *Proceedings of ASME Turbo Expo 2008: Power for Land, Sea, and Air*, No. GT2008-50657, ASME, Berlin, Germany, June 2008.

[73] Sheoran, Y., Bouldin, B., and Krishnan, P. M., "Advancements in the Design of an Adaptable Swirl Distortion Generator for Testing Gas Turbine Engines," *Proceedings of ASME Turbo Expo 2009: Power for Land, Sea, and Air*, No. GT2009-59172, ASME, Orlando, Florida, USA, June 2009.

[74] Sheoran, Y., Bouldin, B., and Krishnan, P. M., "Compressor Performance and Operability in Swirl Distortion," *Proceedings of ASME Turbo Expo 2010: Power for Land, Sea, and Air*, No. GT2010-22777, ASME, Glasgow, United Kingdom, June 2010.

[75] Hoopes, K. M. and O'Brien, W. F., "The StreamVane© Method: A New Way to Generate Swirl Distortion for Jet Engine Research," *49th AIAA/ASME/SAE/ASEE Joint Propulsion Conference*, No. AIAA 2013-3665, AIAA, San Jose, California, July 2013.

[76] Hoopes, K. M., "A New Method for Generating Swirl Inlet Distortion for Jet Engine Research," M.S. Thesis, Mechanical Engineering Department, Virginia Polytechnic Institute and State University, May 2013.

[77] Nelson, M. A., Lowe, K. T., O'Brien, W. F., Kirk, C., and Hoopes, K. M., "Stereoscopic PIV Measurements of Swirl Distortion on a Full-Scale Turbofan Engine Inlet," *52nd Aerospace Sciences Meeting*, No. AIAA 2014-0533, AIAA, National Harbor, Maryland, January 2014.

[78] Guimarães, T., Lowe, K. T., and O'Brien, W., "An Overview of Recent Results Using the StreamVane™ Method for Generating Tailored Swirl Distortion in Jet Engine Research," *54th AIAA Aerospace Sciences Meeting*, No. AIAA 2016-0534, AIAA, San Diego, California, January 2016.

[79] Frohnapfel, D. J., "Experimental Investigation of Fan Rotor Response to Inlet Swirl Distortion," M.S. Thesis, Mechanical Engineering Department, Virginia Polytechnic Institute and State University, April 2016.

[80] Sanders, D. D., Nessler, C. A., Copenhaver, W. W., List, M. G., and Janczewski, T. J., "Computational and Experimental Evaluation of a Complex Inlet Swirl Pattern Generation System," *52nd AIAA/SAE/ASEE Joint Propulsion Conference*, No. AIAA 2015-5008, AIAA, Salt lake City, Utah, July 2016.

[81] Nessler, C. A., Sanders, D. D., List, M. G., Janczewski, T. J., and Copenhaver, W. W., "Axial Extent of Flowfield Variation from the StreamVane™ Swirl Pattern Generation System," *55th AIAA Aerospace Sciences Meeting*, No. AIAA 2017-1621, AIAA, Grapevine, Texas, January 2017.

[82] Frohnapfel, D. J., O'Brien, W. F., and Lowe, K. T., "Fan Rotor Flow Measurements in a Turbofan Engine Operating with Inlet Swirl Distortion," *55th AIAA Aerospace Sciences Meeting*, No. AIAA 2017-1623, AIAA, Grapevine, Texas, January 2017.

[83] Frohnapfel, D. J., O'Brien, W. F., and Lowe, K. T., "Experimental Quantification of Fan Rotor Effects on Inlet Swirl Using Swirl Distortion Descriptors," *Proceedings of ASME Turbo Expo 2017: Turbomachinery Technical Conference and Exposition*, No. GT2017-64779, ASME, Charlotte, North Carolina, USA, June 2017.

[84] Gillaugh, D. L., Copenhaver, W. W., Janczewski, T., Holycross, C., Sanders, D. D., and Nessler, D., "Aeromechanical Evaluation of an FDM Printed Thermoplastic StreamVane™," *53rd AIAA/SAE/ASEE Joint Propulsion Conference*, No. AIAA 2017-4600, AIAA, Atlanta, Georgia, July 2017.

[85] Guimarães, T., Frohnapfel, D. J., Lowe, K. T., and O'Brien, W. F., "Streamwise Development and Turbulence Characterization of a Twin-Vortex Inlet Distortion for Turbofan Applications," *53rd AIAA/SAE/ASEE Joint Propulsion Conference*, No. AIAA 2017-4992, AIAA, Atlanta, Georgia, July 2017.

[86] Smith, K. N., O'Brien, W. F., and Lowe, K. T., "Analysis of Duct Vortex Development with Low- and High-fidelity Models to Support StreamVane Design," *2018 AIAA Aerospace Sciences Meeting*, No. AIAA 2018-1558, AIAA, Kissimmee, Florida, January 2018.

[87] Guimarães, T., Lowe, K. T., and O'Brien, W. F., "StreamVane Turbofan Inlet Swirl Distortion Generator: Mean Flow and Turbulence Structure," *Journal of Propulsion and Power*, AIAA, Vol. 34, No. 2, March-April 2018.

[88] Frohnapfel, D. J., Mack, E. Untaroiu, A., O'Brien, W. F., and Lowe, K. T., "Turbofan Nose Cone Interactions with Inlet Swirl," *Proceedings of ASME Turbo Expo 2018: Turbomachinery Technical Conference and Exposition*, No. GT2018-76616, ASME, Oslo, Norway, June 2018.

[89] Coffman, J. and Nessler, C. A., "Center Body Influences on the AIP and Secondary Flows," *2018 Joint Propulsion Conference*, No. AIAA 2018-4748, AIAA, Cincinnati, Ohio, July 2018.

[90] Frohnapfel, D. J., O'Brien, W. F., and Lowe, K. T., "Experimental Quantification of Fan Rotor Effects on Inlet Swirl Using Swirl Distortion Descriptors," *Journal of Engineering for Gas Turbines and Power*, ASME, Vol. 140, August 2018.

[91] Guimarães, T., Lowe, K. T., and O'Brien, W. F., "Complex Flow Generation and Development in a Full-Scale Turbofan Inlet," *Journal of Engineering for Gas Turbines and Power*, ASME, Vol. 140, August 2018.

[92] Wellborn, S. R., Reichert, B. A., and Okiishi, T. H., "An Experimental Investigation of the Flow in a Diffusing S-Duct," *NASA Technical Memorandum*, No. NASA/TM-1992-105809, July 1992.

[93] Wellborn, S. R., Okiishi, T. H., and Reichert, B. A., "A Study of the Compressible Flow Through a Diffusing S-Duct," *NASA Technical Memorandum*, No. NASA/TM-1993-106411, December 1993.

[94] Wellborn, S. R., Reichert, B. A., and Okiishi, T. H., "Study of the Compressible Flow in a Diffusing S-Duct," *Journal of Propulsion and Power*, AIAA, Vol. 10, No. 5, September-October 1994.

[95] Anabtawi, A. J., Blackwelder, R., Liebeck, R., and Lissaman, R., "Experimental Investigation of Boundary Layer Ingesting Diffusers of a Semi-Circular Cross Section," *36th AIAA Aerospace Sciences Meeting and Exhibit*, No. AIAA 1998-0945, AIAA, Reno, Nevada, January 1998.

[96] Anabtawi, A. J., Blackwelder, R. F., Lissaman, R. H., and Liebeck, R. H., "An Experimental Investigation of Boundary Layer Ingestion in a Diffusing S-Duct With and Without Passive Flow Control," *37th AIAA Aerospace Sciences Meeting and Exhibit*, No. AIAA 1999-0739, AIAA, Reno, Nevada, January 1999.

[97] Berrier, B. L. and Morehouse, M. B., "Evaluation of Flush-Mounted, S-Duct Inlets with Large Amounts of Boundary Layer Ingestion," *Applied Vehicle Technology (AVT) Panel Meeting*, No. 38, NATO, Warsaw, Poland, October 2003.

[98] Gorton, S. A., Owens, R. L., Jenkins, L. N., Allan, B. G., and Schuster, E. P., "Active Flow Control on a Boundary-Layer-Ingesting Inlet," *42nd AIAA Aerospace Sciences Meeting and Exhibit*, No. AIAA 2004-1203, AIAA, Reno, Nevada, January 2004.

[99] Berrier, B. L., Carter, M. B., and Allan, B. G., "High Reynolds Number Investigation of a Flush-Mounted, S-Duct Inlet with Large Amounts of Boundary Layer Ingestion," *NASA Technical Publication*, No. NASA/TP-2005-213766, September 2005.

[100] Owens, L. R., Allen, B. G., and Gorton, S. A., "Boundary-Layer-Ingesting Inlet Flow Control," *44th AIAA Aerospace Sciences Meeting and Exhibit*, No. AIAA 2006-0839, AIAA, Reno, Nevada, January 2006.

[101] Allan, B. G., and Owens, L. R., "Numerical Modeling of Flow Control in a Boundary-Layer-Ingesting Offset Inlet Diffuser at Transonic Mach Numbers," *44th AIAA Aerospace Sciences Meeting and Exhibit*, No. AIAA 2006-0845, AIAA, Reno, Nevada, January 2006.

[102] Owens, L. R., Allan, B. G., Gorton, S. A., "Boundary-Layer-Ingesting Inlet Flow Control," *Journal of Aircraft*, AIAA, Vol. 45, No. 4, July-August 2008.

[103] Webster, R. S., Sreenivas, K., Hyams, D. G., Hilbert, C. B., Briley, W. R., and Whitfield, D. L., "Demonstration of Sub-system Level Simulations: A Coupled Inlet and Turbofan Stage," *48th AIAA/ASME/SAE/ASEE Joint Propulsion Conference*, No. AIAA 2012-4282, AIAA, Atlanta, Georgia, August 2012.

[104] Davis, Z. S. and Park, M. A., "IFCPT S-Duct Grid-Adapted FUN3D Computations for the Third Propulsion Aerodynamics Workshop," *53rd AIAA/SAE/ASEE Joint Propulsion Conference*, No. AIAA 2007-48356, AIAA, Atlanta, Georgia, July 2017.

[105] "Gas Turbine Engine Inlet Flow Distortion Guidelines," Aerospace Recommended Practice, SAE ARP1420, SAE Aerospace, January 2001.

[106] "A Methodology for Assessing Inlet Swirl Distortion," Aerospace Information Report, SAE AIR5686, SAE Aerospace, November 2010.

[107] Guimarães, T., Schneck, W. C., Lowe, K. T., O'Brien, W. F., and Copenhaver, W. W., "Swirling Flow Evolution Part 1: Design and Stereo PIV Measurements at Select Planes," *55th AIAA Aerospace Sciences Meeting*, No. AIAA 2017-1620, AIAA, Grapevine, Texas, January 2017.

[108] Schneck, W. C., Guimarães, T., Frohnapfel, D. J., Lowe, K. T., O'Brien, W. F., and Copenhaver, W. W., "Swirling Flow Evolution Part 2: StreamFlow 2D+t Model Validated with Stereo PIV Measurements," *55th AIAA Aerospace Sciences Meeting*, No. AIAA 2017-1622, AIAA, Grapevine, Texas, January 2017.

[109] Green, D. W. and Perry, R. H., "Perry's Chemical Engineering Handbook," The McGraw-Hill Companies, Inc., Eighth Edition, New York, New York 2008.

[110] Mack, E. K., Gillespie, J., Frohnapfel, D. J., O'Brien, W. and Untaroiu, A., "Pressure Screen-StreamVane Interaction Effects on Downstream Flow Distortion Pattern," *2018 Joint Propulsion Conference*, No. AIAA 2018-4401, AIAA, Cincinnati, Ohio, July 2018.

[111] Treaster, A. L., and Yocum, A. M., "The Calibration and Application of Five-Hole Probes," *24th International Symposium*, No. TM 78-10, Albuquerque, New Mexico, January 1978.

[112] Hill, P. G. and Peterson, C. R., "Mechanics and Thermodynamics of Propulsion," Addison-Wesley Publishing Company, Inc., Second Edition, Reading, Massachusetts 1992.

[113] "Standard for Verification and Validation in Computational Fluid Dynamics and Heat Transfer," ASME V&V 20-2009, ASME, November 2009

[114] "ULTEM™ 9085 Production-Grade Thermoplastic for Fortus 3D Production Systems," Material Specification Sheet, Stratasys Inc., Eden Prairie, Minnesota 2008.

Appendix A – Computational Grid Refinement Study

A grid refinement study was conducted according to ASME standard practices [113] to determine the grid convergence index and estimate discretization error in the computational analysis of the isolated S-duct setup (Chapter 2). This particular case was selected for grid refinement due to the dependency of the CFD solution on the design and evaluation of the ScreenVane distortion device. In all other analyses, CFD was conducted on assumed refined grids based on the results of this study.

Overall, eleven boundary condition cases were analyzed on the isolated S-duct domain. Due to the desire to reduce workload, the grid refinement study was limited to three representative cases: Isolated S-Duct with 0% BLI, Isolated S-Duct with 25% BLI, and Isolated S-Duct with 50% BLI. It was assumed that analyzing the grid on the upper and lower limits of the case study would bound the error. Additionally, since 25% BLI was ultimately selected for ScreenVane design, confidence in the solution could be enhanced with documented grid convergence.

It was assumed that the resulting simulation series fell within the asymptotic solution region, therefore, three grids were created with varying levels of refinement. The refinement levels were based on a systematic adjustment of Element Size and Inflation Layer Thickness. Table A.1 summarizes mesh parameters for the three refinement levels used to prove grid convergence.

Table A.1: S-Duct CFD Grid Refinement Study – Mesh Parameters

Grid Level	3	2	1
Method	Unstructured Tetrahedrons		
Element Sizing	0.500 in	0.375 in	0.250 in
Growth Rate	1.10	1.10	1.10
Inflation, y+	Approx. 50	Approx. 38	Approx. 25
Inflation, First Layer Thickness	0.008 in	0.006 in	0.004 in
Inflation, Number of Layers	20	20	20
Inflation, Growth Rate	1.20	1.20	1.20
Nodes	Approx. 1.7M	Approx. 3.3M	Approx. 9.3M
Elements	Approx. 5.4M	Approx. 12.0M	Approx. 38.0M

Following the “Five-Step Procedure for Uncertainty Estimation”, the Grid Convergence Index (GCI) was estimated.

Step 1: Define a representative size for an unstructured grid.

$$h = \left[\frac{(\sum_{i=1}^{N} \Delta V_i)}{N}\right]^{\frac{1}{3}} \tag{A.1}$$

$where,$

$h\ is\ defined\ as\ the\ representative\ grid\ size$
$\Delta V_i\ is\ defined\ as\ the\ volume\ of\ the\ i^{th}\ element$
$N\ is\ defined\ as\ the\ number\ of\ elements$

Since identical geometry is used for each level of grid refinement, Equation A.1 can be simplified as follows.

$$h = \left[\frac{(V)}{N}\right]^{\frac{1}{3}} \tag{A.2}$$

$where,$

$V\ is\ defined\ as\ the\ volume\ of\ the\ domain$

Step 2: Calculate the grid refinement factor.

$$r = \frac{h_{coarse}}{h_{fine}} \tag{A.3}$$

$where,$

$r\ is\ defined\ as\ the\ grid\ refinement\ factor$
$h_{course}\ is\ the\ lower\ refined\ grid\ level\ size$
$h_{fine}\ is\ the\ higher\ refined\ grid\ level\ size$

Since representative grid size is never explicitly used, values were not calculated for reporting. Additionally, since identical geometry is used for each level of grid refinement, Equation A.3 can be simplified as follows.

$$r = \frac{N_{fine}}{N_{coarse}} \tag{A.4}$$

$where,$

$N_{fine}\ is\ the\ higher\ refined\ grid\ number\ of\ elements$
$N_{course}\ is\ the\ lower\ refined\ grid\ number\ of\ elements$

Step 3: Calculate the apparent order of the method.

$$p = \left[\frac{1}{\ln(r_{21})}\right]\left[\ln\left|\frac{\varepsilon_{32}}{\varepsilon_{21}}\right| + q(p)\right] \tag{A.5}$$

$$q(p) = \ln\left(\frac{r_{21}^{p} - s}{r_{32}^{p} - s}\right) \tag{A.6}$$

$$s = 1 \cdot sign\left(\frac{\varepsilon_{32}}{\varepsilon_{21}}\right) \tag{A.7}$$

$$\varepsilon_{32} = \varphi_3 - \varphi_2 \quad and \quad \varepsilon_{21} = \varphi_2 - \varphi_1 \tag{A.8}$$

$where,$

$p\ is\ defined\ as\ apparent\ order\ of\ the\ method\ and\ is\ iteratively\ solved$

$r_{21}\ is\ the\ grid\ refinement\ factor\ for\ medium\ and\ high\ grids$

$r_{32}\ is\ the\ grid\ refinement\ factor\ for\ low\ and\ medium\ grids$

$\varepsilon_{21}\ is\ the\ difference\ in\ paramter\ of\ interest\ for\ medium\ and\ high\ grids$

$\varepsilon_{32}\ is\ the\ difference\ in\ paramter\ of\ interest\ for\ low\ and\ medium\ grids$

$\varphi_3, \varphi_2, \varphi_1\ are\ defined\ as\ parameters\ or\ interest\ for\ each\ grid$

Step 4: Extrapolate to find "true" solution.

$$\varphi_{ext}^{21} = \frac{r_{21}^{p}\varphi_1 - \varphi_2}{r_{21}^{p} - 1} \tag{A.9}$$

$where,$

$\varphi_{ext}^{21}\ is\ defined\ as\ the\ extrapolated\ "true"\ solution$

Step 5: Calculate the estimated relative error, the estimated extrapolated relative error, and the grid convergence index. The grid convergence index may be reported as equivalent to numerical uncertainty.

$$e_a^{21} = \left|\frac{\varphi_1 - \varphi_2}{\varphi_1}\right| \tag{A.10}$$

$$e_{ext}^{21} = \left|\frac{\varphi_{ext}^{21} - \varphi_1}{\varphi_{ext}^{21}}\right| \tag{A.11}$$

$$GCI_{fine}^{21} = \frac{Fs \cdot e_a^{21}}{r_{21}^{p} - 1}$$

$where,$

$e_a^{21}\ is\ defined\ as\ the\ estimated\ relative\ error$

$e_{ext}^{21}\ is\ defined\ as\ the\ estimated\ extrapolated\ relative\ error$

$GCI_{fine}^{21}\ is\ defined\ as\ the\ grid\ convergence\ index$

$Fs\ is\ defined\ as\ the\ Factor\ of\ Safety$

For the current investigation, critical parameters of total pressure, static pressure, Mach number, and velocity magnitude were selected to be used in the grid refinement study. Area weighted average values were extracted at the AIP as the parameters of interest in Step 3. The results of the grid refinement study are summarized in Table A.2, Table A.3, and Table A.4 for inlet BLI heights of 0%, 25%, and 50%, respectively.

Table A.2: S-Duct CFD Grid Refinement Study – 0% BLI Discretization Error

	P_0 $[psia]$	P $[psia]$	M	$C_{r\theta z}$ $[ft/s]$
N_3	5413733			
N_2	11956788			
N_1	380008318			
r_{32}	1.3023			
r_{21}	1.4704			
φ_3	14.3250 [psia]	13.7225 [psia]	0.245295	272.1570 [ft/s]
φ_2	14.3244 [psia]	13.7217 [psia]	0.245285	272.1440 [ft/s]
φ_1	14.3230 [psia]	13.7197 [psia]	0.245329	272.1890 [ft/s]
p	1.0435	1.1956	3.1224	2.6382
φ_{ext}^{21}	14.3200 [psia]	13.7160 [psia]	0.245350	272.2100 [ft/s]
e_a^{21}	$9.7745\text{x}10^{-3}$ [%]	$1.4578\text{x}10^{-2}$ [%]	$1.7935\text{x}10^{-2}$ [%]	$1.6533\text{x}10^{-2}$ [%]
e_{ext}^{21}	$1.9743\text{x}10^{-2}$ [%]	$2.4904\text{x}10^{-2}$ [%]	$7.6890\text{x}10^{-3}$ [%]	$9.3663\text{x}10^{-3}$ [%]
GCI_{fine}^{21}	$2.4673\text{x}10^{-2}$ [%]	$3.1122\text{x}10^{-2}$ [%]	$9.6120\text{x}10^{-3}$ [%]	$1.1709\text{x}10^{-2}$ [%]

Table A.3: S-Duct CFD Grid Refinement Study – 25% BLI Discretization Error

	P_0 $[psia]$	P $[psia]$	M	$C_{r\theta z}$ $[ft/s]$
N_3	5413733			
N_2	11956788			
N_1	380008318			
r_{32}	1.3023			
r_{21}	1.4704			
φ_3	14.3233 [psia]	13.6862 [psia]	0.246257	272.9980 [ft/s]
φ_2	14.3230 [psia]	13.6861 [psia]	0.246237	272.9760 [ft/s]
φ_1	14.3231 [psia]	13.6860 [psia]	0.246239	272.9780 [ft/s]
p	3.76465	1.1782	8.4760	8.8527
φ_{ext}^{21}	14.3230 [psia]	13.6860 [psia]	0.246240	272.9800 [ft/s]
e_a^{21}	$6.9817\text{x}10^{-4}$ [%]	$7.3067\text{x}10^{-4}$ [%]	$8.1222\text{x}10^{-4}$ [%]	$7.3266\text{x}10^{-4}$ [%]
e_{ext}^{21}	$2.1361\text{x}10^{-4}$ [%]	$1.2710\text{x}10^{-3}$ [%]	$3.2172\text{x}10^{-5}$ [%]	$2.4964\text{x}10^{-5}$ [%]
GCI_{fine}^{21}	$2.6701\text{x}10^{-4}$ [%]	$1.5887\text{x}10^{-3}$ [%]	$4.0215\text{x}10^{-5}$ [%]	$3.1205\text{x}10^{-5}$ [%]

Table A.4: S-Duct CFD Grid Refinement Study – 50% BLI Discretization Error

	P_0 $[psia]$	P $[psia]$	M	$C_{r\theta z}$ $[ft/s]$
N_3	5413733			
N_2	11956788			
N_1	380008318			
r_{32}	1.3023			
r_{21}	1.4704			
φ_3	14.3316 [psia]	13.6832 [psia]	0.246537	273.2270 [ft/s]
φ_2	14.3313 [psia]	13.6831 [psia]	0.246516	273.2050 [ft/s]
φ_1	14.3312 [psia]	13.6830 [psia]	0.246519	273.2080 [ft/s]
p	4.7674	1.1782	7.0634	7.2477
φ_{ext}^{21}	14.3310 [psia]	13.6830 [psia]	0.246520	273.210 [ft/s]
e_a^{21}	6.9778×10^{-4} [%]	7.3083×10^{-4} [%]	1.2169×10^{-3} [%]	1.0981×10^{-3} [%]
e_{ext}^{21}	1.3208×10^{-4} [%]	1.2712×10^{-3} [%]	8.5547×10^{-5} [%]	7.1552×10^{-5} [%]
GCI_{fine}^{21}	1.6510×10^{-4} [%]	1.5890×10^{-3} [%]	1.0693×10^{-4} [%]	8.9440×10^{-5} [%]

From the results of the grid refinement study, it was determined that the final mesh was sufficiently refined. Discretization error for the parameters of interest was calculated at less than 0.05% for all cases analyzed.

Appendix B – ScreenVane Stress Analysis

A computational stress analysis was performed on the StreamVane component of the ScreenVane distortion generator. This analysis was critical to prove structural integrity of the device prior to manufacture and installation in the turbofan engine inlet flowpath, as failure of the device could result in catastrophic damage to the turbofan engine.

Four loading conditions were assumed, ScreenVane as Designed and StreamVane Component Only in both the isolated and coupled computational domains. The ScreenVane as Designed cases utilized the CFD analysis conducted with both the Screen and StreamVane components modeled (summarized in Chapter 4), whereas the StreamVane Component Only cases utilized an additional CFD analysis conducted without the Screen component modeled (all computational setting remained consistent with the exception of the Screen device). The StreamVane Component Only case was an assumed future installation scenario and was desired to be analyzed.

Pressure loads on the vane surfaces were extracted from the CFD solution and applied to the vane surfaces. Fixed support boundary conditions were imposed on the bolt flange restricting movement. The finite element analysis was then conducted and resulting maximum deformation (δ_{max}) and maximum stress (σ_{max}) were computed. The Factor of Safety (FOS) was then calculated as the yield strength of fused deposition model Ultem 9085 (4800 psi) [114] normalized by the maximum calculated stress. The maximum deformation, maximum stress, and factor of safety results are summarized in Table B.1 while the deformation and stress contours are illustrated in Figure B.1, Figure B.2, and Figure B.3.

Table B.1: ScreenVane Stress Analysis – Factor of Safety

	$Isolated\ StreamVane$	$Coupled\ StreamVane$	$Isolated\ ScreenVane$	$Coupled\ ScreenVane$
δ_{max}	1.39×10^{-5} [in]	1.39×10^{-5} [in]	2.26×10^{-5} [in]	2.24×10^{-5} [in]
σ_{max}	127.78 [psi]	127.49 [psi]	130.52 [psi]	130.87 [psi]
FOS	37.56	37.65	36.78	36.68

In all loading conditions, negligible deformation was detected in the ScreenVane distortion generator. Additionally, stresses were extremely low resulting in Factors of Safety greater than 35x for all conditions. Based on small loads generated by relatively low turning angles and a robust design, this ScreenVane was verified safe for installation in the turbofan inlet duct.

Appendix B – ScreenVane Stress Analysis

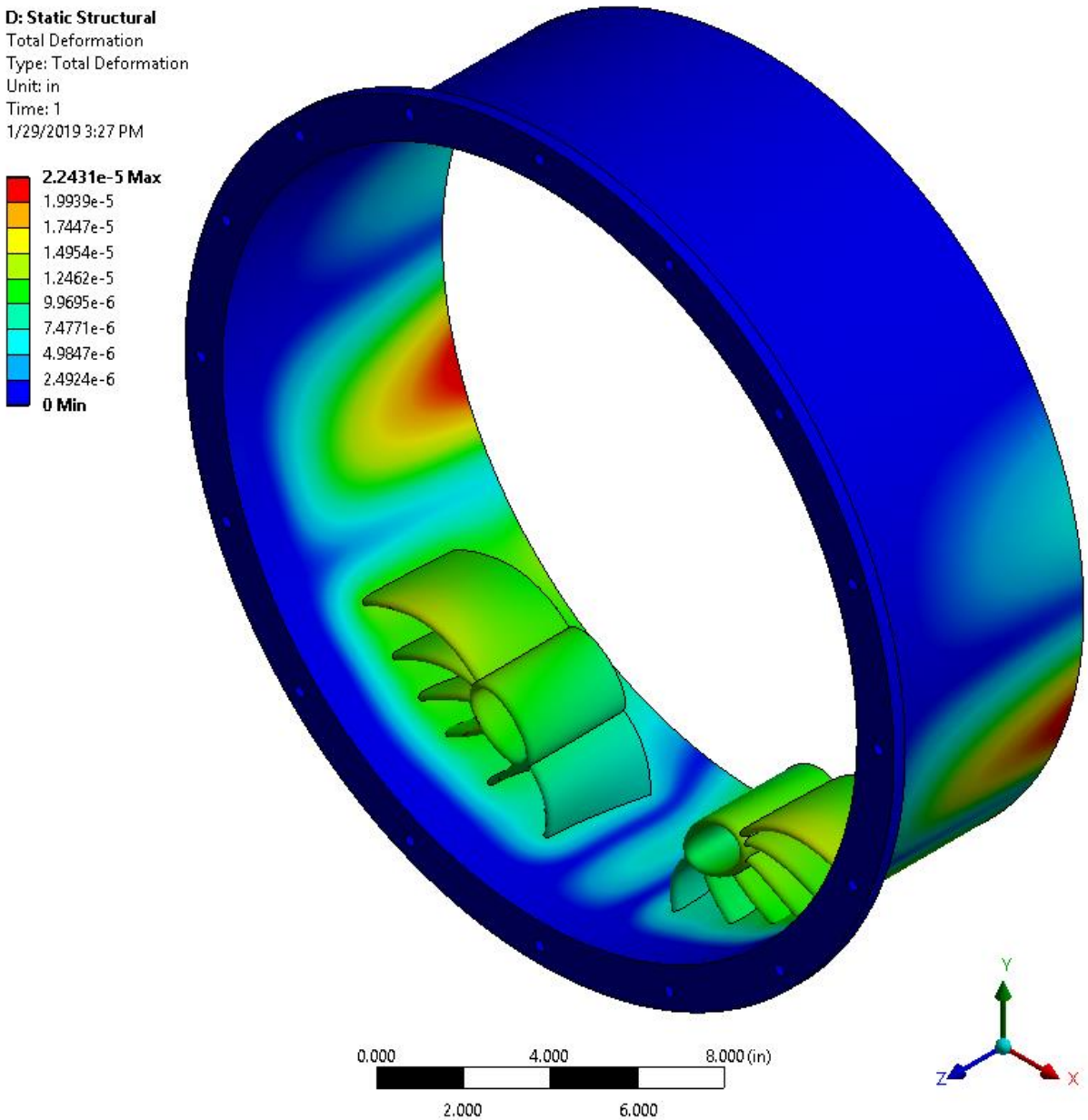

Figure B.1: ScreenVane Stress Analysis – Deformation Contour

Appendix B – ScreenVane Stress Analysis

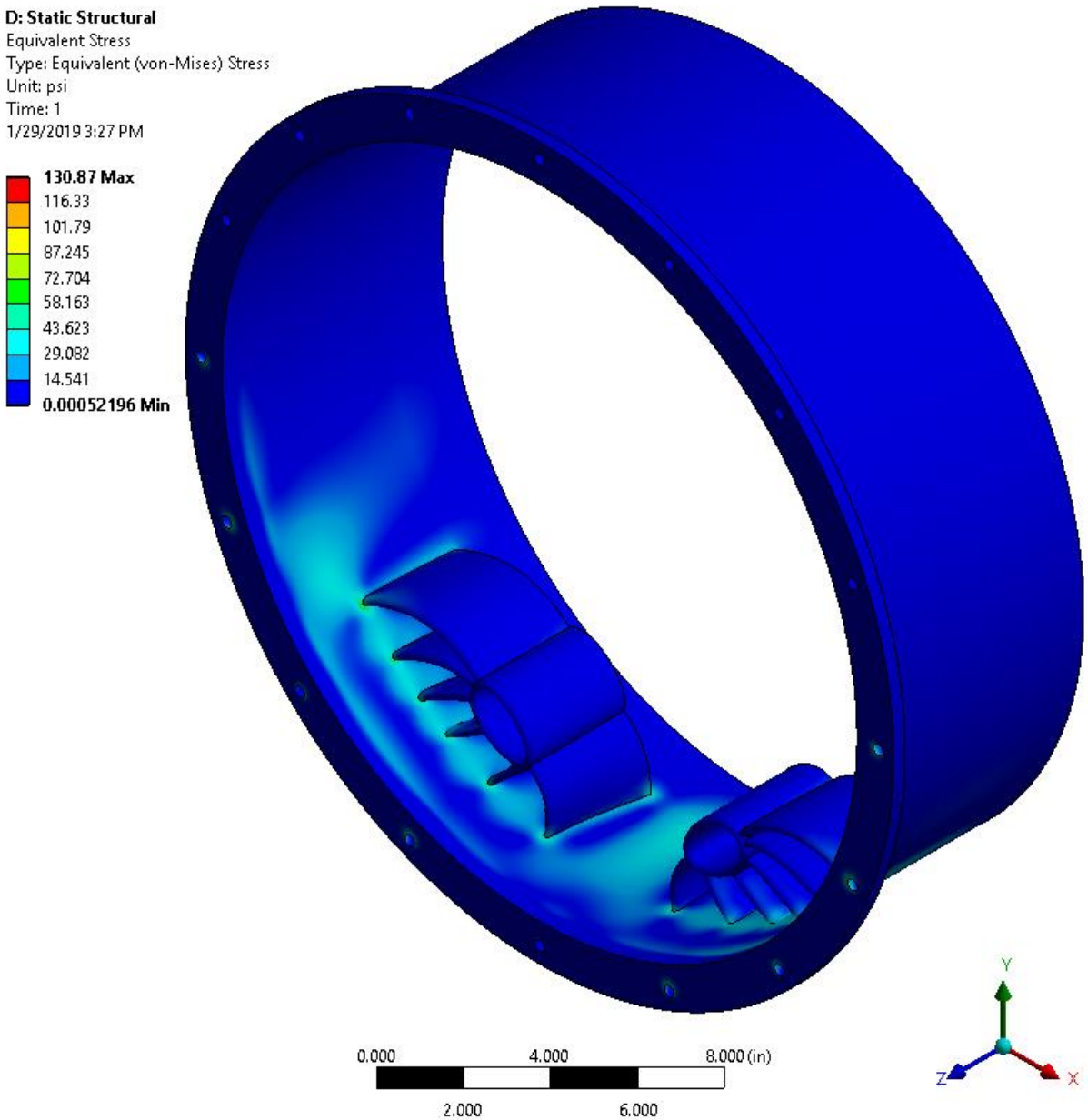

Figure B.2: ScreenVane Stress Analysis – Stress Contour

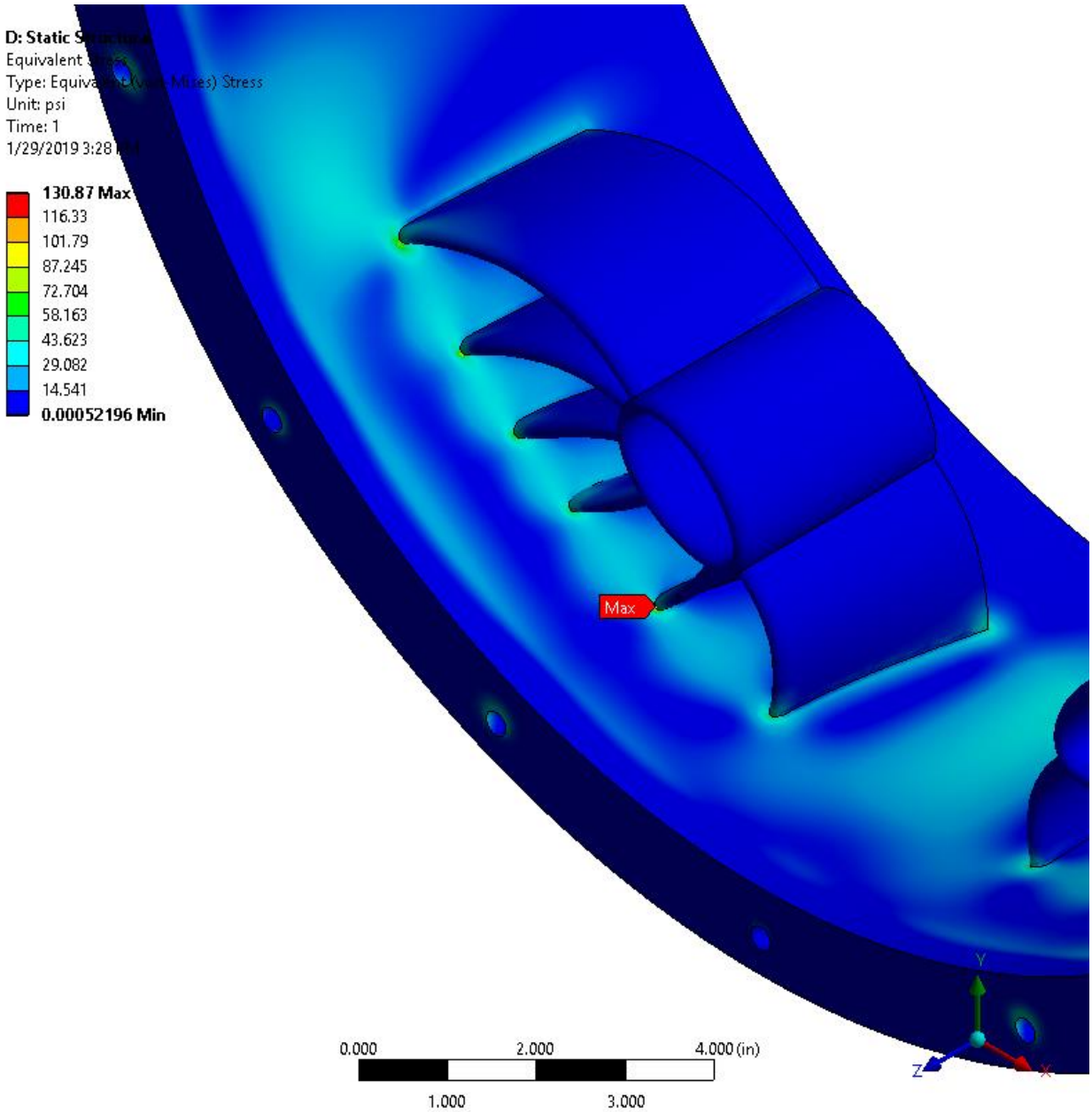

Figure B.3: ScreenVane Stress Analysis – Maximum Stress Contour

Appendix C – Turbofan Engine Ground Test Setup

The following section provides a detailed, illustrated procedure for the turbofan engine ground test setups utilized in the current investigation. Where appropriate, differences between the isolated experimental setup and the coupled experimental setup are noted.

Step 1:

The isolated experimental setup began at the fan case with the turbofan engine mounted in a custom pylon.

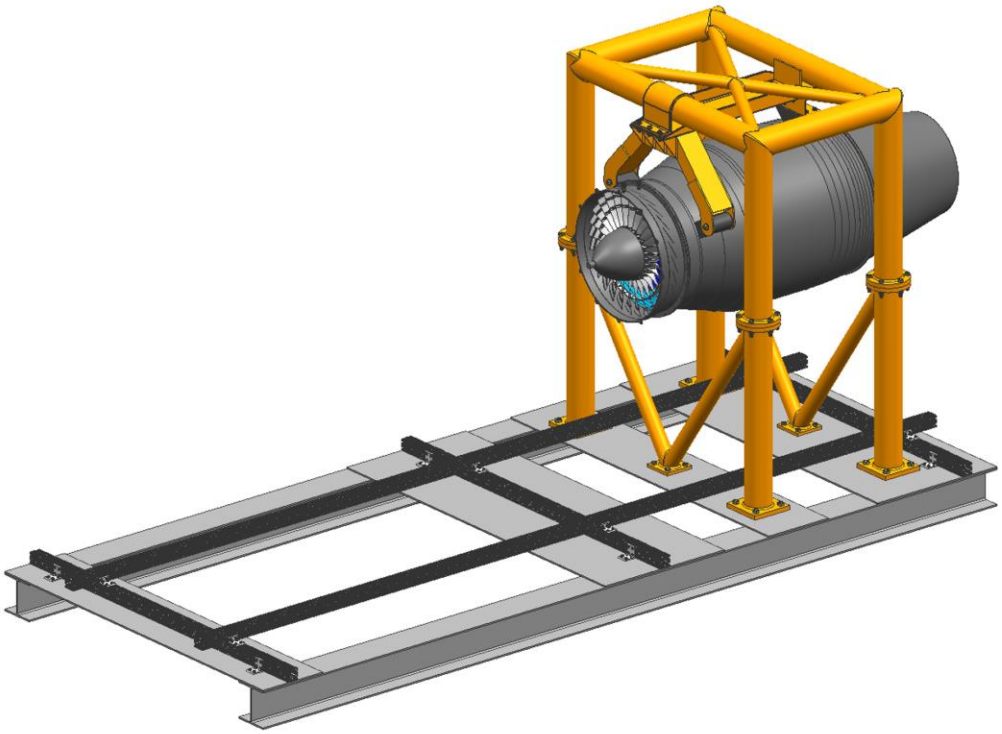

Figure C.1: Turbofan Engine Ground Test Setup – Step 1

Step 2:

A thick-walled, 0.37 diameter axial length, constant area, cylindrical inlet duct section was bolted to the fan case using existing hardpoints on the fan case. This empty inlet duct section provided a mounting location for an optical once-per-revolution fan speed sensor. During the course of the current investigation, the engine data acquisition system was improved such that the optical once-per-revolution fan speed sensor was deemed obsolete and was not utilized. The thick-walled inlet duct section remained installed for the isolated test setup and provided additional isolation length, but was removed for the coupled test setup.

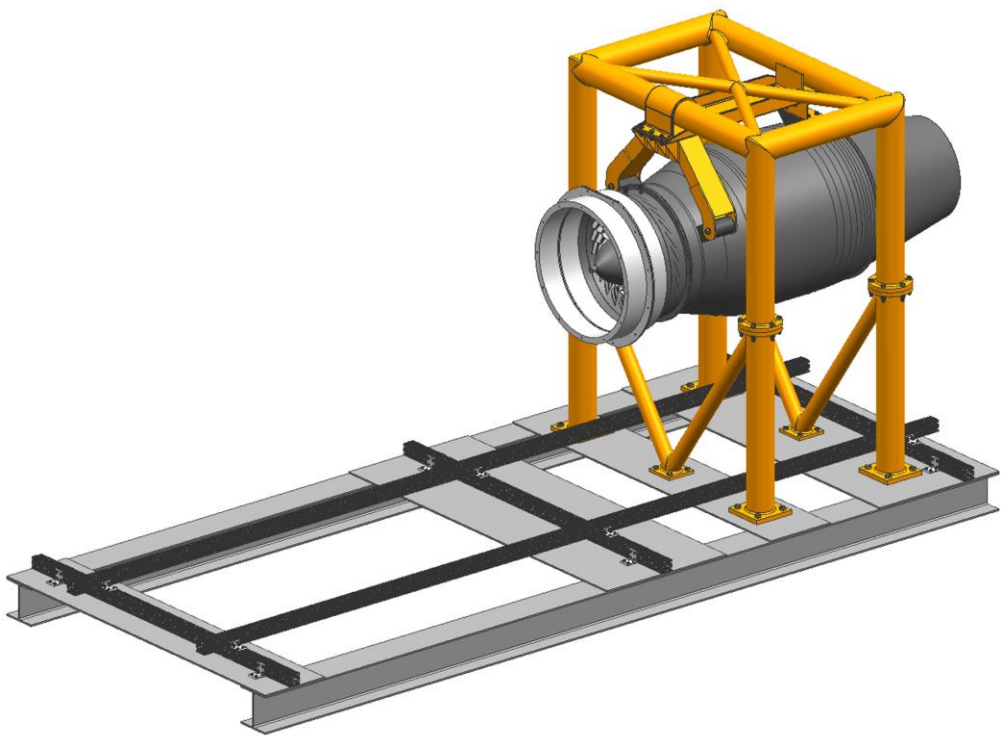

Figure C.2: Turbofan Engine Ground Test Setup – Step 2

Step 3:

A thin-walled, two diameter axial length, constant area, cylindrical inlet duct section (isolation duct) was bolted to the thick-walled inlet duct section. The empty inlet duct section allowed sufficient distance to eliminate turbomachinery interactions from propagating forward into the measurement plane. Previous research suggested that turbofan engine components (fan rotor and nose cone) influence the fluid volume at a distance of up to one half of a diameter upstream. To ensure isolation, the standoff distance was extended to two full diameters. The isolation duct was installed for the isolated test setup, but was removed for the coupled test setup.

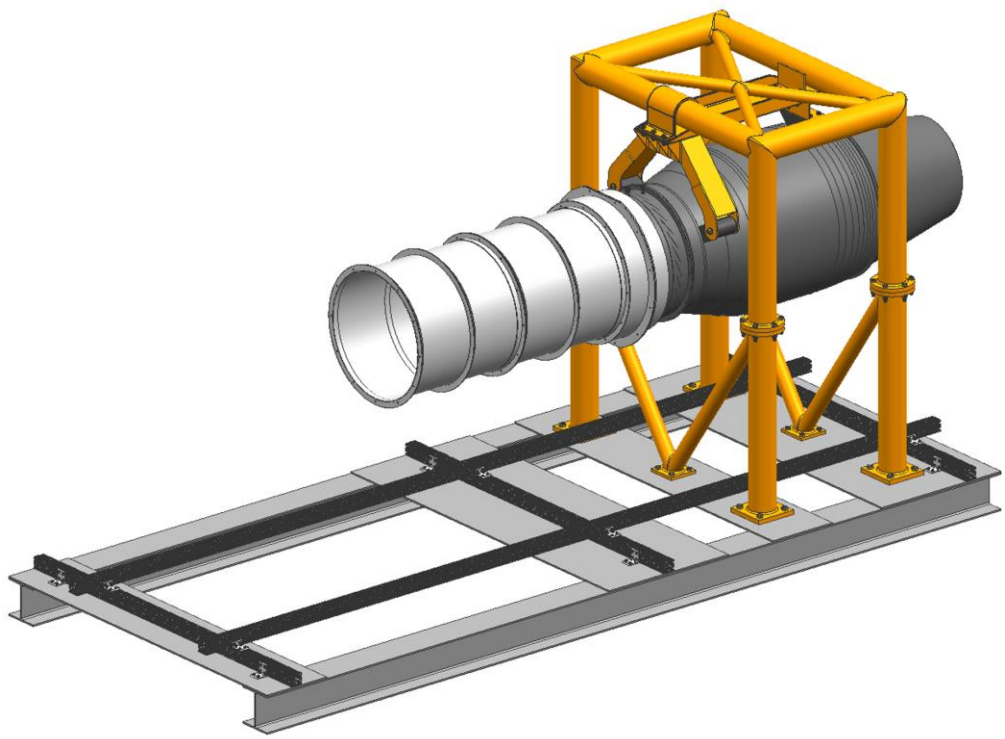

Figure C.3: Turbofan Engine Ground Test Setup – Step 3

Step 4 (AIP Setup):

Continuing upstream, the measurement spool was assembled and installed. First, a thick-walled, 0.20 diameter axial length, constant area, cylindrical inlet duct section was attached to a t-slotted aluminum support frame. The frame supported the weight of the duct section and instrumentation mount, maintained centerline concentricity, and allowed for axial positioning of instrumentation by way of sliding connection to a floor mounted rail system. The downstream flange of the measurement spool was bolted to the upstream flange of the isolation duct. In the coupled experimental setup, the measurement spool was bolted directly to existing hardpoints on the fan case. A universal mounting plate was attached to the thick-walled inlet duct section at top-dead-center and served as a hardpoint for the radial traverse. The radial traverse was then attached to the universal mounting plate, followed by a small rotary table attached to the radially traversing platform. The rotational axis of the small rotary table was aligned with the incorporated measurement spool wall penetration instrumentation port. The radial traverse allowed instrumentation to plunge through the fan case wall and across the flow path. The rotary table assisted with instrumentation alignment during installation.

The five-hole three-dimensional flow probe was inserted through the rotary table and measurement spool wall. Compression fittings on the exterior of the measurement spool as well as the top and bottom of the rotary table secured the probe throughout testing. PTFE ferrules allowed the probe to smoothly plunge radially, while set screw shaft collars located above and below the rotary table mount effectively locked the probe from slipping in the radially traversing mount. Probe installation procedure continued as follows:

1) Install the probe through the rotary table and measurement spool wall compression fittings.
2) Secure the probe within the rotary table using set screw shaft collars to eliminate slip in the radially traversing mount.
3) Retract the tip of the probe just beyond the inner wall of the measurement spool.
4) Using a small piece of thin shim stock placed flush with the inner wall surface, slowly plunge the probe radially inward until probe tip comes contacts the shim stock. At the instant of contact, the probe is radially “zeroed”.
5) Set the limit switch of the radial traverse.
6) Install a custom rotary alignment apparatus to the upstream measurement spool flange. The rotary alignment apparatus consists of a stiff aluminum frame and small free-jet tube. The free-jet tube is assumed to be parallel to the engine axis.
7) Plunge the probe radially inward until the probe sensing area is aligned with the small free-jet tube.
8) Connect a handheld digital manometer (Dwyer 477A-1) to the yaw angle sensing ports of the probe.
9) Apply compressed air to the free-jet tube.
10) Exploiting the nulling nature of the prism style five-hole three-dimensional flow probe, rotate the rotary table while monitoring the handheld digital manometer until the measured differential pressure was stable near zero. Once accomplished, the probe is aligned with the streamwise fluid direction.

[Note: Because testing procedure requires both distorted and non-distorted data collection, perfect probe alignment is not critical. This alignment process is only used to ensure that the probe is nearly nulled with streamwise flow and flow angles are measured in the center of the uniform calibration where greatest accuracy is known.]

11) Remove the custom rotary alignment apparatus and handheld digital manometer.
12) Retract the probe to the zeroed radial position.
13) Connect the five pressure ports to desired pressure scanner channels.
14) Connect the thermocouple plug to the desired temperature acquisition channel.

Step 4 (FREP Setup):

Continuing upstream, the measurement spool was assembled and installed. First, a thick-walled, 0.20 diameter axial length, constant area, cylindrical inlet duct section was attached to a t-slotted aluminum support frame. The frame supported the weight of the duct section and instrumentation mount, maintained centerline concentricity, and allowed for axial positioning of instrumentation by way of sliding connection to a floor mounted rail system. The downstream flange of the measurement spool was bolted directly to existing hardpoints on the fan case. A universal mounting plate was attached to the thick-walled inlet duct section at top-dead-center and served as a hardpoint for the radial traverse. The radial traverse was then attached to the universal mounting plate, followed by a small rotary table attached to the radially traversing platform. The rotational axis of the small rotary table was aligned with the fan exit instrumentation port. The radial traverse allowed instrumentation to plunge through the fan case wall and across the flow path. The rotary table assisted with instrumentation alignment during installation.

The five-hole three-dimensional flow probe was inserted through the rotary table and fan case wall. Compression fittings on the exterior of the fan case wall as well as the top and bottom of the rotary table secured the probe throughout testing. PTFE ferrules allowed the probe to smoothly plunge radially, while set screw shaft collars located above and below the rotary table mount effectively locked the probe from slipping in the radially traversing mount. Probe installation procedure continued as follows:

1) Install the probe through the rotary table and fan case wall compression fittings.
2) Secure the probe within the rotary table using set screw shaft collars to eliminate slip in the radially traversing mount.
3) Retract the tip of the probe just beyond the inner wall of the fan case.
4) Using a small piece of thin shim stock placed flush with the inner wall surface, slowly plunge the probe radially inward until probe tip comes contacts the shim stock. At the instant of contact, the probe is radially “zeroed”.
5) Set the limit switch of the radial traverse.
6) Install a custom rotary alignment apparatus to the radial traverse mount. The rotary alignment apparatus consists of a stiff aluminum frame and small free-jet tube. The free-jet tube is assumed to be perpendicular to the engine axis.
7) Extract the probe radially outward until the probe sensing area is aligned with the small free-jet tube.

8) Connect a handheld digital manometer (Dwyer 477A-1) to the yaw angle sensing ports of the probe.
9) Apply compressed air to the free-jet tube.
10) Exploiting the nulling nature of the prism style five-hole three-dimensional flow probe, rotate the rotary table while monitoring the handheld digital manometer until the measured differential pressure was stable near zero. Once accomplished, the probe is aligned perpendicular to streamwise fluid direction.
11) Rotate the probe 90° to align with the streamwise fluid direction.
12) Rotate the probe a desired offset angle to align with the known fan rotor blade turning angle. By aligning the probe in this manner, the measured relative flow angle will be small and fall near the center of the probe calibration where accuracy is greatest. To determine absolute flow angles, the offset value is simply added to the relative flow angle.

    [Note: Because testing procedure requires both distorted and non-distorted data collection, perfect probe alignment is not critical. This alignment process is only used to ensure that the probe is nearly nulled with flow direction and flow angles are measured in the center of the uniform probe calibration where greatest accuracy is known.]
13) Remove the custom rotary alignment apparatus and handheld digital manometer.
14) Plunge the probe to the zeroed radial position.
15) Connect the five pressure ports to desired pressure scanner channels.
16) Connect the thermocouple plug to the desired temperature acquisition channel.

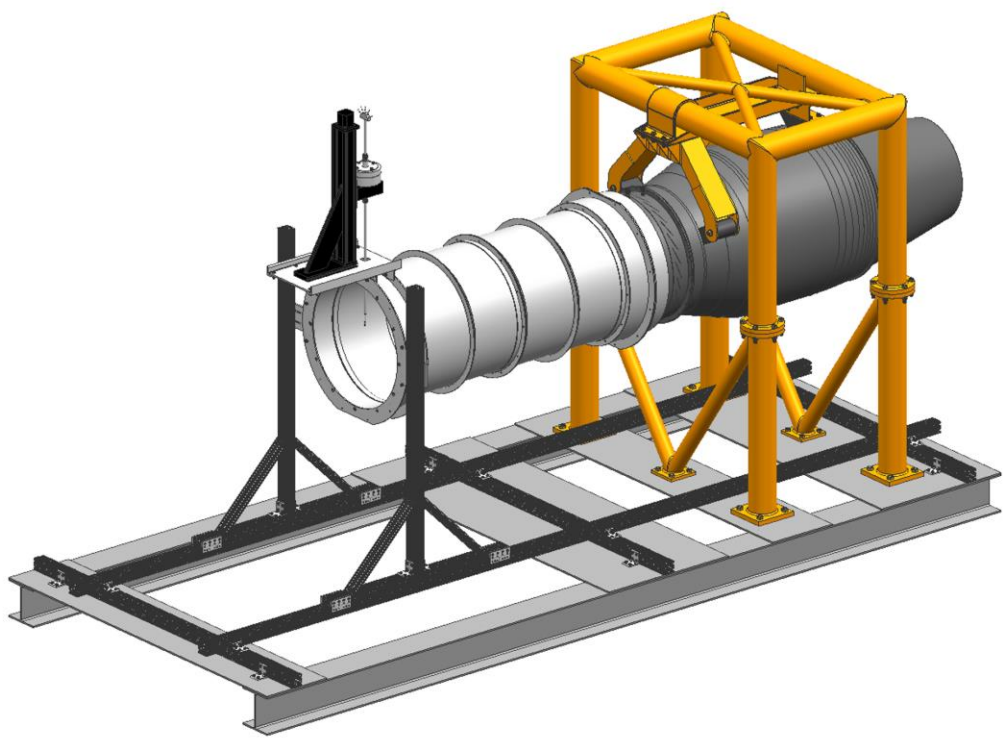

Figure C.4: Turbofan Engine Ground Test Setup – Step 4

Step 5:

A thin-walled, 0.70 diameter axial length, constant area, cylindrical inlet duct section (settling duct) was bolted to the upstream flange of the measurement spool. This tunnel section was used to position the ScreenVane at an appropriate upstream location. The offset distance allowed the small-scale wake structures generated by the turning vanes of the ScreenVane device to dissipate before entering the measurement plane and fan rotor.

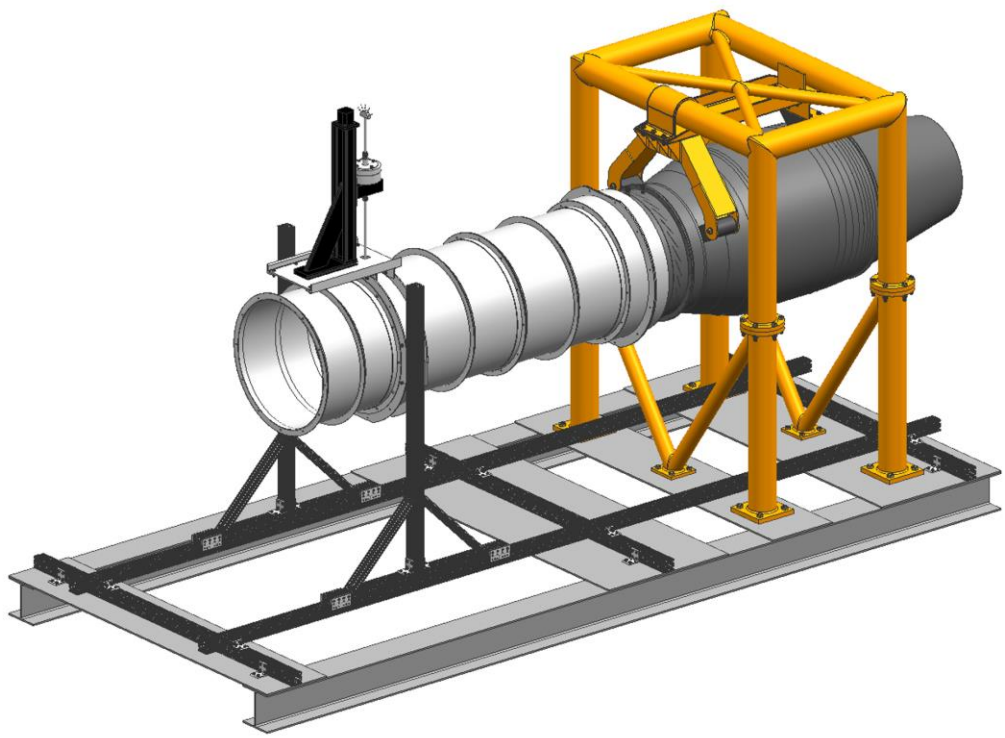

Figure C.5: Turbofan Engine Ground Test Setup – Step 5

Step 6:

The ScreenVane rotator was bolted to the upstream flange of the settling duct. The ScreenVane was aligned in the rotator using indexed markings on the ScreenVane shroud and rotator duct wall.

[Note: For the non-distorted baseline test, the ScreenVane was removed from the rotator and replaced by a uniform wire mesh screen. This screen was made from wire mesh identical to that used as the backer screen material for the total pressure distortion Screen. The use of this screen assisted in controlling inlet air mass flow rates for non-distorted baseline tests. Because the flow was assumed uniform in the non-distorted test, five-hole three-dimensional flow probe measurements were taken at the top-dead-center circumferential location at all plunge depths matching the distorted test.]

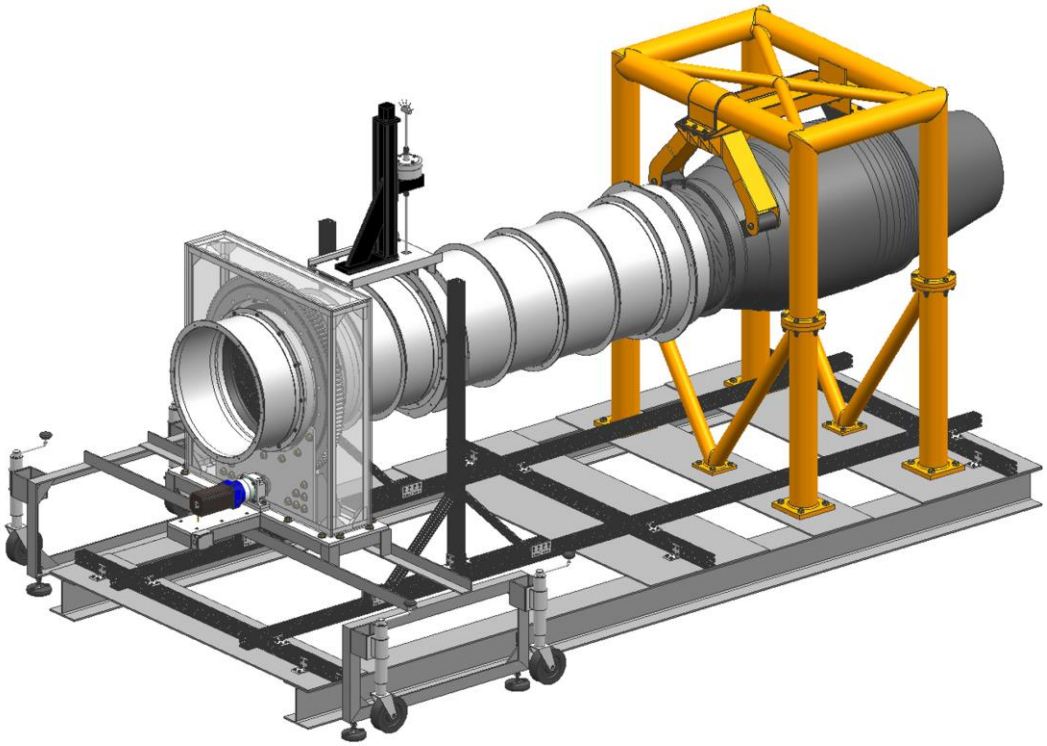

Figure C.6: Turbofan Engine Ground Test Setup – Step 6

Step 7:

The bellmouth inlet was bolted to the upstream flange of the rotator. The static pressure taps (located at one and one half diameters downstream of the bellmouth inlet) were connected to the desired pressure scanner channels.

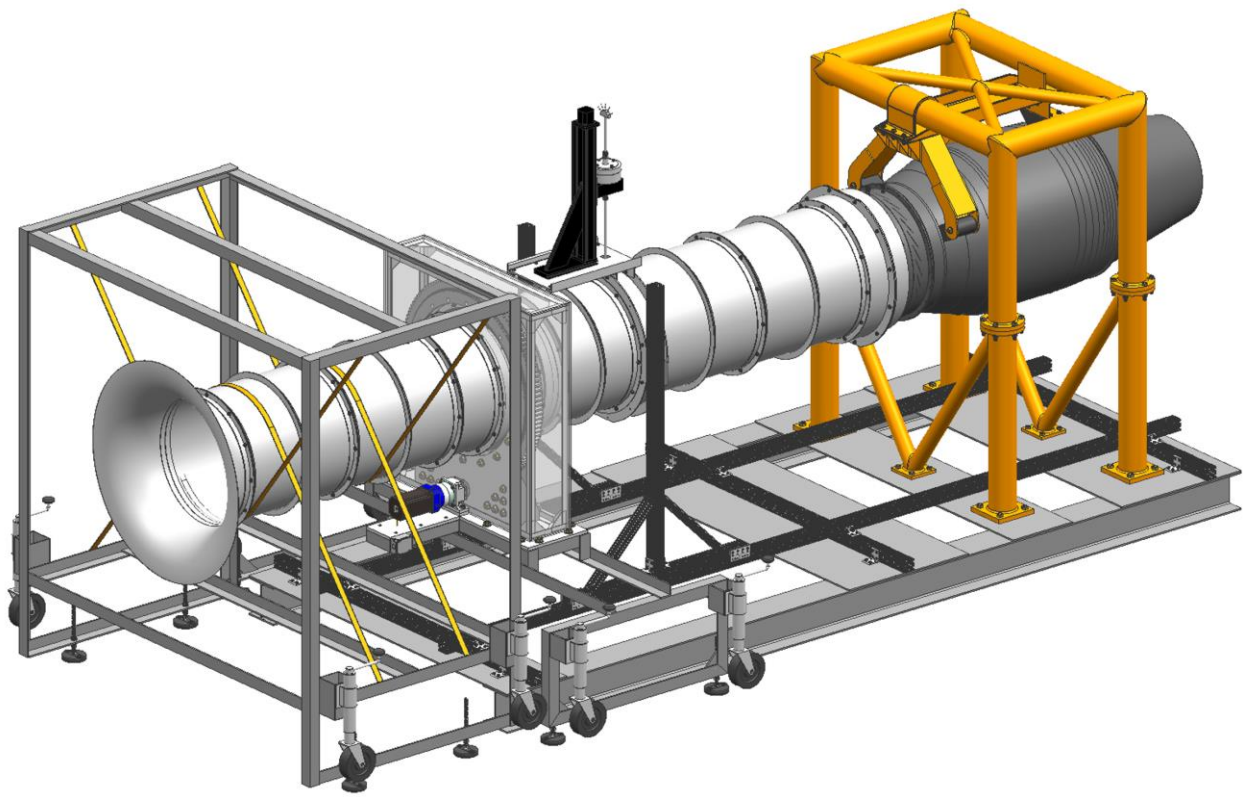

Figure C.7: Turbofan Engine Ground Test Setup – Step 7